UNIVERSITY OF SOUTHAMPTON

FACULTY OF ENGINEERING, SCIENCE AND MATHEMATICS

Optoelectronics Research Centre

Focussing and Diffraction using a High Harmonic Source

Benjamin Mills

Thesis for the degree of Doctor of Philosophy

September 2009

Abstract

High Harmonic Generation is a highly nonlinear process that can be used to generate a high flux, low divergence, coherent beam in the extreme ultraviolet (XUV) wavelength range. It is proposed that this radiation source could be implemented for microscopy using coherent diffractive imaging, with potential measurements including the shape characterisation of single proteins and other biological samples. This thesis documents the development of the diffraction beam line at the University of Southampton, and presents experimental results that show progress towards this goal.

A spherical multilayer mirror and a tapered hollow fiber have been used to focus the XUV beam. The mirror produced an astigmatic focus as a result of the off-axis geometry. Analysis of the surface quality of the mirror enabled an explanation for the observed interference peak splitting. The fiber was found to produce a smaller focus, but suffered from a degraded beam quality due to multiple reflections inside the optic.

Using a phase retrieval algorithm, an experimental XUV diffraction pattern has been used to determine the shape of a micron-sized sample. Fresnel diffraction from an array of micron-sized apertures has been simulated and experimentally verified.

A technique for simultaneously measuring the structure and dielectric constant of a nanosized periodic sample, for multiple wavelengths, is presented. This is achieved by using the Mie solution to model the diffraction peak intensities from a hexagonal array of 196 nm diameter polystyrene spheres. Refractive index results are given for the range 25 to 30 nm and are found to disagree with tabulated values.

Contents

List of Figures

List of Tables

DECLARATION OF AUTHORSHIP

I, Benjamin Mills, declare that the thesis entitled "Focussing and Diffraction using a High Harmonic Source" and the work presented in it are my own. I confirm that:

- this work was done wholly or mainly while in candidature for a research degree at this University;
- where any part of this thesis has previously been submitted for a degree or any other qualification at this University or any other institution, this has been clearly stated;
- where I have consulted the published work of others, this is always clearly attributed;
- where I have quoted from the work of others, the source is always given. With the exception of such quotations, this thesis is entirely my own work;
- I have acknowledged all main sources of help;
- where the thesis is based on work done by myself jointly with others, I have made clear exactly what was done by others and what I have contributed myself;
- parts of this work have been published as:

  B. Mills, C. F. Chau, E. T. F. Rogers, J. Grant-Jacob, S. L. Stebbings, M. Praeger, A. M. de Paula, C. A. Froud, R. T. Chapman, T. J. Butcher, J. J. Baumberg, W. S. Brocklesby, and J. G. Frey. *Direct measurement of the complex refractive index in the extreme ultraviolet spectral region using diffraction from a nanosphere array*, Applied

Physics Letters, 93, 231103 (2008). Selected for both the December 2008 issue of Virtual Journal of Nanoscale Science and Physics (*www.vjnano.org*), and the January 2009 issue of Ultrafast Science (*www.vjultrafast.org*).

B. Mills, E. T. F. Rogers, J. Grant-Jacob, S. L. Stebbings, M. Praeger, A. M. de Paula, C. A. Froud, R. T. Chapman, T. J. Butcher, J. J. Baumberg, W. S. Brocklesby, and J. G. Frey. *EUV off-axis focussing using a High Harmonic Source*, Proc. SPIE, Vol. 7360, 736003 (2009)

S. L. Stebbings, E. T. F. Rogers, A. M. de Paula, M. Praeger, C. A. Froud, B. Mills, D. C. Hanna, J. J. Baumberg, W. S. Brocklesby and J. G. Frey. *Molecular variation of capillary-produced soft x-ray high harmonics*, Journal of Physics B, 41, 145602 (2008).

C. A. Froud, R. T. Chapman, E. T. F. Rogers, M. Praeger, B. Mills, J. Grant-Jacob, T. J. Butcher, S. L. Stebbings, A. M. de Paula, J. G. Frey and W. S. Brocklesby. *Spatially resolved $Ar^{\star}$ and $Ar^{+\star}$ imaging as a diagnostic for capillary-based high harmonic generation*, J. Opt. A: Pure Appl. Opt, 11, 054011 (2009).

Signed: _____

Date: _____

Acknowledgements

Thanks is due to the following people:

My supervisor, William Brocklesby, for guidance and advice over the last four years.

Jeremy Frey, for his endless enthusiasm and knowledge, and for giving me the opportunity to work on such an interesting and challenging project.

To the original group members Chris Froud, Matthew Praeger and Ana de Paula, for taking the time to show me how the experimental side of the research worked. That much of the original experimental setup is still around after four years is testament to their skills and foresight. A special thanks goes to Ana for the many months it took us to set up and align the hollow focussing fibers.

The later group members Edward Rogers, Sarah Stebbings, James Grant-Jacob, Richard Chapman and Tom Butcher for their help on both the experimental and theoretical side of the project.

Jeremy Baumberg and David Hanna for their seemingly simple comments and questions, which led to vast chunks of results and analysis.

EPSRC, for my funding and making the last four years possible.

Eleanor Tarbox for proof reading an early version of my thesis.

My parents, especially my father, who persuaded me to apply for a PhD and, as it turned out, actually had the same supervisor.

Finally, thanks is due to my fiancée Gemma who has supported me for the last four years, and proof read my final draft.

Chapter 1

Introduction

Since their discovery by Wilhelm Roentgen in 1886, X-rays have enabled important advances in a wide variety of imaging techniques, ranging from medical applications to the structural and chemical characterisation of crystals and biological materials. These applications are possible due to the high energy and short wavelength of the X-ray photons, which allow them to penetrate further into materials than visible light and be diffracted in directions that are determined by the spacings between atoms.

One important application, X-ray crystallography, is the technique of analysing the X-ray diffraction pattern from a crystal structure. As the diffracted angles are determined by the interatomic spacing, the molecular composition and the structure and disorder of a crystal can be determined. This has enabled advances in material science, atomic physics and molecular chemistry, and has directly led to the characterisation of the DNA double-helix [1].

With the recent development of short-pulsed lasers and their direct application to the generation of pulsed X-ray sources, high spatial resolution can now be combined with a femtosecond temporal resolution. This has led

to the new field of structural dynamics, with recent results including the study of the dynamics of electron wave packets [2].

One area that X-ray pulses are directly applicable is the characterisation of biological protein structures. This can be achieved by measuring the scattered intensity from a crystallised protein. However, as many proteins cannot be crystallised and those that can are often distorted during the process [3], techniques for looking at single proteins are key to understanding the huge number of identified but uncharacterised proteins [4].

In order to study such a small sample, the X-ray flux must be very high. This has led to the problem of sample damage. Theoretical modelling has shown that irreversible damage can occur on the time scale of ten to fifteen femtoseconds [5]. This is a simple consequence of the ionisation of inner electrons by an X-ray photon and the resulting Coulomb explosion from the remaining positive charge. The consequence is that some imaging techniques cannot take place before irreversible damage occurs. However, by using extremely short X-ray pulses, a sample can be imaged before it is destroyed. In fact, recent results have shown that a sample can be studied in steps through the Coulomb explosion [6]. There is therefore great interest in the generation and comprehension of ultrashort X-ray pulses.

A recent application of X-rays that is showing great promise is coherent diffractive imaging (CDI), which uses the phase retrieval algorithm devised by Gerchberg and Fienup [7]. This technique allows a nonperiodic sample to be 'imaged' using only the observed scattering pattern, despite the fact that a X-ray detector does not record any phase information. Experimental demonstrations include micron-sized machined structures [8] (see figure 1.1), showing that nanometer scale resolution can be achieved despite the fact that the sample is irreversibly damaged within a few femtoseconds.

Figure 1.1: *Coherent diffractive imaging (CDI) demonstrated by Chapman et. al. [8], using the FLASH Free Electron Laser radiation source at 32 nm, showing a) a single-shot diffraction image, b) a scanning electron microscopy image of the sample before CDI and c) a reconstructed image of the sample before being destroyed by the X-rays, calculated from just the diffraction pattern.*

To achieve single-shot CDI, an intense pulsed beam of high energy light is required. The following paragraphs briefly explain some of the possible radiation sources and provide the motivation for the source used throughout this thesis.

Laser plasma generation [9], which also includes table-top variations [10], uses a high powered laser focussed onto a suitable target material to produce a plasma, which can emit wavelengths in the XUV and x-ray spectral region. Micron-sized objects have been imaged using this source [11]. However, the generated pulse lengths are generally on the order of picoseconds and therefore too long for single-shot imaging.

Synchrotron radiation sources have been providing important results in the fields of structural biology for many years [12,13]. Time resolved studies have also been demonstrated [14]. There is also a multitude of results in other fields such as material science [15], condensed matter physics [16] and absorption spectroscopy [17]. Synchrotron radiation wavelengths can

vary from fractions of an Angstrom to tens of nanometers (see [18], for example), typically with picosecond pulse lengths [19]. A slicing technique demonstrated at the Advanced Light Source, achieved by using an ultrashort laser pulse to modulate the energy of the electrons, has been shown to generate 300 femtosecond X-ray pulses [20]. Whilst there are undoubtedly many applications, the generated pulse lengths are currently too long for single-shot imaging of the type described above.

X-ray Free Electron Lasers (FEL), such as FLASH [21], create a high energy laser beam by accelerating an electron bunch through an undulator. Currently FLASH can produce X-ray pulses in the range 6.5 to 50 nm, with pulse lengths as short as 10 femtoseconds (fs) [22]. Single-shot imaging has been demonstrated on this source (see figure 1.1).

The Linac Coherent Light Source, an X-ray FEL which will begin operations in September 2009, will be able to generate X-ray pulses that are almost nine orders of magnitude brighter than current synchrotron radiation [23]. The source is therefore proposed to be ideal for the characterisation of single biological samples. Initial tests during April 2009 have produced light at 0.15 nm.

High Harmonic Generation (HHG) [24, 25] is an enticing 'table-top' alternative to an FEL, and is the radiation source used throughout this thesis. HHG can provide a high flux of 10^{11} photons per second, with typical pulse lengths of 5 to 20 femtoseconds. The generated beam is spatially coherent [26] and hence ideal for diffractive imaging. Wavelengths are generated most efficiently in the range 20 to 40 nm, although shorter wavelengths are possible [27]. In addition, the generated wavelengths can be shifted [28] or optimised [29], allowing very specific control over the output spectrum. Due to the broad harmonic spectrum that is generated, HHG radiation has

been shown to support pulses shorter than sixty attoseconds [30]. Recent results have shown the successful imaging of micron-sized objects with a resolution of ∼70 nm [11]. This combination of nanometer spatial resolution and attosecond temporal resolution, along with the possibilities for spectral tailoring, has understandably led to a huge interest in using HHG as a laboratory-based X-ray source.

As the resolution limit when imaging is related to the wavelength of the light, wavelengths currently generated using HHG will enable the shapes of proteins and viruses larger than a few nanometers to be determined. This shape information can be used to determine the chemical composition and structure of biological samples and help improve molecular modelling, leading to a better understanding of molecular processes [31]. In July 2009, single-shot imaging of a fabricated sample with a resolution of 119 nm, was demonstrated using a HHG source [32]. However, there is still work to be done before the technique can be applied to single-shot imaging of biological materials. As demonstrated in this thesis, many areas of the current approach that can be improved, often with order-of-magnitude increases in flux possible.

This thesis documents the development of a biological imaging system that will be capable of combining attosecond temporal resolution with nanometer spatial resolution. The journey towards this goal is interesting in itself - the wavelengths generated using HHG exist in a generally unexplored spectral region and therefore this area is rich for new scientific endeavors.

The wavelengths generated throughout this thesis are above the aluminium edge at 17 nm and strictly should be defined as extreme ultraviolet (XUV), as they are in all subsequent sections.

1.1 Thesis Outline

This thesis documents the construction and optimisation of the HHG diffraction beam line at the University of Southampton. During this PhD, several large steps have been taken towards the goal of single molecule scattering. This work continues the progress made by previous group member Froud and Praeger who constructed the XUV generation apparatus. The experimental design, collection of experimental results and theoretical analysis should all be assumed as my own work, unless noted otherwise. Where contributions by others have been made, acknowledgements are explicitly given. My contribution is summarised by the following:

Firstly, an improvement in the understanding of the HHG process has been made, resulting in a significantly higher XUV flux and producing a source that is considerably less sensitive to the instabilities of the fundamental laser. This, along with development of the diffraction beam line setup, is presented in chapter 2.

Secondly, two focusing methods have been investigated: a multilayer mirror and a hollow fiber with a parabolic profile. The multilayer mirror produced an astigmatic focus, where the intensity and phase was shown to be strongly varying through the focus. By simulating small surface imperfections on the surface of the mirror, the experimentally observed diffraction peak splitting was explained. The hollow fiber was found to produce a smaller focus but due to multiple reflections inside the fiber, the focus quality was degraded. These results are presented in chapter 3.

Thirdly, preliminary results have shown the successful imaging of a micron-sized object. This result forms the basis for chapter 4, which also covers Fresnel diffraction from an array of circular apertures.

Finally, a technique is demonstrated for simultaneously measuring both

the structure and XUV dielectric constant across several wavelengths for a nanoscale sample, from just a single diffraction image. Experimental results for polystyrene in the range 25 to 30 nm are found to disagree with the tabulated references. This result, along with a study into the application of this technique to other materials, is presented in chapter 5.

The overall conclusions and prospects for future work are discussed in chapter 6.

Chapter 2

XUV Generation

This chapter provides a background to the science and experimental techniques used in this thesis for generating extreme ultraviolet (XUV) through the technique of High Harmonic Generation (HHG). In the last few decades, ultrafast science has become imperative for understanding many frontiers of modern optics and thus a brief review is given in section 2.1. A discussion of the components of the ultrafast laser system, which is used for HHG, along with the diagnostics used to characterise the laser output is given in section 2.2.

In section 2.3, the technique of HHG is introduced along with the requirements for phase-matching the generated wavelengths. The properties of the XUV are also discussed here, in particular the role the gas plays in both generation and absorption. Section 2.4 discusses the techniques for separating the generated XUV from the fundamental laser light. The experimental setup used throughout this thesis is presented in section 2.5. This section includes a comparison of the experimental configurations that have been investigated, and a summary of XUV flux, spot size and other important considerations. Results concerning the sensitivity, noise and spatial

resolution limit of the XUV Charge Coupled Device (CCD) are presented in section 2.6.

2.1 Review of Ultrafast Science

To comprehend ultrafast science, it is important to understand the relationship between time and frequency. The Fourier transform relations, shown in equations 2.1 and 2.2, are used to switch between the time and frequency domain.

$$f(t) = \frac{1}{2\pi} \int F(\omega) exp(i\omega t) dw \tag{2.1}$$

$$F(\omega) = \int f(t) exp(-i\omega t) dt \tag{2.2}$$

The complex field in the time domain can be described by,

$$E(t) = \sqrt{I(t)} exp(-i\phi(t)) \tag{2.3}$$

where $I(t)$ is the intensity, and $\phi(t)$ is the temporal phase which describes the frequency versus time behavior.

When equation 2.3 is transformed into the frequency domain, it will have the form,

$$E(w) = \sqrt{S(w)} exp(-i\varphi(w)) \tag{2.4}$$

where $S(w)$ is the spectral density, and $\varphi(w)$ is the spectral phase. The spectral phase is defined as the phase of each frequency in the waveform. As shown in subsequent sections, the control of the spectral phase is critical to the generation of ultrashort laser pulses. To fully characterise an electric

field, either the intensity and temporal phase or the spectrum and spectral phase must be known. The Fourier relations show that a large bandwidth of light is required for a temporally short pulse.

The wavelength dependence of the refractive index has major implications for ultrashort optics. Temporal dispersion arises because the phase velocity, and hence the time taken to propagate through an optic, is dependent upon its wavelength. Consequently, some frequencies are delayed with respect to others. In regions of normal dispersion, this delays the higher frequencies with respect to the lower frequencies. Understanding how to counteract the unavoidable dispersion of optical devices is therefore paramount to the delivery of an ultrashort pulse.

To model the laser pulse propagation, it is generally easier to work with the spectrum and spectral phase. A Taylor expansion of the spectral phase about a central frequency ω_0,

$$\varphi(\omega) = \varphi_0 + \varphi_1[\omega - \omega_0] + \varphi_2\frac{[\omega - \omega_0]^2}{2!} + \varphi_3\frac{[\omega - \omega_0]^3}{3!} + ... \tag{2.5}$$

where $\varphi_0 = \varphi(\omega_0)$, $\varphi_1 = \frac{d\varphi(\omega_0)}{d\omega}$, $\varphi_2 = \frac{d^2\varphi(\omega_0)}{d\omega^2}$ and $\varphi_3 = \frac{d^3\varphi(\omega_0)}{d\omega^3}$, provides us with the phase delay, group delay, group delay dispersion and third-order dispersion. To produce the shortest possible pulse, independent control of these components, and their higher-order counterparts, may be required. However, in general only the third component, which describes a linear spectral phase shift, and the fourth component, which describes a quadratic spectral phase shift, are considered.

2.2 Ultrafast Laser System

To generate XUV radiation using HHG, a short and intense pulse of light is required. A schematic showing the setup used for this thesis is shown in figure 2.1.

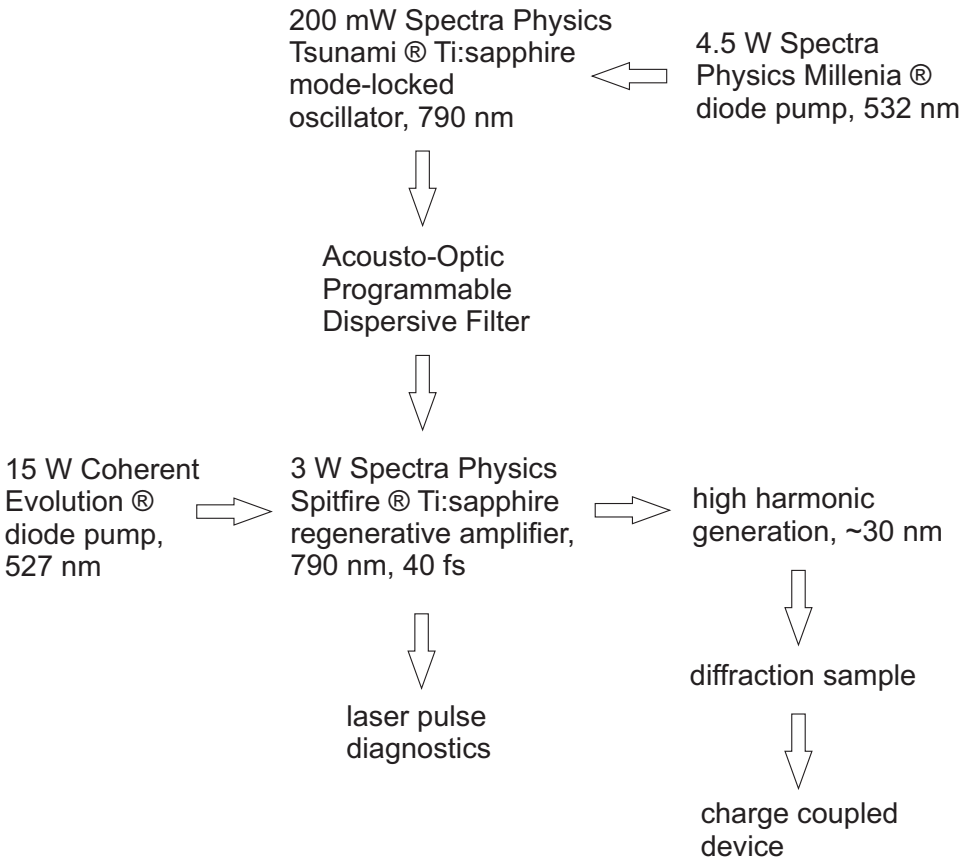

Figure 2.1: *Schematic of the ultrashort pulse and XUV generation system.*

In this section an outline of the seed and amplification laser is given, along with the diagnostics used to understand the laser pulses. The science behind the generation of HHG is detailed in section 2.3. The diffraction setup is presented in sections 2.5 and 2.6.

2.2.1 Mode-Locked Ti:Sapphire Oscillator

The mode-locked oscillator is used to produce nanojoule pulses that are approximately 25 femtoseconds (fs) long, at an 80 MHz repetition rate. These pulses are then sent to the amplifier, where the repetition rate is reduced to 1 kHz and the pulse energy is increased to 3 mJ. This section describes the design and operation of the oscillator.

The oscillator crystal is pumped by a 4.5 watt continuous wave Spectra Physics Millenia diode pump operating at 532 nm. Inside the oscillator cavity, a prism pair adds negative group delay dispersion to the pulse to counteract the positive second-order dispersion from the crystal and other optics. Bandwidths of 400 nm, and pulse lengths of 4 fs have been shown using a similar design [33].

In the Ti:Sapphire seed laser cavity, the nonlinear refractive index of the crystal causes an intracavity focus [34]. The refractive index can be described by,

$$n = n_0 + n_2 I \tag{2.6}$$

where n_2 is the nonlinear refractive index and I is the intensity. The constants are defined as $n_0 = \sqrt{1 + \chi^{(1)}}$ and $n_2 = \frac{\chi^{(3)}}{2n_0}$, where $\chi^{(1)}$ and $\chi^{(3)}$ are the first and third-order electric susceptibility respectively. By placing an aperture at this intracavity focus, a passively mode-locked system is created. A fluctuation in intensity will result in a change in the cavity loss, as the position of the focus will change. The Ti:Sapphire cavity is constructed such that if the intensity increases, the nonlinear refractive index will increase causing the beam waist to be smaller at the aperture, hence creating a smaller loss. Similarly, less intense light will experience a greater loss as it

will not be focussed as tightly. In the time domain, an intensity fluctuation will therefore experience a relatively small loss for the peak intensity but a higher loss on its less intense wings and so build up to be a short pulse. The initial noise required in the oscillator can be achieved by vibrating one of the dispersion prisms in the cavity. This modulates the cavity length and causes the laser modes to constructively interfere and produce a pulse of light.

Acousto-Optic Programmable Dispersive Filter

Before the pulse enters the amplifier, its spectral phase can be altered using an acousto-optic programmable dispersive filter (Dazzler) to optimise the spectral phase of the amplified pulse. A radio frequency (RF) signal produces an acoustic wave along a birefringent crystal. The polarisation of the incident pulse of light, which propagates normal to the density modulations, can be rotated ninety degrees due to these modulations, resulting in a different phase velocity. The position along the crystal where this occurs is defined by the wave form of the modulations, and hence different wavelengths can be delayed with respect to the others if a specifically designed acoustic wave is used.

2.2.2 Chirped Pulse Amplification

Inside the chirped pulse amplifier (CPA) system [35, 36], as shown in figure 2.2, the laser pulse from the seed oscillator is stretched via a grating pair to around 100 ps, allowing it to be amplified whilst minimising nonlinear effects inside the Ti:sapphire crystal. A second grating pair is subsequently used to apply the appropriate dispersion to re-compress the pulse. The amplifier receives nanojoule pulses at a 80 MHz repetition rate and selectively

amplifies pulses at a 1 kHz repetition rate to pulse energies of 3 mJ.

Amplification is achieved using a regenerative amplifier. Once every millisecond, a Pockels cell lets through a single stretched pulse into the amplification cavity. The pulse then passes through a Ti:sapphire gain medium approximately twenty times before a second Pockels cell switches the pulse out of the cavity. The relative timing of the Pockels cells define the number of passes and therefore the amplification of the pulse. The timings are optimised so that the pulse passes through the medium the minimum number of times to ensure saturation is reached whilst minimising dispersion effects. The Ti:sapphire crystal is pumped in the regenerative amplifier by 15 watts from the Spectra Physics Evolution, a doubled Q-switched Nd:YLF, at 527 nm. The amplified pulses are temporally compressed using a grating pair. A 98% dielectric beamsplitter (BS) is used to reflect the beam towards the two experimental beamlines, where it is further split by a 50% BS. The remaining 2% is passed through to the diagnostics, where the beam quality and pulse length can be monitored. These diagnostics are discussed in the following sections, 2.2.3 and 2.2.4.

2.2.3 Laser Beam Quality

In this section, the technique used for determining the quality of the amplified laser beam is presented. This parameter has a great deal of importance for HHG generation as the size of the focus at the point of generation, and hence the intensity, is dependent on this value. Knowledge of the parameter enables appropriate focussing objectives to be used. The technique presented here is repeated in chapter 3 in greater detail, where the beam quality of the generated XUV after two different focussing optics is presented.

The beam quality, also known as the M^2 parameter, is defined as the dif-

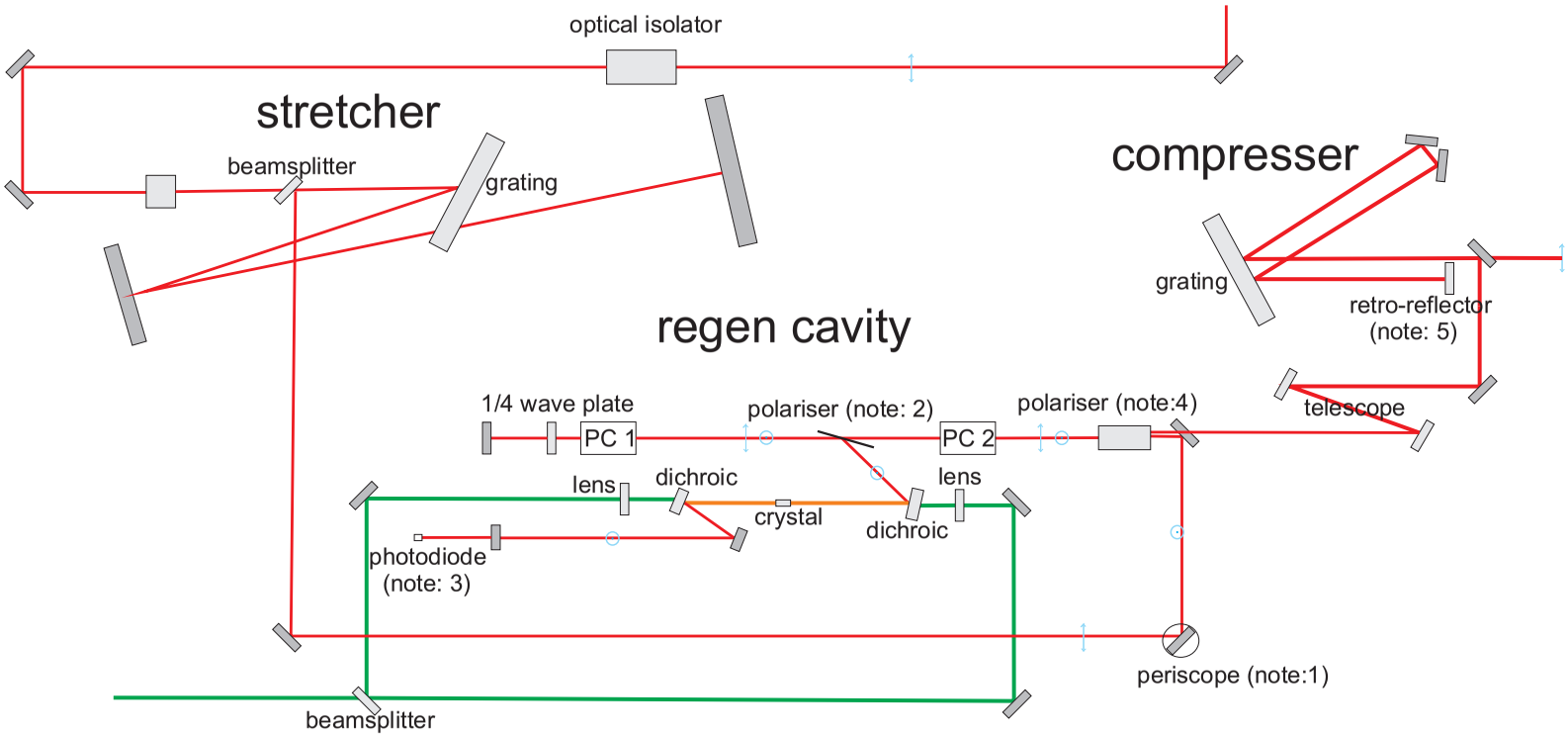

Figure 2.2: *Beam path through amplifier, showing stretcher, regenerative cavity and compressor. Mirrors are dark gray. Special optics are light gray. Pockel's Cell shortened to PC. Note 1: Periscope changes polarisation of beam. Note 2: If PC 2 is off, light reflects off polariser to beam dump, if PC 2 is on, light passes through into cavity. Light remains in cavity whilst PC 1 is on. Note 3: Photodiode measures leakage of mirror to monitor cavity amplification. Note 4: Once PC 1 is turned off, the light passes through the cavity polariser, through PC 2, and then is reflected up by the second polariser and hence over the mirror towards the compressor. Note 5: A vertical retro-reflector steps the beam upwards and over the final mirror and out of the compressor.*

ference between the divergence of a measured beam and that of a diffraction-limited beam. A beam which diverges two times faster will have an M^2 value of two. The size of the focus is also dependent on the parameter and hence to reach the intensities required for HHG (section 2.3) or couple light efficiently into a generation capillary (section 2.5) the M^2 value must be known.

The M^2 of a beam can be extracted from a set of beam width measurements [37] through a focus. Equation 2.7 shows that knowledge of $w(z)$ provides a unique solution for the M^2 value (assuming a monochromatic source), where w is the $1/e^2$ half-width of the beam intensity profile, w_0 is the $1/e^2$ half-width of the beam at the focus, M^2 is the beam quality, and z is the distance from the focus.

$$w(z) = w_0 \sqrt{1 + \left(\frac{M^2 \lambda z}{\pi (w_0)^2} \right)^2} \tag{2.7}$$

To measure the M^2, the spatial intensity through the focus, resulting from a 1 meter focal length mirror, was recorded on a charge coupled device. Analysis of a set of these images provided the beam width in the horizontal plane, $w(z)$. This data set is shown in figure 2.3, where the laser M^2 has been determined to be 1.78. Therefore the focus will be 1.78 times larger than that of a diffraction-limited beam in the horizontal direction. It is important to realise that the M^2 in the vertical and horizontal axes can be different. As shown in section 3.1, this can lead to interesting consequences when abberations such as astigmatism are involved.

The most significant error in this measurement arises from the resolution of the CCD. When the $1/e^2$ intensity has been determined, the two pixels that are either side of the most intense pixel and have the desired intensity, are noted. Due to the discrete data points, the pixels that have an intensity closest to the desired intensity are chosen. The beam width can therefore

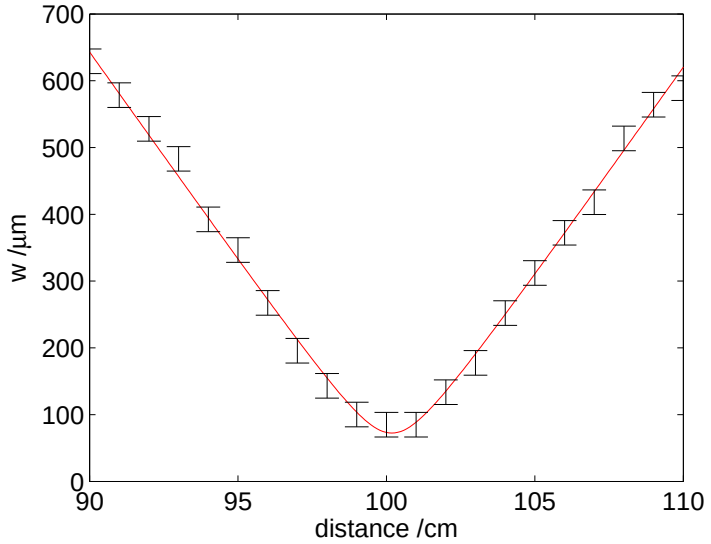

Figure 2.3: *Measured laser beam width in the horizontal plane, corresponding to an M^2 of 1.78 and w_0 of 72 µm.*

be incorrect for a distance corresponding to two CCD pixels. This effect is illustrated by the error bars on the figure. Further smaller errors arise from the beam propagation direction wandering slightly during the time required for the beam images to be taken. If the beam propagation direction changes to a slightly different angle, then the spot size will appear larger. This error has not been added to the figure, but is assumed to be relatively small.

2.2.4 Pulse Characterisation

HHG is a highly nonlinear process. It is therefore important to monitor the laser pulse length throughout experiments as small fluctuations will change the laser peak intensity and hence the XUV output. In addition, the pulse length must be measured in order to optimise the compressor in the CPA cavity (see section 2.2.2), after the laser amplification.

In order to measure a time period, a shorter reference signal is required. However, the pulses generated using CPA are some of the shortest man-made

occurrences and hence the pulse itself must be used to measure the length of the pulse. This can achieved by interfering it with a time-delayed replica inside a second harmonic generation crystal. By changing the time delay, an autocorrelation can be produced which indicates the length of the pulse. However, this yields only the temporal intensity. As mentioned in section 2.1, either the temporal intensity and temporal phase, or the spectral intensity and spectral phase, must be known in order to fully characterise an ultrashort pulse. By using a spectrometer in combination with the autocorrelator however, the temporal intensity and the spectral intensity can be measured, and from this initial information the spectral (and therefore temporal) phase can be iteratively solved to a good approximation. This technique, known as Frequency Resolved Optical Gating (FROG) [38], can therefore determine the electric field of an ultrashort pulse. A GRENOUILLE [39] is an adapted version of a FROG, which uses a Fresnel biprism instead of a moving mirror in order to enable a single shot measurement. This is the device used for all pulse measurements in this thesis, and is monitored frequently during generation of the XUV. In general, the laser system produces 40 ± 1 femtosecond pulses. The iterative calculation takes less than a second and generally produces a error, defined as the difference between the observed and simulated measurement, of less than one percent. This corresponds a pulse length measurement accuracy better than one femtosecond.

2.3 High Harmonic Generation

The XUV radiation demonstrated throughout this thesis was produced using HHG. In this section, the process is explained.

Firstly, a brief background and motivation for using the source is given. HHG is a well-established technique and as such there is a wealth of inter-

esting material available. The literature presented in this section is targeted towards understanding the possibilities and limitations of using this radiation source for diffractive imaging. In section 2.3.2 the 'three step model', which can be used to describe the generation process, is illustrated. In section 2.3.3, the two generation techniques used during this thesis and their phase matching equations are presented. The process of coupling light into a hollow glass capillary is then discussed. Finally, the role played by gas in both the generation and the absorption of XUV is discussed in section 2.3.4.

2.3.1 Motivation

HHG is a table-top technique that can be used to generate intense pulses of coherent light in the XUV and soft X-ray region of the spectrum [24, 40, 41]. There is therefore great interest in using this radiation for areas such as material analysis, absorption spectroscopy and biological imaging. Throughout this thesis, high harmonics are generated by focussing a high intensity laser pulse in argon gas. However, other noble gases and molecules have been shown to produce significantly different outputs [42, 43]. The generation process produces periodic fluxes of photons, generally lasting around 250 attoseconds (10^{-18}) [44], which have energies that are odd multiples of the fundamental laser pulse. As described further in section 2.3.2, it is the recombination of an ionised electron and its parent ion that is used to produce an XUV photon. As this process occurs twice per optical cycle and alternate recombination events have a π phase shift (since the electron is returning from the opposite direction), only odd harmonics are observed. In addition, the spectral widths of the harmonics are generally inversely proportional to the temporal length of the laser pulse. In order to obtain efficient generation, a linearly polarised pulse is generally required [45], although techniques

for increasing the peak intensity at the point of XUV generation by modifying the polarisation have been shown [46]. The generated XUV flux is proportional to I^5 [47], where I is the intensity of the fundamental laser.

Although low-order harmonics are generated, they are usually separated from the high-order harmonics by transmission through a thin metal foil (see section 2.4) and as such the harmonics ∼15 and higher are generally observed on a spectrometer. In addition, the absorption edges of the gas that is used for XUV generation can lead to further attenuation of some low-order harmonics. The laser-to-harmonic conversion efficiency has been measured as ∼4 x 10^{-5} for the 15th harmonic [48]. Harmonics with photon energies higher than 0.5 keV (2.5 nm) [49] have been demonstrated. Generation at these wavelengths is expected to have major implications for diffractive imaging of biological materials as, in the range ∼2 to ∼4 nm, water is transparent whilst carbon strongly absorbs. This spectral region will therefore enable the study of biological materials whilst in a water-based environment.

The generated spectrum can be tailored to individual requirements. Wavelengths can be shifted [28, 50, 51], optimised [29] and temporally altered [52]. The radiation possesses strong spatial coherence [26], and hence does not require aperturing before using for diffractive imaging.

2.3.2 Generation Model

HHG is an extremely nonlinear effect and cannot be approximated by a Taylor expansion of the electric displacement. Therefore a different explanation is needed. The 'three step model' [25,53] employs a combination of quantum mechanics and classical Newtonian physics.

A schematic of the semi-classical three step model explanation is shown

in figure 2.4. Firstly, the intense laser electric field causes the atomic Coulomb potential to distort. This can allow an outer electron to tunnel-ionise away from the atom. Secondly, the ionised electron is treated as a classical particle as it is accelerated away from the parent ion by the laser electric field. When the electric field changes direction, the electron can return to the atom. Thirdly, a photon is emitted at an energy given by the sum of the electron kinetic energy and the ionisation potential of the atom. The maximum photon energy that can be generated is given by,

$$h\nu_{max} = I_p + 3.17U_p \tag{2.8}$$

where I_p is the ionization potential of the gas and $U_p = \frac{e^2E^2}{4m\omega^2}$ is the ponderomotive energy for a laser beam of intensity $\mid E^2 \mid$ and angular frequency ω. The mass and charge of the electron is denoted by m and e. The value of 3.17 arises from the kinetics of the electron in the electric field of the laser.

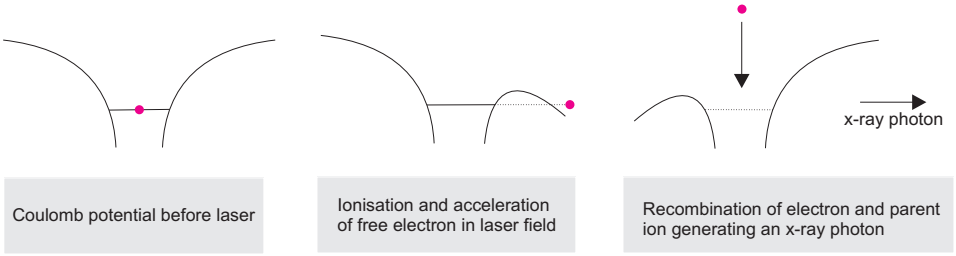

Figure 2.4: *A schematic of the three step model, used to explain High Harmonic Generation.*

To increase the maximum photon energy, either the ionisation potential or the ponderomotive energy can be increased. The first can be increased by selecting a gas with a high ionisation potential. Such an atom will have its outer electron bound tightly, and therefore noble gases are generally used. As shown in equation 2.8, the ponderomotive potential is proportional to

the laser wavelength squared. There is consequently interest in using longer wavelength lasers for XUV generation [54]. The ponderomotive energy can also generally be increased by increasing the laser intensity. However, at higher electric field strengths the magnetic field, which acts in a direction perpendicular to the electric field, can become significant enough to cause the emitted electron to be diverted by nanometers and therefore miss the collision with the parent ion.

2.3.3 Phase Matching

In linear optics, the induced polarisation of an atom is assumed to be linearly proportional to the applied electric field. However, for high intensity electric fields this relationship breaks down and the high-order powers of the applied electric field must be considered. This nonlinear relationship can lead to the transfer of energy between different frequencies. This is the basis behind harmonic generation. In this case, energy is transferred from the fundamental to the harmonic frequency. The energy in the harmonic will only build up while the phases of the two wavelengths are matched. This length is known as the coherence length. After this length, the energy is returned back to the fundamental frequency and the cycle continues. Therefore, to maximise the energy in the harmonic, the coherence length must be increased.

The effect of HHG can be explained using nonlinear optics and hence the concept of phase matching is extremely important. In order to build up a strong XUV signal, the fundamental wavelength and the generated wavelengths must be phase matched. In general they are not, and instead the signal builds up over a coherence length, before destructively interfering. Effective phase-matching is therefore critical for efficient XUV generation.

In this thesis, XUV is generated using either a hollow glass capillary or a small cell, both of which contain low pressure argon gas. The capillary acts like a waveguide for the laser, whilst the gas cell is much larger and hence the laser beam is treated as if it is propagating in free space. The different phase matching conditions for these two methods are now discussed.

In order to generate high intensity harmonics of the fundamental laser, the phase mismatch between the two wavelengths must be minimised. The phase mismatch on axis, Δk, can be expressed as [55],

$$\Delta k = qk_{laser} - k_q = \frac{q2\pi(1-\eta)}{\lambda}\Delta n + P\eta N_{atom} r_e(\frac{\lambda}{q} - q\lambda) + G + A \quad (2.9)$$

where q is the harmonic number, λ is the fundamental wavelength, P, η, N_{atom}, r_e are the gas pressure in atmospheres, ionisation fraction, gas density at one atmosphere, and the electron Bohr radius, respectively. The term, $\Delta n = n_{laser} - n_q$, represents the difference in the refractive index of the medium for the two wavelengths. G and A are the geometric and the atomic phase terms, and are explained below.

The first two terms in equation 2.9 are the material dispersion and the plasma dispersion, and take a positive and negative value respectively. The plasma dispersion value changes through the duration of the pulse as more electrons are ionised. A consequence is that phase matching is only possible below an certain percentage of ionisation. If the ionisation level is above this percentage, no phase matching can occur. Depending on the temporal profile of the laser pulse, this may mean that phase matching is not possible for the most intense part of the laser pulse [56]. Using a shorter laser pulse, which enables a higher electric field strength to be phase matched, may

therefore significantly increase the generated XUV flux.

The sign of geometric term differs for the two XUV generation techniques used in this thesis. Firstly, a waveguide geometry, i.e. the hollow glass capillary, has a negative sign [47]. Secondly, a focussed geometry, i.e. a gas cell, has a positive sign [57]. The atomic phase term, which is related to the paths of the electrons that occur during the generation process, has a sign which is not fixed during propagation as it is related to the intensity through the pulse [58].

Throughout this thesis, the gas pressure at the laser focus is varied until a maximum yield is reached. However, as shown in section 2.3.4, the generated XUV is strongly absorbed by the gas and hence the optimal gas pressure is a balance of both efficient phase matching and minimal gas absorption.

To fully understand the generation process and explain the observed asymmetry in both the shape and spectrum of the XUV output [59], a model must be introduced which includes all the generated XUV wavelengths in three dimensions for all time slices through the pulse. This can be achieved using a split-step model [56], where in each small period in time the XUV generation is calculated along with the change in the ionisation fraction resulting from the fundamental laser. Work to date by group member Rogers has demonstrated good qualitative comparison with experimental results.

2.3.4 Gas Absorption

As the generation process requires the ionisation of an electron, increasing the number of gas atoms at the focus will generally increase the XUV flux. However, the absorption of the XUV photons by the gas atoms must also be taken into account. Ideally, a high density of gas will be present at the focus with a low density after the focus. To illustrate this phenomenon, figure 2.5

shows the transmission through 1 cm of argon gas as a function of pressure, for several XUV wavelengths. The high absorption has two major effects. Firstly, the total XUV flux is generally significantly reduced. Secondly, the difference in attenuation, as a function of wavelength, means that harmonics that have wavelengths longer than ∼30 nm are heavily attenuated. In addition, results have shown that a minimum in the generated spectrum due to the electronic structure of argon occurs for wavelengths in the 24 nm region [60]. Therefore, the XUV multilayer focussing mirror (see section 3.1 for in depth discussion) was selected to have a peak reflectivity at 27 nm.

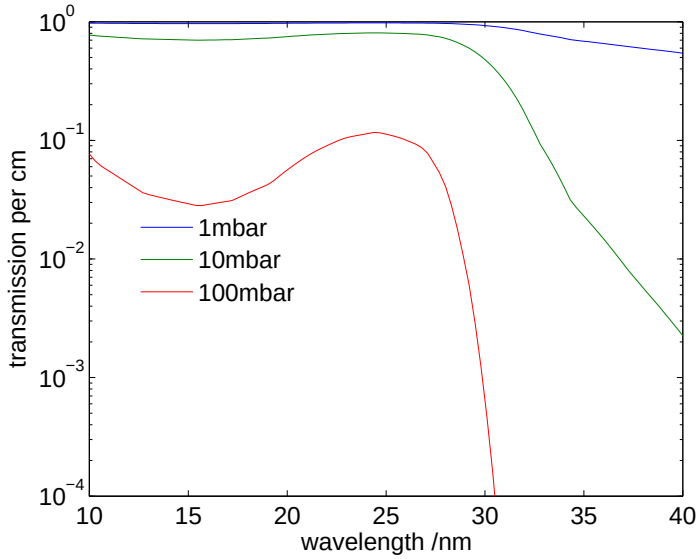

Figure 2.5: *Transmission through 1 cm of argon, at pressures typically used for XUV generation.*

Although not shown, a background pressure of 0.01 mbar results in a average loss of 0.5% for the wavelength range 30 to 40 nm over a distance of 1 cm. A pressure of 0.001 mbar or lower is generally sufficient for propagation over distances greater than 1 cm. The optimal generation pressure is generally in the range 10 to 100 mbar. Methods of reducing the pressure after the point of generation have therefore been investigated, one of which

utilises a short laser-gas interaction region with differential pumping to produce a steep pressure profile. All the generation optics used in this thesis are discussed in section 2.5.

2.4 Separation of the Laser and XUV

The objective of this thesis, to construct a beamline that enables XUV diffractive imaging of nanoscale objects, requires a high flux of XUV radiation. In addition, the laser light, which is used to generate the XUV, must be significantly less intense than the XUV at the diffraction sample. However, the laser and XUV propagate collinearly, and the XUV generation efficiency is $\sim 10^{-6}$. Therefore a significant reduction in the laser intensity must be achieved, with minimal attenuation of the XUV. In this section, two techniques for separating the laser and the generated XUV are contrasted.

The two techniques that are analysed in this section are as follows: Firstly, transmission through a thin metal foil, which heavily attenuates the laser but transmits a large percentage of the XUV, is presented. This method is used exclusively throughout this thesis. Secondly, reflection from a Brewster-angled silicon wafer at the laser wavelength is discussed. This technique reflects the XUV but refracts and absorbs the laser wavelength. Initial results are presented.

Transmission through a Metal

The solution used throughout this thesis, transmission through a metal foil [61], is described here. A 200 nm thick foil of aluminium is generally used, as it attenuates the laser wavelengths by a factor of 10^8 whilst transmitting $\sim$10% of the XUV.

Transmission efficiencies through aluminium for 800 and 30 nm wavelengths are illustrated in figure 2.6. Also shown is the thickness where the XUV flux becomes more intense than the laser flux, if a generation efficiency of 10^{-6} is assumed. The absorption from the aluminium oxide layers on both sides of the aluminium foil [62] are taken into account. The figure shows that the aluminium should be at least 200 nm thick.

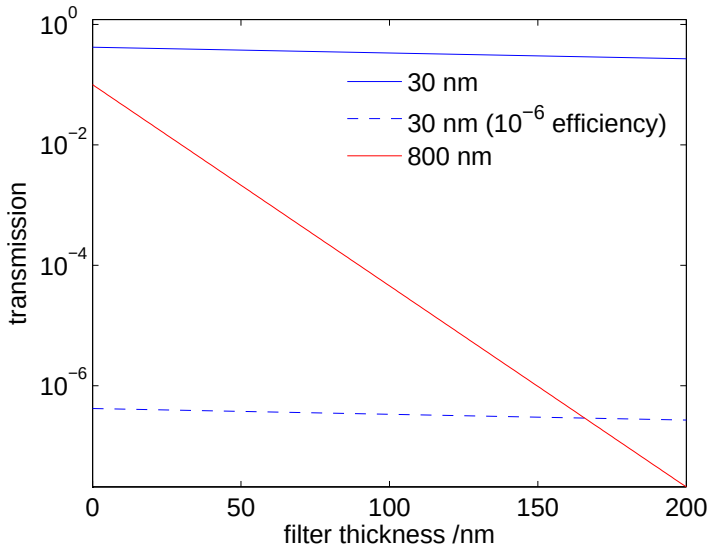

Figure 2.6: *Transmission through aluminium for 30 nm and 800 nm radiation. Also shown are the relative intensities of the laser and XUV radiation given a generation efficiency of 10^{-6}.*

The figure shows that whilst 200 nm foil thickness will result in an order of magnitude more XUV than laser, the total attenuation for the XUV is an order of magnitude. Therefore, alternate methods which achieve large attenuation of the laser but minimise the XUV absorption will be a worthwhile area of investigation in the future.

Polarisation

Light which is p-polarised and incident upon a surface that is positioned at Brewster's angle will in general experience very little reflection. A monochromatic beam, incident on a flat material which has a zero imaginary refractive index component will however reflect zero light. In this subsection, the possibility for separating the laser and XUV by using an appropriately angled silicon wafer is investigated. This technique has been investigated before for separating monochromatic XUV from laser light [63], and also for separating HHG radiation from laser light [64]. In the latter case, a single value for the attenuation of the laser and XUV is given. However, in this section, the concept of refracting polychromatic laser light is explored more thoroughly. As shown in this section, this technique can be used as an accurate diagnostic measurement of the polarisation quality of the laser, which in itself is useful as the HHG process is extremely dependent on the polarisation of the laser.

In order to become a viable alterative to the aforementioned metal transmission method, the laser must be attenuated sufficiently whilst the XUV is reflected. The reflectivity of silicon at XUV wavelengths is ∼0.65 for an angle of 75 degrees [65]. Presented here are experimental results for the laser attenuation when incident upon a Brewster-angled silicon wafer. The silicon wafer is assumed to be flat. The reflectivity for p and s-polarised light at an interface is given by [66],

$$r_p = \frac{\epsilon cos(\phi) - (\epsilon - sin^2(\phi))^{1/2}}{\epsilon cos(\phi) + (\epsilon - sin^2(\phi))^{1/2}} \tag{2.10}$$

$$r_s = \frac{cos(\phi) - (\epsilon - sin^2(\phi))^{1/2}}{cos(\phi) + (\epsilon - sin^2(\phi))^{1/2}} \tag{2.11}$$

where ϵ is the dielectric constant (the refractive index squared) and ϕ is the angle of the interface.

Figure 2.7 shows the reflectivity as a function of angle for a silicon wafer, for the whole laser spectrum, for both p and s-polarisation. The minimum reflectivity corresponds to an angle of ∼75 degrees.

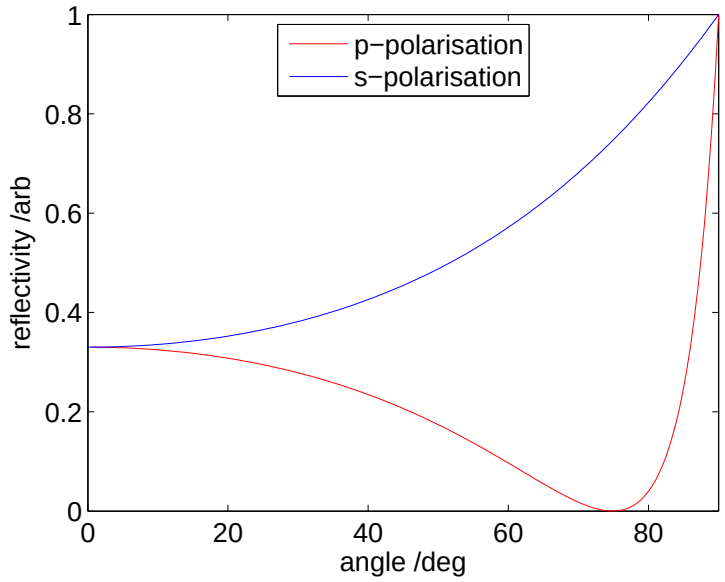

Figure 2.7: *The reflectivity of a silicon wafer, as a function of angle for s and p polarisation, for the entire laser spectrum.*

There are two reasons for a non-zero reflectivity at 75 degrees: the multiple wavelengths result in multiple Brewster angles; and the imaginary component of the refractive index is non-zero. It is useful to observe the effects of the multiple Brewster angles and the imaginary component individually. Figure 2.8 shows the p-polarisation reflectivity for a monochromatic beam (at 791 nm, which is the central wavelength in this case) and the reflectivity for the whole spectrum. The maximum theoretical attenuation for silicon for 791 nm is 1.4 x 10^6. However, the maximum for the whole beam is only 4.1 x 10^5. As the XUV generation efficiency is $\sim 10^{-6}$, even the maximum

theoretical attenuation is not sufficient.

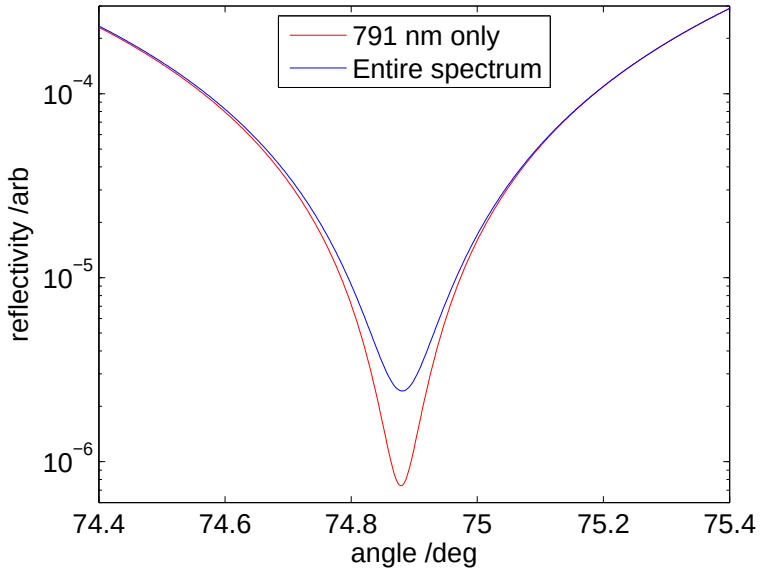

Figure 2.8: *The reflectivity of p polarisation for a single wavelength at 791 nm and for the entire laser spectrum.*

A second silicon wafer, positioned parallel to the first, will further attenuate the laser. However, the attenuation from the second wafer will be less than that achieved for the first, as the spectrum is altered as a result of the first reflection. Figure 2.9 shows the laser spectrum after one reflection.

Figure 2.10 shows the experimentally measured reflectivity (for a single reflection) versus angle for a silicon wafer (circles) alongside the theoretical reflectivity curve for a laser with 99.92% p-polarisation (solid line). The silicon wafer was aligned using two axes of rotation. Firstly, the total reflection was minimised by using both axes, and hence one axis was positioned at 75 degrees whilst the other was perpendicular to the beam. Next, the reflected intensity was recorded at angles near to 75 degrees, using a Vernier scale on a goniometer. The theoretical data was matched to the experimental data by changing the relative ratio of p and s-polarisation. This allows a mea-

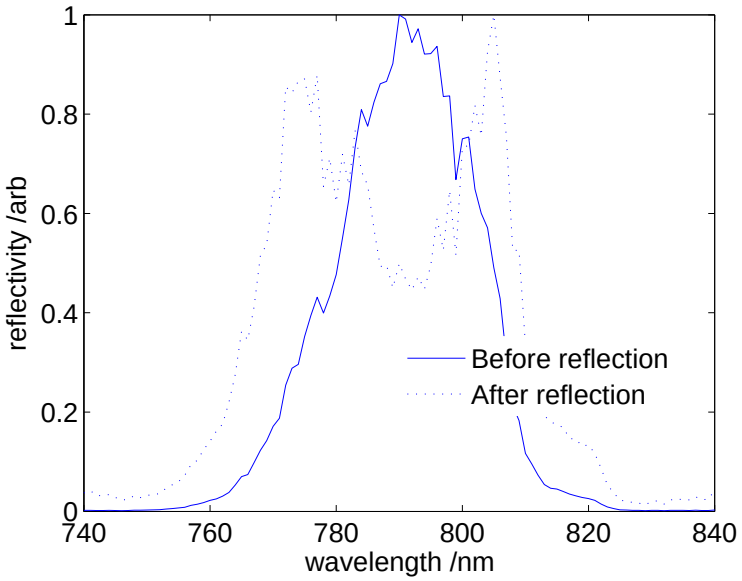

Figure 2.9: *The laser spectrum, before (experimental) and after (calculated) reflection from the silicon wafer. Both spectra are normalised to unity.*

surement of the polarisation of the laser beam, accurate to four significant figures. As the laser beam is not 100% p-polarisated, the maximum intensity attenuation is decreased further. In fact, the maximum attenuation is found to be 1.4 x 10^3, corresponding to a reflectivity of 7.1 x 10^-4.

As the XUV reflectivity at 75 degrees is ∼0.65 and the XUV generation efficiency is ∼10^{-6}, there will be roughly one thousand laser photons for every XUV photon if a single reflection is used. This is not sufficient for the separation of the laser and the XUV, and hence, based on this data, the current method of transmission through a thin metal film is more effective. If a second wafer was used, the total laser attenuation would be less than 2.8 x 10^6, leading to a best case scenario of 0.78 laser photons for every XUV photon. This is still not adequate for XUV diffraction, and hence using reflection from a silicon wafer to separate the laser and the XUV is not a feasible solution.

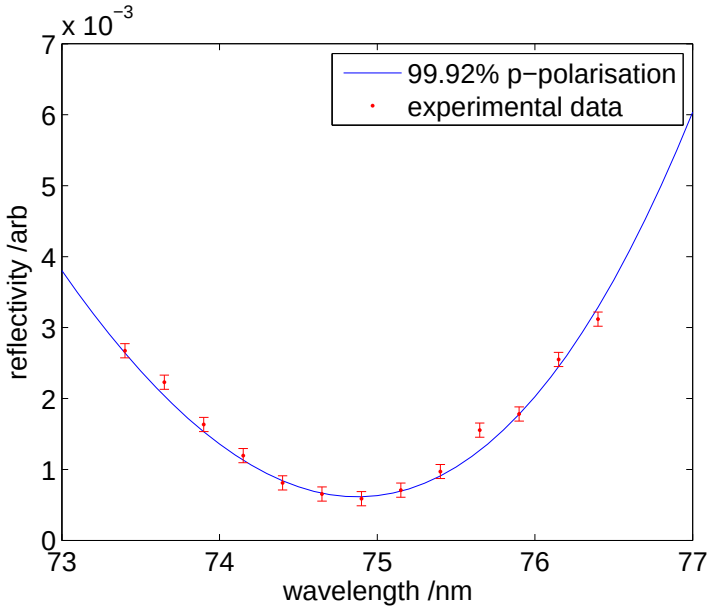

Figure 2.10: *The experimentally observed reflectivity as a function of angle (circles) and the theoretical reflectivity (solid line) using the experimental spectrum and assuming a p polarisation of 99.92%.*

In this case, the error bars correspond to the instability of the laser output power, which at the time was observed to vary on the power meter by +/- 10% in an oscillating movement over a period of around sixty seconds. The 99.92% line corresponds to a best fit line through this data.

2.5 Diffraction Beam Line Overview

In this section, a description of the four different experimental setups that were used during this thesis is given. The hollow capillaries were designed by group members Froud and Praeger. The gas cell was designed by group member Grant-Jacob. The gas tube and the associated vacuum pumping setup is my own design. All experimental measurements were taken by myself. Only a brief discussion is given for the standard apparatus such as the gas injection system and the vacuum electrical feedthroughs. Two theses

by group members Froud [67] and Praeger [68] provide further information.

There are several key points for the design of a HHG diffraction setup. A schematic for the setup, which illustrates focussing using a multilayer mirror and a parabolic hollow fiber, is shown in figure 2.11.

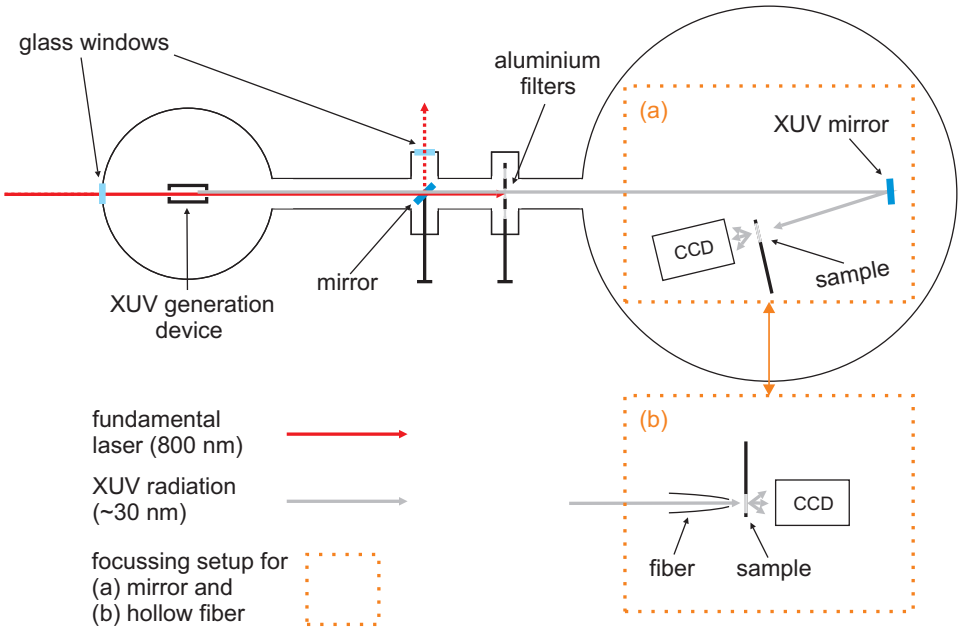

Figure 2.11: *Schematic for HHG diffraction experiments, showing the focussing arrangement for a multilayer mirror and a hollow fiber.*

Firstly, as XUV is strongly absorbed in air, the entire generation and diffraction setup must be kept under vacuum, ideally below 0.001 mbar. Secondly, all light at the point of generation must pass through the 200 nm thick aluminium foil before hitting the diffraction sample and CCD, to ensure that no laser light is present on the sample. Therefore, the vacuum system contains two chambers. The first small chamber contains the XUV generation components. The second large chamber contains the sample, CCD, and a number of externally controlled actuators. The two chambers are separated by the aluminium foil. Thirdly, a moveable mirror, positioned before the aluminium foil, is used to reflect the laser light through a glass

window and provide throughput measurements to help with alignment.

There are three different generation devices used in the thesis. Each are positioned at the focus of the laser, kept under vacuum and attached to a gas input line. The generation devices consist of: a hollow glass capillary (both 7 cm long and 5 cm long variants were tested), a perspex gas cell, and a metal gas tube. Schematics of these devices, along with approximate gas pressure profiles, are shown in figure 2.12.

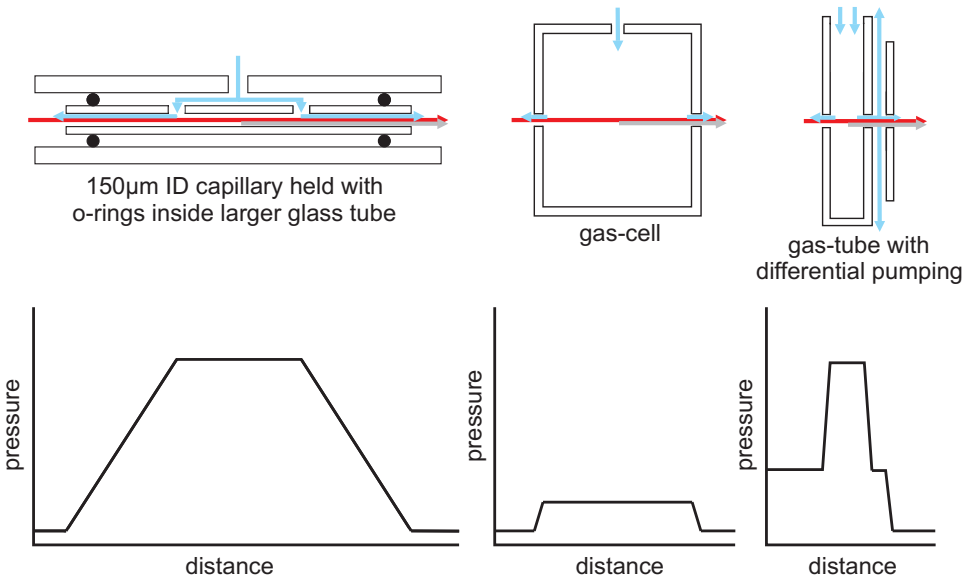

Figure 2.12: *Top: The different generation devices used during this thesis, showing capillary, gas cell and gas tube. The paths of the fundamental laser (red), generated XUV (grey) and gas flow (blue) are shown. Bottom: The relative gas pressure profiles achieved along the central axis of the generation devices.*

The capillaries have an internal diameter of 150 μm, and two gas inlet holes drilled into the side, positioned at the middle of the capillary but separated by 2 cm. The 7 cm capillary was set up with a manual alignment rig that was designed by Froud [67] and Praeger [68]. The 5 cm capillary was mounted inside a small vacuum chamber, designed by myself, and electronically aligned using a five axis stage, allowing for more accurate movements.

The coupling of light into a hollow capillary is profoundly dependent on the choice of focussing lens. The spot size to bore size ratio (w/a) determines which capillary modes [69] are produced, and as different modes have different propagation losses, the maximum throughput of a hollow capillary is a function of this ratio. A high throughput is desired as the XUV intensity is dependent on the laser intensity inside the capillary. For efficient coupling, a ratio of $\sim$0.64 is required [70]. Consequently, the laser M^2 parameter must be known for effective XUV generation (see section 2.2.3 for a discussion on the laser beam quality).

The gas cell is 2 cm long and has 500 μm diameter apertures either side. The gas inlet tube is connected directly into the cell. The gas cell used was a modified version of that designed by Grant-Jacob [71], and was mounted identically to the 5 cm long capillary.

The gas tube is a 4 mm wide copper pipe with two large holes drilled through the walls. Along the core of the pipe, one end is sealed and the other acts as the gas inlet. The gas cell is mounted statically inside the small chamber and wrapped tightly with PTFE tape. The laser is used to ablate the PTFE on both sides of the gas tube, effectively forming a 4 mm long region of constant gas pressure. Approximately 5 mm after the gas tube, a second piece of tape is ablated to provide a small aperture. Both sides of the latter aperture are vacuum pumped separately, and hence the aperture acts to create a pressure differential. The tape needs to be replaced only when the system is modified. As the laser is used to form the apertures, no alignment is required. As the generated XUV is a shorter wavelength than the laser, and therefore diverges less, the XUV is not clipped by the laser ablated apertures.

There are two different XUV focussing devices used in this thesis, a

hollow glass fiber and a multilayer mirror. The fiber is parabolically shaped, and focusses light through the phenomenon of total external reflection. The multilayer mirror has a spherical profile and focal length of 25 cm. Both are discussed in depth in chapter 3.

The four experimental setups are distinct as they use different combinations of generation devices and focussing optics. They are, in terms of the generation and focussing techniques: 1) a 7 cm long capillary with hollow fiber, 2) a 5 cm long capillary with multilayer mirror, 3) a 2 cm long gas cell with multilayer mirror, and 4) a 4 mm wide gas tube with multilayer mirror. The combination 1) was conducted with a 35 fs, 1 W laser, whilst combinations 2-4 used the 40 fs, 1.5 W output from the laser described in section 2.2. The 1 watt laser is discussed in [67] and [68]. As the output of the two lasers are similar, a comparison can be made between the four experimental setups.

Table 2.1 shows a summary of the data for the four experimental arrangements. Although there is data for only four of the possible combinations of the laser, generation device, and focussing device, several important points can be made. The XUV flux is the number of photons per second, measured at the XUV focus. The flux for the gas tube was measured 20 mm away from the focus and hence the spot size has not been measured. However, it is likely to be very similar to the gas cell as they are both free space generation techniques.

Firstly, the smallest focus is produced by the hollow fiber. Secondly, a comparison of a capillary and a gas cell shows that, whilst the capillary produces a larger focus, the total flux is greater. The intensity at the centre of the focus for the gas cell is however measured to be 3.5 times greater, due to the smaller spot size. Thirdly, although the focus for the gas tube

was not measured, a flux measurement shows that it is 15,000 times greater than the gas cell. As shown in chapter 3, the multilayer mirror and hollow fiber have total reflectivities of 6% and 35% respectively. The low value for the mirror is due to a reflectivity bandwidth that is considerably narrower than the generated XUV spectrum.

As discussed in section 2.3.4, a high gas density is desirable at the laser focus. However, due to the XUV absorption by the gas, the density should be reduced after the focus. The following paragraphs describe the gas density profiles in the three different type of XUV generation devices used in this thesis.

The central section of the capillaries can reach a pressure of up to 200 mbar as the gas conductance from the gas inlet holes to the capillary exit is low. Therefore a relatively high pressure can be maintained inside the central region of the capillary whilst the vacuum chamber holding the capillary can remain at a low pressure. However, the linear pressure drop off towards the exit means that much of the generated XUV is absorbed. Therefore the observed XUV is generated towards the end of the device.

The gas cell, which has 500 μm diameter exit apertures, has a very high gas conductance, and hence the gas pressure inside the gas cell can only be increased to around 10 mbar. A higher pressure would leak a large amount of gas into the surrounding area, resulting in high absorption for the entire

Table 2.1: *Generation conditions and focus measurements for the different experimental setups. The columns labelled flux and focus refer to the XUV flux at the XUV focus and the size of the XUV focus respectively.*

laser	generation	focussing	flux (/s)	focus (ω_0)
1 W, 35 fs	7 cm capillary	hollow fiber	2.2 x 10^6	17 μm
1.5 W, 40 fs	5 cm capillary	multilayer mirror	3.2 x 10^7	32 μm
1.5 W, 40 fs	2 cm gas cell	multilayer mirror	1.5 x 10^7	22 μm
1.5 W, 40 fs	4 mm gas tube	multilayer mirror	2.3 x 10^{11}	n/a

vacuum chamber. Although the maximum pressure is relatively low, which results in a relatively low XUV flux, the pressure drop off is fast and hence the absorption is low. These opposite effects lead the gas cell to have a similar measured flux to the capillary.

The gas tube, which utilises differential pumping, takes the benefits from both the capillaries and the gas cell. Firstly, the exit apertures are small, which allows a high pressure of up to 200 mbar inside the gas tube. Secondly, the differential pumping reduces the pressure rapidly, and hence the XUV absorption is low. This has resulted in a significantly higher flux at the focus.

The ease of use and reliability of the generation devices, although of secondary importance, are also worth considering. The capillary requires efficient coupling through the use of a specifically sized focus. It can therefore require a significant amount of time to align. The gas cell, due to its fixed apertures, still requires alignment. The gas tube however, requires no alignment as the laser is used to produce the entrance and exit apertures. Therefore the apertures are exactly aligned with the path of the laser and generated XUV. The gas tube is therefore both the easiest to set up, and produces by far the highest flux. This argument is however based on maximising the total flux. If other factors are important, for example the tunability of the generated XUV spectrum [28], a different device may be optimal.

2.6 XUV Detection: Charge Coupled Devices

In order to understand the diffraction patterns that are recorded on the XUV CCD, the processes involved with the data recording must be fully understood and the limitations quantified. In this section the nonlinearity

and sources of noise are discussed.

The CCD has an image sensor consisting of a 1024 by 1024 array of 13 μm diode capacitors, which collect a charge that is proportional to the number of photons incident on the diode. After a specified time, shift registers pass the charge along to the edge of the chip where it is recorded and an intensity image is generated. For XUV wavelengths, the quantum efficiency is ~ 0.6. The CCD is connected to a water cooling system situated outside the vacuum chamber through the use of a flexible copper braid. Indium is used to increase the thermal conductivity between the connections.

2.6.1 Nonlinearity

In general, the photon count on a CCD is only proportional to the photon flux for a limited number of counts, corresponding to a linear response. As the charge inside a capacitor tends towards the maximum, charge will tend to leak, corresponding to a reduced photon count. A linearity measurement is therefore critical, as a diffraction image that has data outside this region will be misleading, unless accounted for. By recording an XUV image on the CCD for increasing integration times, a set of identical images that are scaled in intensity were recorded. The relationship between the integration time and the pixel count was then used to quantify the CCD linearity. An image was recorded for 10, 50, 100, 500, 750, 1000 and 1250 ms. Figure 2.13 shows the five highest pixel counts for each image, for each integration time. The CCD is shown to have a linear response over more than 90% of the maximum pixel count. Therefore, no adjustments will need to be made to diffraction images recorded using this CCD on the condition that the maximum pixel count is below 90% of the maximum.

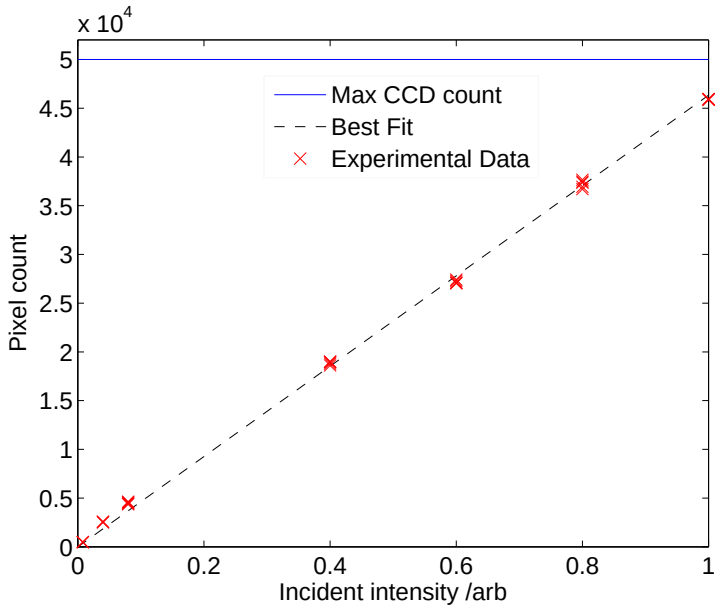

Figure 2.13: *Recorded pixel intensity versus relative incident flux, showing that the CCD has a linear response for more than 90% of the dynamic range.*

2.6.2 Sources of Noise

An output from a CCD that has no incident light is subject to two random noise sources: readout and dark current. The readout noise is a consequence of converting an analogue signal to a digital output and is independent of integration time and CCD temperature. Dark current noise results from the thermal energy in the CCD which can randomly produce electrons that are counted as signal. Dark current noise is dependent on both integration time and temperature, but can be made negligible by reducing the CCD temperature.

In order to remove the stray laser light from the XUV diffraction images, a CCD image taken with no gas present is background subtracted from each experimental dataset. Gas is required for XUV generation but does not significantly change the properties of the laser leakage, which generally corresponds to laser light that has passed through micron-sized pinholes in

the aluminium filters.

It is important to calculate the CCD temperature which corresponds to a level of thermal noise that is insignificant, as this is the required temperature for all experiments throughout this thesis. For this experiment, 10,000 pixel counts were recorded for a series of temperatures (-50 to 20 °C in steps of 5 °C) and for three integration periods (0.1, 1, and 10 seconds). No light was incident on the CCD. The standard deviation of the pixel counts, for each combination of temperature and integration period, are shown in figure 2.14.

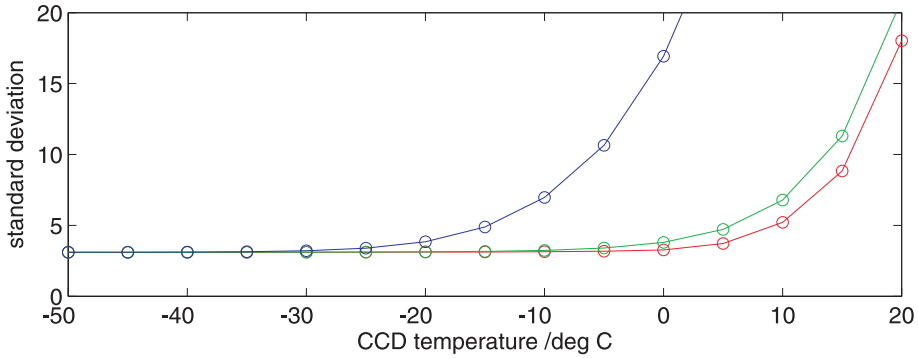

Figure 2.14: *Standard deviation of photon counts on the CCD with no incident light, for 0.1 (red), 1 (green) and 10 (blue) seconds, showing that the thermal noise, which is a function of time, is negligible for temperatures* $\leq$ *40° C.*

For temperatures $\leq$ -40 °C, the data corresponding to the different integration times overlap, and hence for this temperature the time dependence of the CCD noise is negligible. The value of 3.5 corresponds to the stated deviation of the readout noise, which is independent of time. Therefore, throughout this thesis, the CCD temperature has been held at -40 °C. Where the CCD noise has been required for data simulations, it has been approximated by a Normal distribution with a standard deviation of 3.5.

2.7 Conclusion

This chapter has provided a background to the science and technology needed to construct a HHG radiation source, and has discussed the generation, absorption, and detection of the XUV, together with the removal of the fundamental laser wavelength.

The most important step to achieving the objective of the project, single molecule scattering, is to increase the flux at the sample. Therefore the optimisation of the the generation and the focussing setup are of critical importance. This chapter has presented details on the generation of the XUV, in particular the importance of both a high gas pressure at the point of generation and of a low gas pressure after generation to minimise absorption. Focussing results are presented in detail in chapter 3.

A comparison of different generation and focussing techniques has illustrated that orders of magnitude improvements in flux are possible and that a comprehensive comparison is now required. Calculations have shown the importance of the gas density profile inside the generation device. The technique which uses differential pumping represents a significant step forward in the progress of this project.

An investigation into the viability of using a Brewster-angled silicon wafer to separate the laser and XUV has shown excellent comparison with theoretical calculations, and has enabled an accurate measurement of the polarisation of the laser. However, the technique will not be used, as the laser attenuation is less than currently achieved with a thin metal foil.

A thorough analysis of the XUV CCD has been presented. It was found to have a linear response for more than 90% of its dynamic range and to have a thermal noise which is insignificant for temperatures $\leq$ -40 °C.

Chapter 3

XUV Focussing

A critical factor in the aim of single molecule scattering is the ability to focus the extreme ultraviolet (XUV) radiation down to a size scale similar to the sample being investigated. This is because the number of scattered photons is generally proportional to the irradiance and therefore to observe a high signal to noise scattering pattern the number of photons incident on the sample must be maximised. However, due to the small variation in the real part of the refractive index between different media and vacuum, and the short absorption lengths for nearly all materials, optics that work by refraction are not effective. There are in general three distinct alternatives available for focussing XUV wavelengths, as shown in figure 3.1.

Firstly, the zone plate focusses light by either attenuating the intensity or imparting a phase delay on the incident beam at specific positions. The structure of the zone plate is designed so that there is only one point where all the possible beam paths for a single wavelength constructively interfere. This corresponds to the optic focus, where the focus quality depends on the accuracy of the zone plate fabrication. Imaging resolutions better than 15 nm have been demonstrated for 250 eV ($\sim$5 nm) to 1.6 keV ($\sim$0.7 nm) [72].

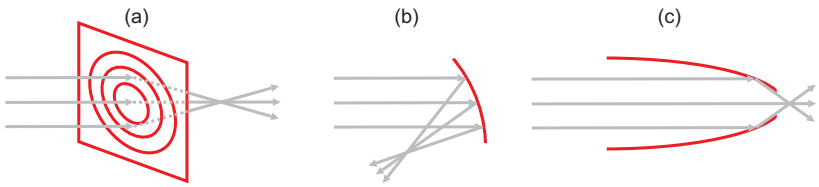

Figure 3.1: *Typical methods for focussing XUV radiation: a) zone plate, b) multilayer mirror, c) parabolic hollow fiber.*

When used on a High Harmonic Generation (HHG) source, the different harmonics would however be focussed to different positions, which could be useful if a single wavelength focus was required, but is a disadvantage due to the decrease in irradiance at each single wavelength focus.

Secondly, the focussing mirror simply reflects the incident light towards a focal point. The XUV reflection at normal incidence from a single layer of material is generally very low. However, by building up thin layers of alternating mediums, so that the reflected waves constructively interfere, a larger reflectivity can be achieved. Molybdenum/Silicon (Mo/Si) mirrors have been shown experimentally to achieve ∼60% with a maximum theoretical value of ∼76% for 13.0 nm radiation [73]. However, the reflectivity at other wavelengths generated by HHG is lower. The high absorption limits the number of periods, normally to around thirty. This technique is useful as it reflects all, or just some wavelengths, to a single focus, depending on the fabrication parameters. The multilayer period and ratio between the sub-layers enables a large choice for both the peak reflectivity and the reflected bandwidth. As the focussed beam must be reflected back at a slightly different angle to the incident beam, a mirror with spherical profile

will always produce an astigmatic focus. This abberation is demonstrated in section 3.1.3 where the spatial profile of the XUV beam is analysed when a spherical mirror is used. To remove this abberation, a mirror with an off-axis paraboloidal profile can be used. This option, however, is generally an order of magnitude more expensive and as such it is important to determine exactly when the additional cost is required. An alternate method to a normal incidence mirror, known as a Kirkpatrick-Baez mirror [74], uses a glancing reflection off two independently controlled mirrors to focus a light source. The incident beam is focussed in one plane by the first mirror, and then in the orthogonal plane by the second mirror. Foci smaller than ~ 40 nm have been demonstrated [75] on hard X-ray sources.

Thirdly, the focussing fiber works by the principle of total external reflection, where light that is incident at a glancing angle upon a medium will in general be reflected with little loss. Using this principle of a high reflectivity at angles less than the critical angle, effective X-ray optics can be made. A common technique is to fabricate a hollow fiber which has a entrance aperture larger than its exit. This principle has been extended to include both single and bundles of hollow fibers [76] with profiles that are generally linear or parabolic [77]. A linear profile will increase the irradiance at the exit through multiple reflections, whereas a parabolic profile will ideally reflect all possible ray paths towards a single focus that exists some distance after the exit aperture. As a hollow fiber will focus all XUV wavelengths to a single focus, it will focus the wide spectrum that can be generated using a HHG radiation source.

Presented in this chapter are experimental results from using a spherical multilayer mirror and a parabolic hollow fiber to focus HHG radiation.

HHG radiation has been focussed to a spot size of 1 μm using an off-

axis paraboloidal multilayer mirror [78]. There are no published results for using a hollow fiber to focus HHG radiation. However, there does exist a wealth of information for synchrotron sources. Originally reported by Stern et. al. [79] with a 10 μm spot size, nanometer foci are now possible [80]. An imaging resolution of 30 nm [81] and $\sim$80 nm [82] has been achieved using a zone plate for synchrotron and high harmonic radiation sources respectively.

3.1 Spherical Multilayer Mirror

In this section, focussing results for a Mo/Si spherical mirror that has been used in an off-axis arrangement are presented, along with extensive analysis of the resulting astigmatic focus and its consequence on diffractive imaging. The spherical mirror produces a vertical and a horizontal focus, which are separated by a circle of least confusion (CLC). A theoretical model is used to show that the most intense position through the focus depends on the horizontal and vertical beam quality and that if the mirror radius of curvature (ROC) is increased, a smaller focus may be achievable as a smaller off-axis mirror angle will be possible. Additionally, it is shown that the phase at the CLC is strongly saddle-shaped. However, as explained in this chapter, this phase distortion cannot explain the significant interference peak splitting that is experimentally observed in diffraction patterns that are recorded using this focussing setup. To illustrate the observed peak splitting, an XUV far-field diffraction pattern that corresponds to an array of 196 nm diameter polystyrene spheres is shown in figure 3.2. This figure is repeated later in section 3.1.4 where it is proposed that the XUV beam quality is degraded upon reflection from the multilayer mirror and it is this asymmetric phase distortion that causes the diffraction peak splitting.

This section is organised as follows: The experimental setup is explained

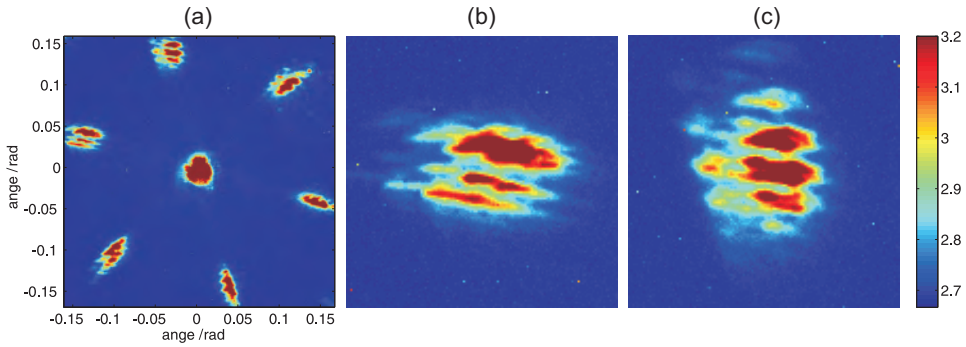

Figure 3.2: *Experimentally observed diffraction pattern from a single layer hexagonal array of 196 nm diameter polystyrene spheres, showing the a) whole diffraction image, b) left interference peak and c) top interference peak. This figure is identical to figure 3.13.*

in section 3.1.1, along with the reason for the off-axis focussing arrangement. Experimental reflectivity results are used here to determine the mirror parameters. In section 3.1.2, an introduction is given to the beam propagation theoretical model, which uses ABCD matrices to calculate the effect on the intensity and phase upon reflection from an off-axis spherical mirror. Section 3.1.3 presents experimental results, which are analysed using the aforementioned model. This is a substantial section and consists of the extraction of the XUV beam quality, the spatial intensity and phase profile through the focus, and the effect on the focus of changing the mirror ROC and angle. All results indicate that the mirror surface decreases the beam quality. Finally, section 3.1.4 demonstrates the effect of large-scale deviations from a spherical profile. Here it is found that deviations in the mirror surface as small as a few nanometers can produce both the interference peak splitting that is observed experimentally and also the observed decrease in beam quality. This result therefore confirms earlier expectations that the beam quality is decreased upon reflection from the multilayer mirror.

3.1.1 Experimental Setup

For the results presented here, the 5 cm long hollow generation capillary (see section 2.5) with an argon pressure of 70 mbar was used to produce the XUV. By using appropriate coupling techniques, laser transmission percentages of 60% were achieved. Inside the main vacuum chamber, a Mo/Si multilayer spherical concave mirror, with a ROC of 500 mm, was used at an incident angle of ∼10 degrees to focus the XUV beam down to a spot size of 30 μm. Here, the definition of spot size (w_0) is that given by Svelto [83], and describes the radial distance over which the intensity reduces from its maximum to $1/e^2$ of its maximum. The spot size therefore corresponds to the radius of the beam. The spatial intensity profile is recorded using the water-cooled XUV charge coupled device (CCD) camera, which is moved in steps of 1 mm through the focus in a direction parallel to the XUV propagation, with typical integration times of 100 ms. Figure 3.3 shows this experimental setup. The mirror angle is the minimum possible for the experimental geometry and is limited by the width of the camera.

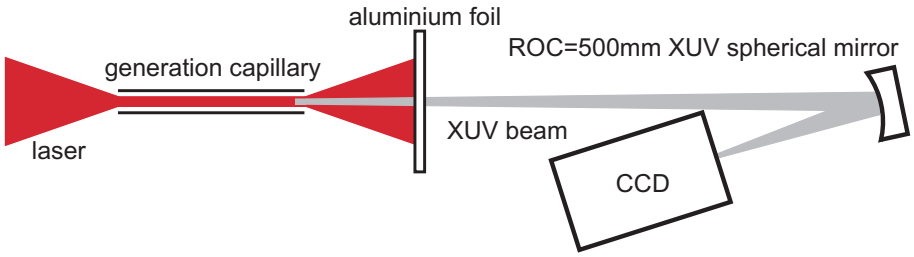

Figure 3.3: *Schematic of the experimental setup for the multilayer mirror.*

On separate experiments using the same input laser intensity and gas pressure inside the generation capillary, the spatial profile of the XUV beam at the position of the mirror and the XUV beam at the mirror focus have been recorded. This has enabled the total reflectivity of the mirror to be

calculated at 6%. This low value is due to a wide generated spectrum and a narrow reflected bandwidth. The quoted peak reflectivity is 20% for the wavelengths 26.7 ± 0.3 nm. By using the observed reflected XUV spectrum, as shown in figure 3.4, and the refractive index values given by [65], the multilayer periods have been calculated to be 15 nm with a Mo/Si ratio of 0.4 to 0.6.

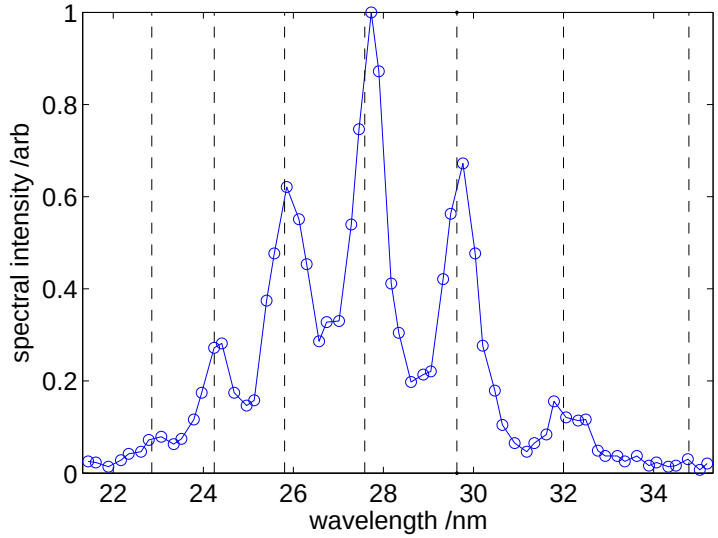

Figure 3.4: *XUV spectrum from the multilayer focusing mirror. The vertical dashed lines correspond to odd harmonics of 800 nm.*

The usual technique for measuring the spectrum of a polychromatic beam is propagation onto an angular dispersive optic such as a grating, followed by a CCD. To measure the spectrum from the XUV focusing mirror, a crystalline sample with a period of 196 nm was used to diffract the XUV onto a CCD. This diffraction sample, and associated diffraction pattern, is discussed further in chapter 5. However, in this section we are only concerned with the mirror reflectivity as a function of wavelength. Due to splitting in the diffraction pattern, which can be explained by modelling nanometer sized defects in the mirror surface (see section 3.1.4), the ob-

served spectral widths are likely to be larger than the actual values.

3.1.2 Beam Propagation Theory

In this section the theoretical framework for analysing an astigmatic beam is presented. By modelling the experimental results with a 3D intensity and phase model, the beam quality and the interdependence of the experimental parameters can be explored.

A spherical mirror at normal incidence (zero angle) has the same ROC for both the horizontal (x) and vertical (y) axes. However, for a non-zero angle, both the effective x and y ROC change. The consequence is the presence of distinct vertical and horizontal line foci, which are separated by a circle of least confusion (CLC). It is important to realise that although the intensity profile at the CLC is circular, the phase is not flat. This is a simple consequence of different values for the x and y ROC. Treating the x and y axes separately at the CLC, one axis is diverging and one is converging, and therefore the phase at this position is saddle-shaped.

The assumptions for this model are that the light beam always diverges at an angle that satisfies the paraxial approximation ($\sin(\theta) \simeq \theta$), and that the beam is monochromatic. Although the wavelengths in the generated beam have a spectral bandwidth ($\lambda/\Delta\lambda$) of roughly two, the narrower band of wavelengths that are focussed by the mirror has a value greater than ten, and hence can be treated as a monochromatic source. This theoretical approach models the light beam as a Gaussian beam. However, the theory can be adapted to higher order propagation modes by introducing the M^2 beam quality parameter, which quantifies how much faster the modelled beam diverges when compared to a diffraction-limited beam. For this analysis, the complex beam parameter q is constructed, and defined as,

$$\frac{1}{q} = -\imath\frac{\lambda}{\pi w^2} + \frac{1}{R} \tag{3.1}$$

where λ is the wavelength, w is the beam spot size, and R is the radius of curvature. The complex beam parameter therefore includes local information on the beam size and the degree of convergence or divergence.

The complex beam parameter after an optical element (q') is related to the parameter immediately before the element (q) by,

$$q' = \frac{Aq + B}{Cq + D} \tag{3.2}$$

where the constants A to D are defined by the type of optical elements.

The system to be modelled here (as shown in figure 3.3), starting from the point of generation inside the capillary, consists of propagation through free space, reflection from a spherical mirror positioned off-axis, and propagation through free space. The spherical mirror profile is modelled as a parabolic surface, as the spherical aberration in this case is negligible. However, the astigmatism is non-negligible, and hence this theoretical model describes the focussing ability of a mirror with a parabolic profile which is arranged off-axis. This is equivalent to the experimental setup shown in figure 3.3. As mentioned earlier, the ROC imposed on the beam by the mirror is different for the x and y axes. Equations 3.3 and 3.4 show the form of the two system matrices for the two axes,

$$\begin{pmatrix} A & B \\ C & D \end{pmatrix}_x = \begin{pmatrix} 1 & L \\ 0 & 1 \end{pmatrix} \begin{pmatrix} 1 & 0 \\ -2/R_x & 1 \end{pmatrix} \begin{pmatrix} 1 & z \\ 0 & 1 \end{pmatrix} \tag{3.3}$$

$$\begin{pmatrix} A & B \\ C & D \end{pmatrix}_y = \begin{pmatrix} 1 & L \\ 0 & 1 \end{pmatrix} \begin{pmatrix} 1 & 0 \\ -2/R_y & 1 \end{pmatrix} \begin{pmatrix} 1 & z \\ 0 & 1 \end{pmatrix} \tag{3.4}$$

where $R_x = Rcos(\theta)$ and $R_y = R/cos(\theta)$. L is the fixed distance between the generation capillary and the mirror, θ is the angle that the mirror deviates from the propagation direction, and z is the distance from the mirror to a position through the focus, which in this case can be varied in order to provide the complex beam parameter at any position through the focus. These calculations are for a mirror that reflects light back at the same height but different yaw angle, i.e. a mirror that has been rotated about a vertical axis.

3.1.3 Analysis of the Astigmatic Focus

In this section, results that show the intensity profile in steps of 1 mm through the focus are analysed using the beam propagation model. From this data, all necessary parameters can be accurately extracted.

This section is outlined as follows. Firstly, the method for determination of the beam parameters is presented. Of particular interest is the beam quality parameter (the M^2 value) which is shown to be increased upon reflection from the XUV mirror. Secondly, the theoretical model is used to optimise the focussing arrangement for both intensity and spot size. Thirdly, the theoretical phase is mapped onto the theoretical intensity profiles through the focus, showing that the phase shift is large but symmetric, and therefore the phase variation cannot explain the experimentally observed diffraction peak splitting.

Beam Quality Calculation

In this section it is shown how the mirror angle, beam M^2, and the spot size inside the capillary where the XUV is generated can be determined from the intensity profile of the XUV beam through the astigmatic focus. Figure 3.5 shows the experimentally measured spot size for the horizontal (blue circles) and vertical (red circles) axes. The error bars in this figure are a result of the deviations in the size of the XUV beam, at a fixed distance through the focus. It has been previously calculated to be approximately 10%. This is the error shown on the figure. The deviations in size result from small changes in the laser intensity at the point of XUV generation; a higher intensity will ionise a larger volume of gas atoms, producing a larger source size and hence a larger XUV focus.

The line foci correspond to points of inflexion in the data. The vertical focus exists at 0.247 m, the CLC at 0.250 m, and the horizontal focus at 0.254 m. The theoretical curves (solid lines) are calculated by using the aforementioned ABCD matrix model and were best fit by eye. This approach is more accurate than simply fitting the data points for the individual axes to a Gaussian beam propagation equation as the angle of the mirror changes its apparent curvature for each axis, and hence all the parameters are to some extent interdependent. Firstly, the mirror angle affects the relative separation of the line foci and can therefore be easily determined. It does however have a secondary effect on the ROC for the two axes and hence must be calculated first. Once the angle has been determined, both the beam M^2 and the focussed spot size can be uniquely determined. As the generation and focussing geometries and distances are known, the calculation of these parameters enables the size of the XUV focus at the point of generation inside the capillary to be deduced. The mirror angle and capillary spot size

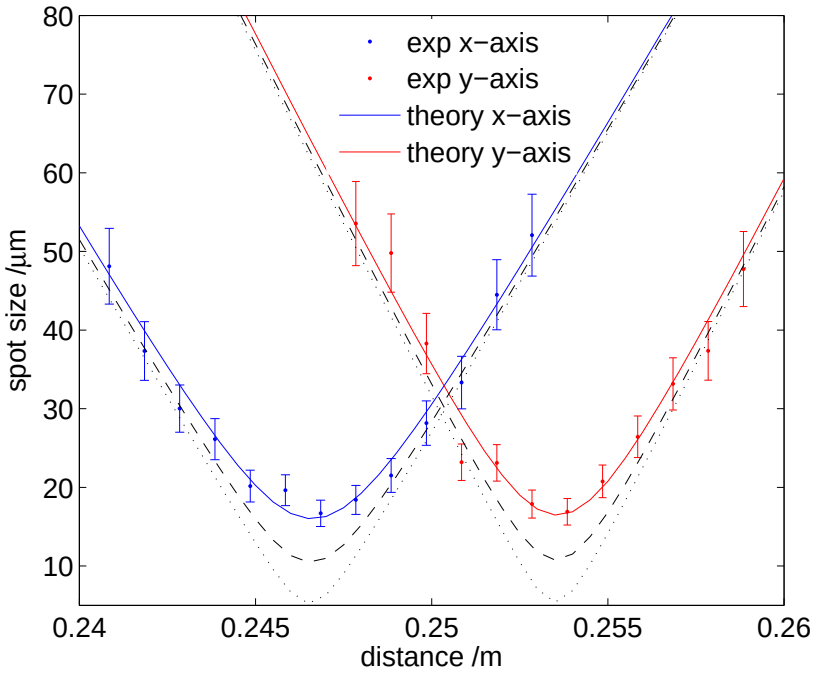

Figure 3.5: *Experimentally observed horizontal (blue circles) and vertical (red circles) spot sizes through the astigmatic focus. The solid lines correspond to a mirror angle of 9.55 degrees and M^2 values of 14 and 16.1 for the two beam axes. Also shown is the effect on the beam size if the M^2 increase by the mirror was only to 10 (dashed line) and 5 (dotted line). The figure shows that a reduced M^2 will not significantly decrease the spot size at the CLC, and therefore instead the astigmatism is the limiting factor.*

are determined to be 9.55 ± 0.1 degrees (directly observed by eye to be 10 degrees) and 65 ± 5 μm. The M^2 in the horizontal and vertical axes are 14.0 ± 1 and 16.6 ± 1.

The analysis above implies that the XUV at the point of generation inside the capillary has a radius of 65 ± 5 μm. This is unlikely for the following reason. The XUV is generated only where the fundamental laser light is sufficiently intense to ionise an electron. As the boundary conditions for an electric field inside a hollow dielectric capillary result in zero intensity at the edges [69] and the high-order capillary modes are lossy and therefore do not exist at the XUV generation point towards the end of the capillary, the XUV beam must be significantly smaller than 65 μm. Calculations using Keldysh ionisation theory [84] have shown that for an identical setup, the theoretical XUV spot size is 15 μm [43].

Using the ABCD matrix framework and working backwards from the data in figure 3.5, the size of the XUV beam at the position of the multilayer mirror can be calculated. Using this and the calculated generated spot size of 15 μm gives an M^2 value of 3, where the sensitivity on the generated spot size is such that 15 ± 5 μm implies a generated XUV M^2 of 3 ± 1. The generated M^2 is therefore different to the value measured at the focus. The likely reason here is that, although the surface roughness of the multilayer mirror is sub nanometer, the surface figure of the mirror is such that a variable phase shift is imparted upon the XUV beam, causing the beam quality to be degraded. The quoted surface figure of $< \lambda/10$ at 633 nm corresponds to a value of 2λ at 30 nm, and therefore a significant phase shift could occur across the XUV beam should the mirror surface deviate at the point of illumination. A model used to quantify this proposition is presented in section 3.1.4. However, as shown in figure 3.5, if the proposed

increase in the M^2 was only to 10 (dashed line) or 5 (dotted line) instead of ∼15, the spot size at the CLC would only decrease in size by a few microns. Instead, the astigmatism is the limiting factor for the spot size. The relationship between the spot size and the mirror angle is discussed further in the next section.

Astigmatic Intensity Profile Through the Focus

The theoretical model has been adapted to calculate the 2D spatial intensity profile at the resolution of the XUV CCD. Figure 3.6 shows, a-c) the experimentally observed spatial intensity profile at the two line foci and the CLC and d-f) the theoretical predictions corresponding to parameter values extracted from figure 3.5. In all cases, the pixels are 13 μm.

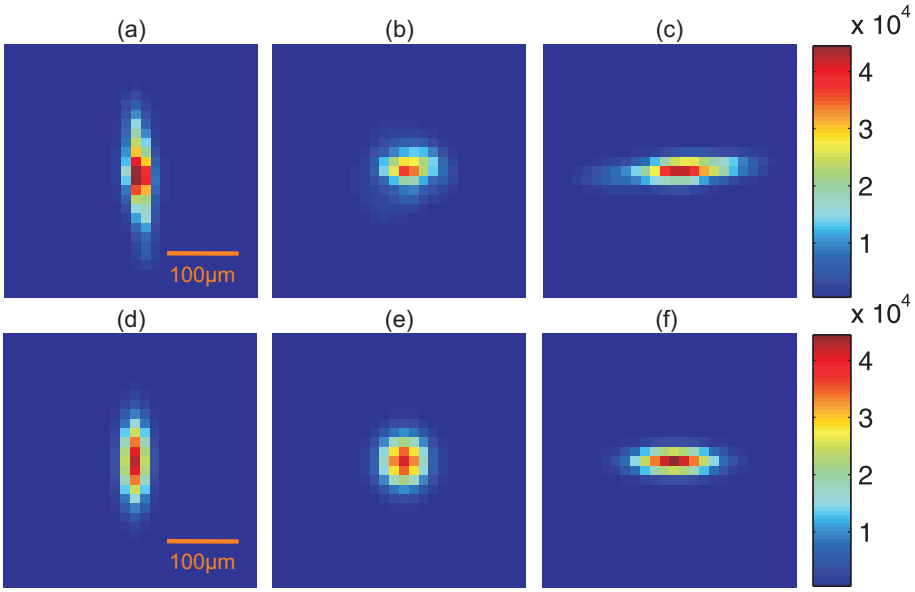

Figure 3.6: *Experimental a-c) and theoretical d-f) intensity profiles at the horizontal and vertical line foci, along with the intensity profile at the CLC, using the parameters determined from figure 3.5.*

The theoretically predicted profiles are not identical to the experimental results for two reasons. Firstly, the experimentally recorded intensity pro-

files are not centered over a single pixel. This can explain the difference in the relative intensities of the central pixels. The second reason is due to the limitation of describing a polychromatic complex spatial profile by using a single scalar quantity (the M^2 value). Whilst the width of the experimental beam as it propagates has been successfully modelled, the M^2 value does not contain information on the actual spatial profile. Instead the spatial intensity profile is modelled as a Gaussian which diverges faster than expected by a factor defined by the beam quality parameter.

Figure 3.7 shows the experimental (circles) and theoretical predictions (lines) for the peak intensity through the focus. The theoretical data, corresponding to a 9.55 degree mirror angle and the experimentally determined M^2 values, is shown as the solid line and normalised to the experimental data by making the most intense data points equivalent. The most intense data point for both experiment and theory is the horizontal line foci, and therefore if the peak intensity is to be maximised the sample should be positioned at the horizontal line focus, instead of the CLC. The fact that the second line focus is more intense than the first is an artifact of the different M^2 values for the x and y axes. For identical M^2 values, the first line focus is always the most intense position. Also shown is the effect on the peak intensity at the CLC if the mirror angle was reduced to 5 degrees (dashed line) and 0 degrees (dotted line), illustrating that the peak intensity at the focus would be almost doubled if the mirror angle was reduced from 9.55 to 5 degrees, whilst further decreases in the angle provide diminishing returns. In this case the errors are from the photon counting uncertainty (which is small as a high signal was recorded) and the error due to the resolution of the CCD. The vertical scale shows the photon count of the brightest pixel on the CCD image. As the intensity of the brightest pixel depends on whether the

XUV beam is central on a pixel, or central on a region between two pixels, the intensity of the brightest pixel will depend on the position of the beam on the CCD. As the beam is roughly five pixels in radius, the intensity will drop approximately 20% of the maximum across every neighbouring pixel. Depending on whether the signal is shared across two pixels or centred on a single pixel, the maximum intensity will vary up to around 10%. As this error can occur in both the horizontal and vertical axes of the CCD, the combined error is ± 14%. This is the error shown on the figure.

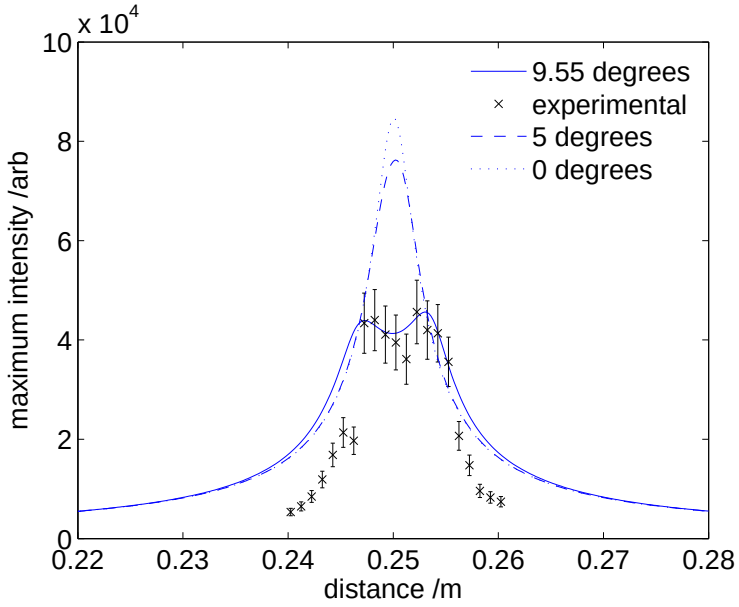

Figure 3.7: *Peak intensity through the focus for experimental data (circles) and the theoretical values (lines).*

Figure 3.7 indirectly shows that the spot size at the CLC will be reduced if the mirror angle is reduced, as the peak intensity is shown to increase. However, the spot size is a function of both the mirror angle and the mirror ROC. To increase the focussed intensity the mirror angle should be reduced and the mirror ROC decreased. However, as shown in figure 3.8, the relationship is nonlinear. For a mirror angle of 0 degrees, the spot size is

generally proportional to the mirror ROC. However, for a fixed mirror angle of 10 degrees, a shorter focal length mirror will only slightly decrease the spot size. Therefore, for mirror angles greater than 10 degrees, the most significant improvement in peak intensity will result from a decreased angle. Due to the nonlinear relationship, the combination of a longer mirror focal length and the possible corresponding smaller mirror angle can actually result in a tighter focus and a higher intensity. Therefore, a smaller ROC will not always increase the intensity at the beam focus.

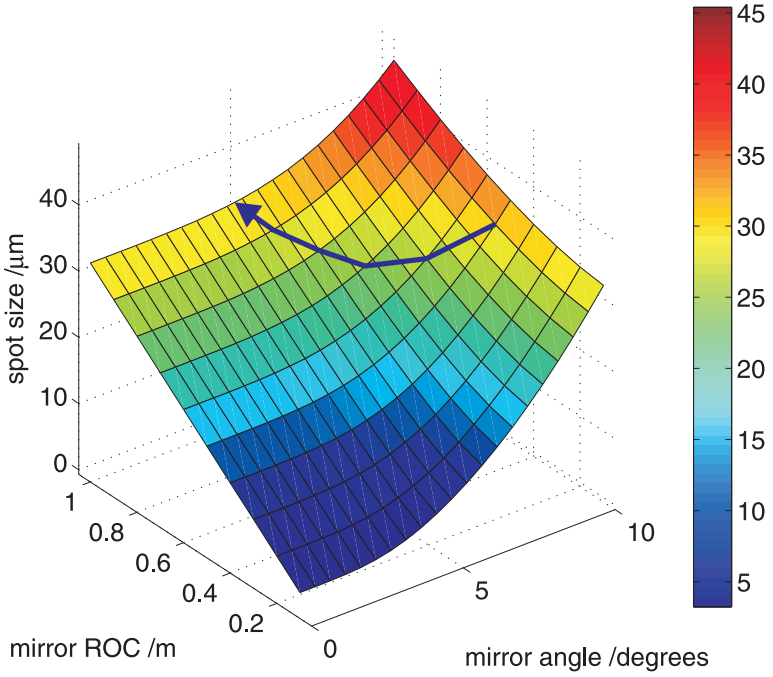

Figure 3.8: *Focussed spot size at the CLC as a function of mirror ROC and mirror angle, for the experimentally determined parameters. The arrow demonstrates the effect that increasing the mirror ROC will allow a smaller mirror angle, which will lead to a smaller spot size at the CLC. This is demonstrated by the colormap under the arrow, which changes from yellow, to green, then back to yellow. Here, the ideal mirror ROC is ∼0.7 m at an angle of 7 degrees. For a different camera width, the ideal value may be different.*

Astigmatic Phase through the focus

This section describes the phase of the XUV beam at positions through the focus. This is achieved using the ABCD matrix theoretical framework, as described in this chapter. In order to understand the effect of the off-axis mirror on the spatial phase distribution of the XUV beam through the focus, the phase of the beam before the mirror must be assumed to have a definable radius of curvature. This would be a reasonable approximation to make if the generated XUV beam was a Gaussian beam. However, previous calculations have shown that the M^2 value is significantly larger than unity. The XUV beam is therefore not a Gaussian beam, but is instead a superposition of high-order transverse electromagnetic propagation modes. As the ratios of the propagation modes cannot be determined from the scalar M^2 value, it is impossible to predict the phase of the beam incident on the mirror. The assumption used here is therefore not particularly strong but it is the best solution possible given the available data. Despite this problem, this section is still relevant to the discussion of off-axis focussing, as the phase distribution produced by the mirror is always symmetric and hence does not directly produce the asymmetric diffraction patterns that are experimentally observed.

The curvature imposed on the beam by the mirror is such that at the CLC, one axis is converging and one is diverging. Therefore the phase at this position is saddle-shaped. For the line foci, the phase is flat in one axis and curved in the other. Shown in figure 3.9 is the theoretically predicted phase through the focus, overlaid onto the theoretical intensity profiles which are thresholded at $1/e^2$ of the maximum intensity. In order to highlight the phase modulations, the figure shows $cos(\phi)$, where ϕ is the phase angle across the beam. For an angle of 9.55 degrees, a spherical mirror with

ROC of 500 mm will produce a significant phase variation across the beam. Although the phase variation is large for all positions through the focus, the variation is symmetrical and hence cannot produce the experimentally observed diffraction peak splitting, as the phase variation must have some asymmetry for this result. This principle is discussed further in section 3.1.4. Although the astigmatic phase will not produce split interference peaks, it will produce a different diffraction pattern to a similar intensity profile with a flat phase and hence is a consideration when using a spherical mirror in an off-axis arrangement for diffractive imaging.

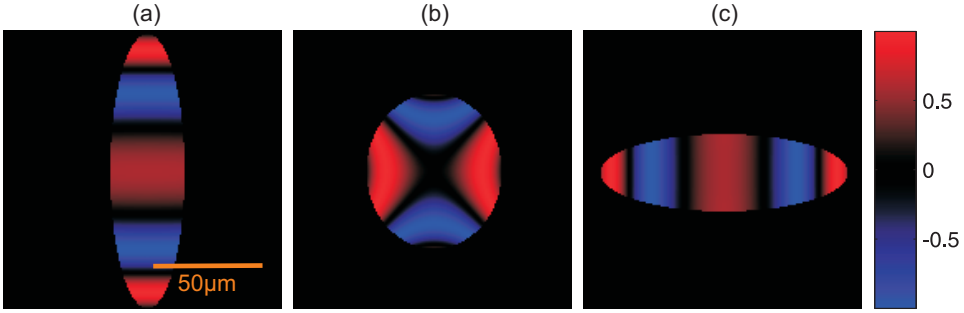

Figure 3.9: *Theoretical phase, displayed in the form cos(ϕ) in order to illustrate the phase modulations, mapped onto theoretical intensity profiles (as shown in figure 3.6), for the a) vertical focus, b) CLC and c) horizontal focus.*

3.1.4 Mirror Defect Modelling

In this section, the effect of large-scale surface modulations on the surface of the XUV mirror is investigated. The mirror surface simulation presented here can explain both the observed M^2 increase and the diffraction peak splitting that are experimentally observed. Although the mirror has an extremely low surface roughness, the surface figure (which corresponds to long-scale deviations from a perfect spherical profile) is defined as $< \lambda/10$ at 633 nm. This is equivalent to $\sim 2\lambda$ for a 30 nm wavelength. However, it is important to realise that both the surface figure value and the correlation

length of the deviations must be known in order to precisely quantify the effect of reflection from a mirror. In the results presented here, the latter is not known and hence the problem is instead approached differently. Given that we observe an increase of the beam M^2, and observe diffraction peak splitting, the work presented here attempts to quantify the mirror surface quality that would result in this observation. If the required mirror surface quality is within the manufacturers specification, then there is a strong possibility that the observed increase in M^2 and the observed diffraction peak splitting is a direct result of defects in the mirror surface. Future work will include optical interferometric results of the mirror surface, which will help to further quantify this model.

The deviation from a perfect spherical surface in nanometers, shown in figure 3.10a), is simulated by summing 1000 Gaussian distributions with radius 1 mm, and randomly positioned on the mirror. They have an equal chance of being positive or negative. The height of each Gaussian is randomly determined each time using the uniform distribution with range 0 to 4 nm. The central 2 mm part of the mirror, shown in figure 3.10b), represents the deviation for an area approximately equal to the incident XUV beam, and corresponds to the central region of the simulated mirror surface. In this case, the simulated root mean square value for the whole mirror is 8 nm, which is less than the quoted value of 63 nm.

By assuming that the incident XUV beam has a perfect Gaussian intensity profile and a flat phase, the perturbation to the phase can be calculated by taking into account the varying pathlength for each part of the beam. This result is Fourier transformed to give the intensity and phase of the XUV beam at the mirror focus. The effect of the astigmatic focus is ignored in order to understand the different effect of the two aberrations. Figure

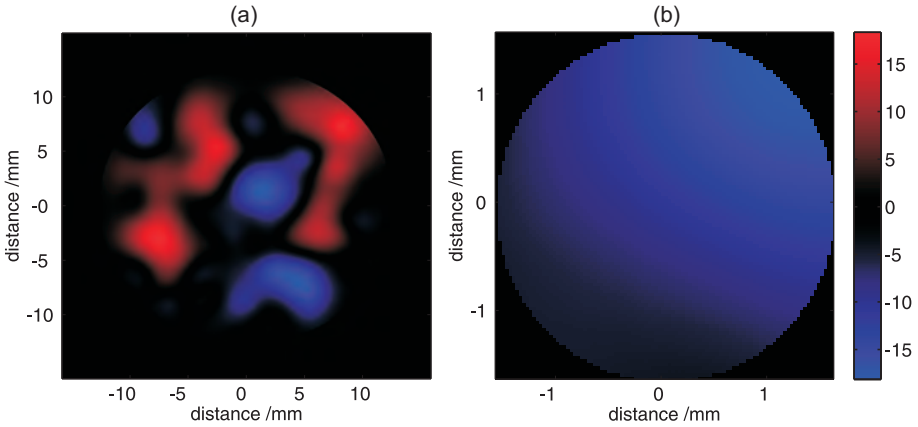

Figure 3.10: *Simulated deviation from a perfect spherical profile constructed by the combination of 1000 Gaussians with radius of 1 mm and random heights up to 4 nm, for the a) entire mirror surface, and b) region illuminated by the XUV beam.*

3.11 shows a) the simulated intensity profile, b) the effect of re-sampling the intensity profile at a resolution corresponding to the CCD and c) the phase profile at the focus. The intensity profile in a) is surprisingly asymmetric, and is a direct result of the phase shift produced, corresponding to the surface in figure 3.10b). However, when figure 3.11a) is sampled at a resolution equivalent to the CCD, as shown in b), the intensity profile appears to be considerably more symmetric. This shows a qualitative agreement with the experimentally observed intensity profile in figure 3.6b), confirming that this model does not contradict experimental observations of the apparent symmetry of the XUV spatial intensity profile at the focus. This therefore implies that the spatial intensity profile may be significantly worse than is implied by the experimental data, due to the low resolution of the sampling.

The phase, shown in figure 3.11c) also exhibits asymmetry, as opposed to the astigmatic phase which possesses rotational symmetry. Part c) shows the value of the phase for all pixels that correspond to greater than 1% of the simulated maximum intensity in order to clearly demonstrate this asymme-

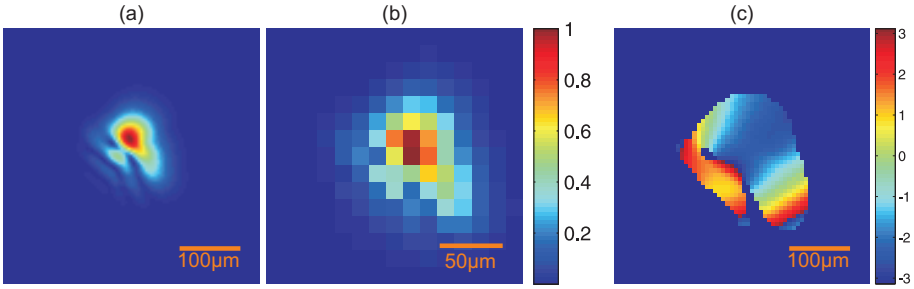

Figure 3.11: *The simulated a) intensity and c) phase profiles at the focus, given the mirror surface in figure 3.10b) showing the predicted asymmetry in the beam profile at the focus. Part b) illustrates the effect of re-sampling the intensity profile onto pixel sizes that are equivalent to the XUV CCD, demonstrating that a non-circular beam profile can appear approximately circular when the sampling resolution is reduced.*

try. Simulations show that the effect of using the astigmatic intensity and phase for diffraction experiments results in little change when compared to a beam with a flat phase. However, as discussed in more detail later in this section, the asymmetric phase that results from a modulated mirror surface considerably affects the diffraction images, and can successfully explain the experimentally observed interference peak splitting.

The M^2 that corresponds to the intensity and phase in figure 3.11 has been calculated using software written by group member Rogers, which uses the angular spectrum method [85]. This technique enables the electric field an arbitrary distance from an initial known electric field to be determined. The technique is discussed in more detail in section 4.1.4 where it is used to calculate Fresnel diffraction patterns. Given an arbitrary beam profile, the new beam profile corresponding to any propagation distance can therefore be directly calculated. By calculating the profile at ten positions, the beam M^2 for both the horizontal and vertical axes has been determined. For the simulated beam in figure 3.11, the values 2.2 and 2.5 were calculated. The simulated surface in figure 3.10b) has therefore increased the beam M^2 by a factor of $\sim$2.5, clearly showing that a modulated mirror that deviates from

a spherical profile by less than 20 nm over a 1-inch optic can significantly deteriorate a 30 nm XUV beam. This effect is observed experimentally. As shown in section 3.1.3, the XUV beam quality was observed to be degraded by a factor of 5. In addition, the simulated beam quality in the horizontal and vertical axes is different, an effect also observed experimentally.

Although the degraded intensity profile is an important consideration, the phase profile at the focus is of paramount importance due to the effect on subsequent diffractive imaging. By moving the CCD from the focus (see figure 3.3) and replacing it with a periodic sample, the effect of the degraded phase can be illustrated. The sample, a single-layer hexagonal array of 196 nm diameter polystyrene spheres supported on a 50 nm thick silicon nitride substrate, is discussed extensively in chapter 5. This sample has also been simulated by creating a hexagonal array of circles. The theoretical far-field diffraction pattern is therefore the Fourier transform of the product of the simulated sample and the simulated beam profile from figure 3.11. Figure 3.12a) shows the simulated diffraction pattern using the degraded intensity with a flat phase. The hexagonal structure, which results from the hexagonal lattice on the sample, is clearly shown. Although there is some elongation of the interference peaks, no significant splitting is observed. Figure 3.12b) shows the simulated diffraction pattern for both the degraded intensity and the degraded phase. The interference peaks show significant splitting and hence clearly demonstrates the effect of an asymmetric phase on a diffraction pattern.

Figure 3.13 shows the experimentally observed result. Before a comparison is made, there are two important considerations. Firstly, the theoretical diffraction peaks are larger simply as a result of using a spot size that illuminates fewer spheres. This is a consequence of needing at least 20 pixels to

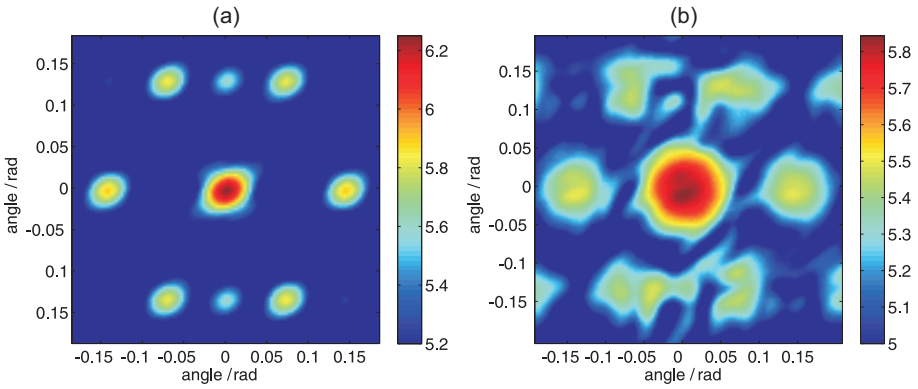

Figure 3.12: *Simulated diffraction pattern from a hexagonal array of circles when using a) the simulated intensity and a flat phase, and b) both the simulated intensity and phase from figure 3.11.*

simulate a single sphere and being limited by computer memory to using a 4000 by 4000 array of double precision numbers. Secondly, the experimental result consists of multiple wavelengths, and hence the diffraction peaks are repeated for different angles.

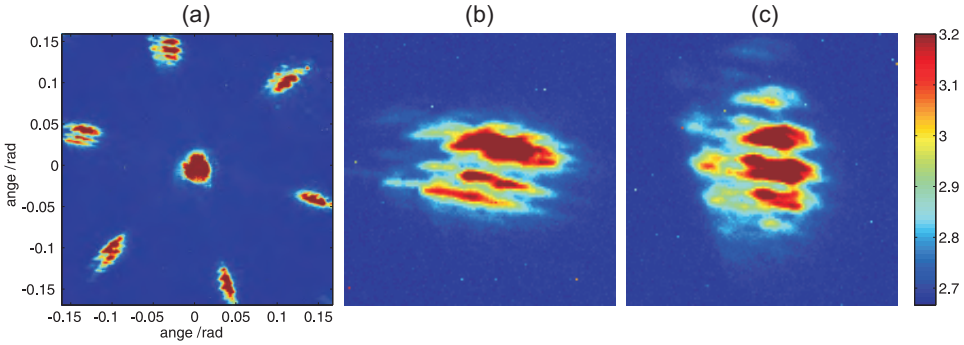

Figure 3.13: *Experimentally observed diffraction pattern from a single layer hexagonal array of 196 nm diameter polystyrene spheres, showing the a) whole diffraction image, b) left interference peak and c) top interference peak. This figure is identical to figure 3.2.*

Figure 3.13a) shows the experimental equivalent to the results in figure 3.12, while parts b) and c) show two of the experimental diffraction peaks in more detail. Although the interference peaks correspond to multiple wavelengths in the axial direction, there is significant splitting in the radial

direction. The splitting is unique for each of the interference peaks, and therefore good qualitative agreement is demonstrated with the theoretical results in figure 3.12. This analysis shows that an asymmetric phase at the XUV focus can be used to explain the experimentally observed interference peak splitting. However, as it is not possible that the phase distortion resulting from the astigmatic focus can produce this effect, there must be another factor introducing additional phase distortions. This section has shown that this effect can be explained by the presence of nanometer sized modulations over large distances in the mirror surface, and therefore that the mirror surface figure is an extremely important consideration for XUV optics when diffractive imaging is investigated.

Aluminium Filter Simulation

In previous sections, analysis of experimental results has shown that the M^2 of the XUV beam has been increased from ∼3 to ∼15. Simulations have demonstrated that this effect can be explained by nanometer sized defects on the mirror surface. In these simulations, the effect of the 200 nm thick aluminium foil (see figure 3.3) on the XUV beam quality was not included. Whilst it is true that there are deviations in the thickness of the aluminium foil and this will affect the XUV beam quality, this section demonstrates that the effect is negligible.

The thickness tolerance of the aluminium foil is ± 10 nm. However, the typical maximum surface deviation is 1% per cm [86]. The simulation of the aluminium foil thickness can therefore be treated similarly to the mirror surface simulation. The simulated thickness of the aluminium foil used in the presented result is shown in figure 3.14, where a 200 nm thick aluminium foil with a 5 nm layer of aluminium oxide on either side is demonstrated.

The refractive index data for both materials are taken from [65].

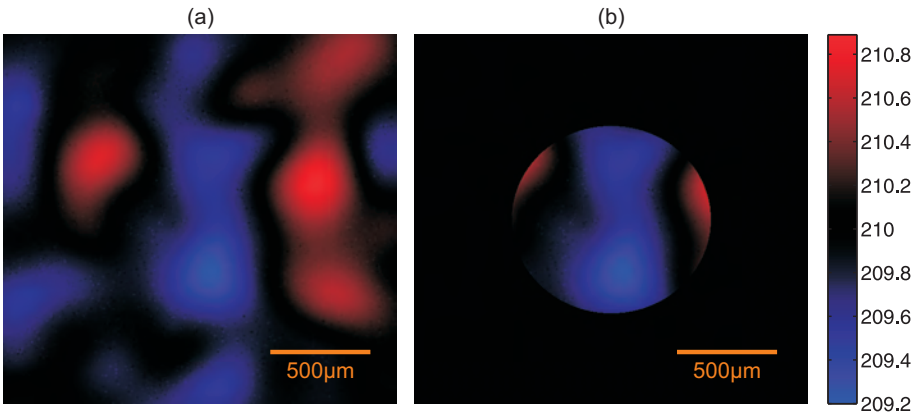

Figure 3.14: *Simulation of the aluminium foil thickness in nanometers, showing a) a 2 mm square region and b) the region corresponding to a 1 mm diameter XUV beam.*

To simulate the effect on the XUV beam quality, the intensity and phase profile immediately after the aluminium foil is calculated [87]. The input beam has a Gaussian intensity profile and a flat phase. The result is shown in figure 3.15. The previously described Angular Spectrum Method is then used to calculate the increase in the XUV beam M^2 as a direct result of propagation through the foil. The results for the surface shown in figure 3.14 are an increase in M^2 in the horizontal and vertical profile of 0.25% and 0.14% respectively. For the chosen simulation parameters, the increase was less than 1% for a series of ten outcomes. Whilst this result clearly shows that the effect on the XUV beam quality is negligible, the simulated value relies on the accuracy of the refractive index data from [65] which is known to have large errors in the XUV spectral region. However, simulations repeated using refractive index data for other metals has shown that the randomness in the simulation of the thickness of the metal foil produces a larger variety of outcomes than a change in the metal. This is due to the small variation in the real part of the refractive index for materials in the XUV region.

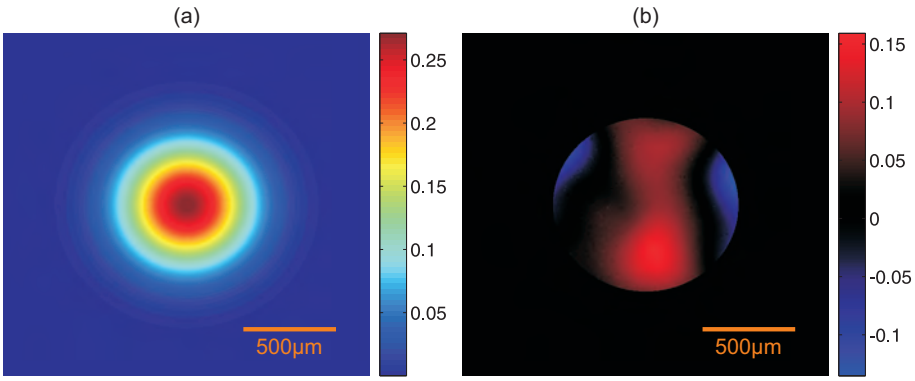

Figure 3.15: *Simulated a) intensity and b) phase shift of a 30 nm XUV beam after propagation through the simulated foil.*

3.1.5 Conclusion

Presented in this section is an extensive analysis of an astigmatic XUV beam, produced when a spherical mirror is used in an off-axis arrangement to focus capillary-generated XUV. By using an experimentally verified 3D model, the balance between the experimental parameters required for an optimal focus has been determined. As the focussed spot size is a nonlinear function of the mirror angle and mirror ROC, increasing the ROC (if it allows a smaller mirror angle) can actually decrease the spot size and hence increase the peak intensity. However, in order to minimise the phase distortion and maximise the focussed intensity, the mirror angle should be less than 5 degrees. The theoretical model has also enabled a calculation of the XUV beam M^2, at 14.0 ± 1 and 16.6 ± 1 for the horizontal and vertical axes, and has shown that the beam M^2 has been increased upon reflection from the XUV mirror.

The cause of the increase in the beam M^2 is proposed to be the non-zero surface figure parameter for the XUV mirror. This effect has been indirectly investigated by calculating the phase perturbation imparted on an XUV beam upon reflection from a mirror that deviates from a perfect spherical profile. Using this phase perturbation, the theoretical intensity

and phase at the XUV focus was calculated and was shown to be degraded in a way that has been observed experimentally. Most importantly however, the simulated beam profile was shown to have a significant effect on the diffraction pattern from a periodic structure. Instead of distinct interference peaks, the interference peaks were found to show significant splitting. This effect is observed experimentally and therefore shows that the surface figure of an XUV optic is of critical importance when both focussing and using the focussed source for diffraction imaging.

3.2 Hollow Focussing Fiber

In order to obtain a high XUV irradiance for diffraction experiments, a focussing device can be used. In this section, experimental results for a hollow focussing fiber with a parabolic profile are presented. This device reflects light through the phenomenon of total external reflection. Incident XUV radiation that is well collimated will be reflected to a single focus. However, the quality of the focus is very dependent on both the quality of the parabolic profile and the alignment of the optic. In this section, these two effects are quantified, with the aim of understanding the observed focus and calculating how to improve it.

This section is outlined as follows. In section 3.2.1, the methods for fabrication of the fiber are discussed. The fabrication itself was carried out by the company Chiral Photonics, whilst the cleaving and further characterisation was completed at the University of Southampton. The measured profile is shown, and compared to the ideal parabolic profile. Section 3.2.2 shows the experimental configuration, along with alignment techniques. In section 3.2.3 experimental results for the optical transmission and focussed spot size are given. In section 3.2.4, a 'knife-edge' technique is demonstrated, which

has enabled the dynamic range on the CCD to be increased from three orders of magnitude to seven. This has enabled a detailed measurement of the spatial profile of the XUV beam in the far field, after propagating through the focus. Significant structure is observed at wide angles. In section 3.2.5 the results from a beam propagation simulation, written by group member Froud, is presented. The model shows that the the structure observed at wide angles corresponds to rays of light that has reflected multiple times inside the fiber. Finally, as shown in section 3.2.6, by measuring the spatial intensity profile of the XUV beam at increasing distances from the focus, the M^2 of the beam is calculated to be 5.4 for the central spot, and 18.3 if the wide angle structure is taken into account.

Most of the experimental setup, and some of the experiments for the hollow fiber was carried out with the assistance of the post-doctorate group member de Paula. The analysis of the experimental results is my own. The ray tracing model, developed to understand and optimise the fiber was developed by group member Froud. Figure 3.22 is adapted from [67] and figure 3.24 is adapted from [88].

3.2.1 Fabrication

A hollow glass fiber with a specific profile can be fabricated by pulling both ends of a section of cylindrical hollow fiber whilst heating the central section, as shown in figure 3.16. Both the length of the heated region and the speed of the translation stages can be varied to allow almost any profile to be developed [89]. The focussing fiber used in this chapter was fabricated by the company Chiral Photonics. The measured inner diameter is shown in figure 3.17.

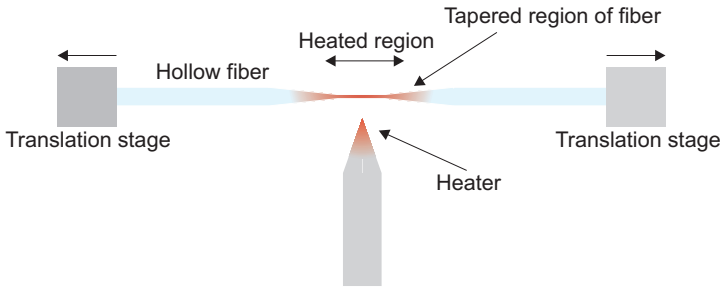

Figure 3.16: *Schematic showing the fabrication technique for a hollow focussing fiber.*

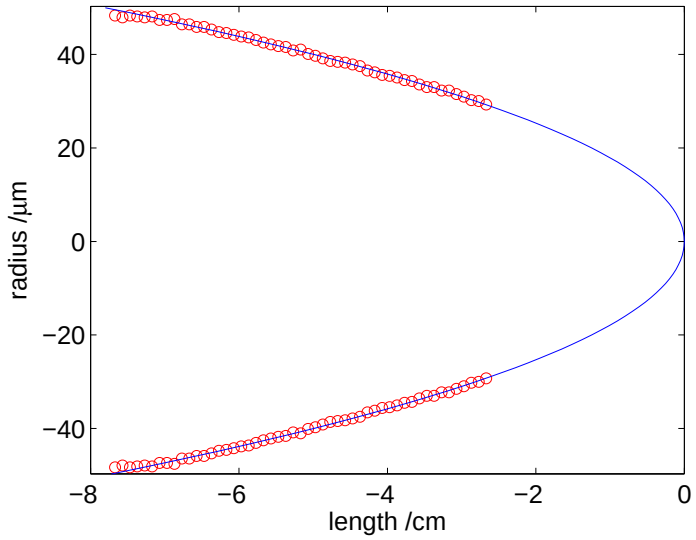

Figure 3.17: *Measured inner diameter of the hollow fiber (red circles) plotted against a parabola (blue line). The measured inner diameter varies from 96 µm to 58 µm over a 5 cm length. Note the unequal scales on the two axes.*

3.2.2 Experimental Configuration

The introduction of a focussing fiber into a diffraction setup requires a different strategy to the previously discussed multilayer mirror. In this section, the requirements of the experimental configuration are presented along with the final setup.

The inner diameter of the focussing fiber entrance is 96 μm. However, the diameter of the XUV beam at this position is $\sim$1 mm. Therefore a maximum of $\sim$4% of the generated XUV can be focussed by the fiber. This limitation is a consequence of both the required parabolic profile (a small increase in the entrance would require a large increase in the fiber length) and of the available standard vacuum equipment. As shown in figure 2.11, both a mirror and a metal foil must be positioned between the generation optic and the focussing fiber. This results in a distance greater than 50 cm. If custom vacuum equipment were to be used, this distance could be decreased and the percentage of XUV focussed by the fiber could be increased. The XUV that does not propagate through the fiber should be blocked as it could interfere with the diffraction pattern from a sample.

The experimental requirements for the hollow fiber focussing apparatus are as follows:

1. For diagnostics, the entire XUV beam must be observable, and hence the hollow fiber must be able to be moved fully out of the beam. This allows the fiber to be positioned at the most intense part of the beam. This requires two long distance actuators, for the horizontal and vertical axes.

2. Once positioned, the fiber must be aligned with respect to the XUV beam, requiring a vertical and horizontal pivot movement.

3. As the XUV beam is significantly larger than entrance aperture of the fiber, light which does not pass through the fiber must be apertured. However, the aperture must be variable-sized to allow the full beam to be observed for step 1. Therefore an externally controlled iris is required. As the iris is always positioned in line with the fiber, it can use the actuators described in step 1.

For convenient mounting and handling, the focussing fiber was held inside a hollow cylindrical capillary. In addition to the required actuators for the alignment of the focussing fiber, there are also three axes of movement on the sample, and two axes for the camera. This setup is shown in figure 3.18. This gives a total of seven actuators, and two fine adjustments for alignment, along with an externally controlled iris.

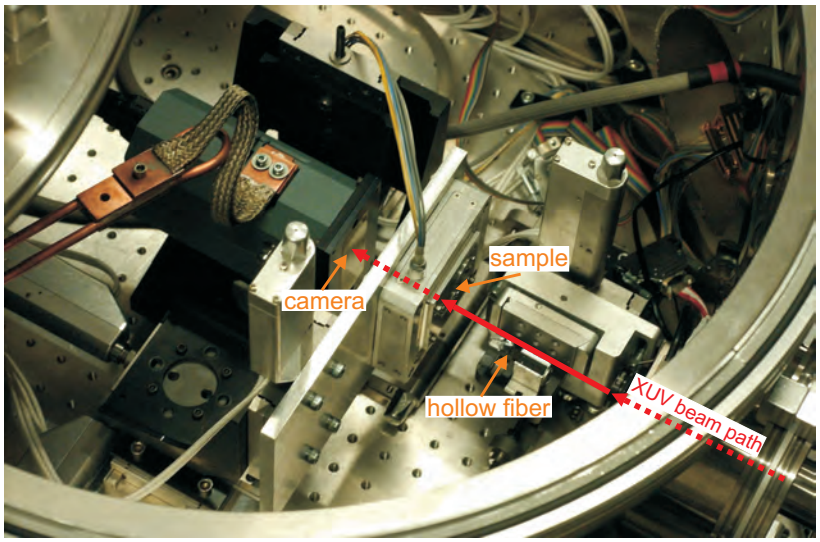

Figure 3.18: *Photograph of hollow fiber focussing experimental setup, showing locations of the hollow fiber, sample, sample stage, and XUV camera.*

For alignment, fine angle adjustments on the order of 100 nanoradians were used with the aim of both maximising the throughput and optimising the shape of the transmitted beam. Typically, low throughput was found to

correspond to significant intensity in concentric wide-angle ring-like structures. This concept is discussed further in section 3.2.4, where it is shown that the rings correspond to multiple reflections inside the hollow fiber.

3.2.3 Transmission and Spot Size

In order to determine the effectiveness of the fiber as a focussing device, the XUV spot size, transmission, and intensification must be measured. The spot size (w_0) has been measured to be 17.3 μm and 16.7 μm in the horizontal and vertical axes respectively. This measurement was taken at a position immediately after the exit aperture of the fiber. The transmission and increase in irradiance are harder to measure accurately. The two CCD images shown in figure 3.19 elucidate the technique used.

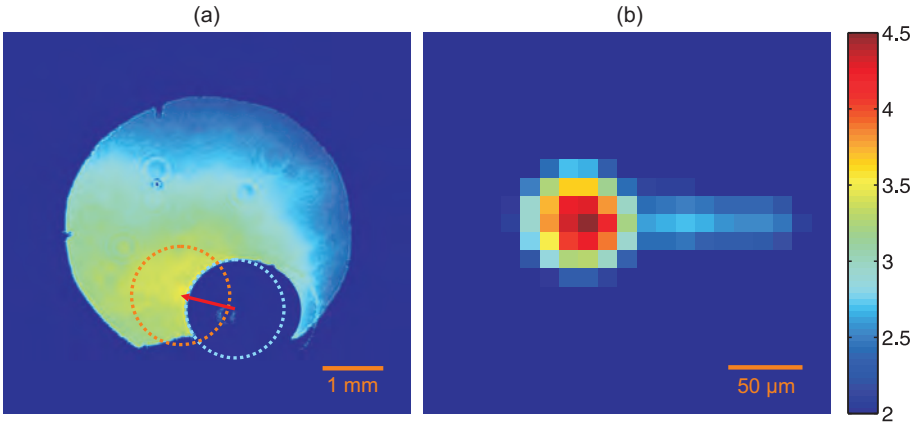

Figure 3.19: *The technique used for calculation of the fiber transmission and the increase in irradiance. Part a) shows the XUV spatial profile with the fiber mount (shown by the blue circle) moved out of the most intense part (shown by the red circle). Part b) shows the transmitted XUV when the fiber is moved to the most intense part of the beam. The color scale is logarithmic.*

In both images the CCD is positioned approximately 1 cm after the fiber. In part a) the following components are positioned in increasing distance from the CCD: the mount containing the fiber as shown by the blue circle, the externally controlled iris which is currently fully open, and the XUV

radiation source. The red arrow points to the most intense spatial region of the XUV source and hence the mount containing the focussing fiber was moved to that position, as shown by the orange circle. With the fiber in position, the externally controlled iris was closed. The light now incident on the CCD corresponds only to XUV that has passed through the focussing fiber. This result is shown in part b). Note the different distance scale on the image. Both images have been normalised for time, and therefore the increase in irradiance resulting from the fiber is apparent from the figure. It is important to realise that the fluctuations in the shape and intensity of the XUV beam make an accurate measurement of the transmission and increase in intensity difficult as the most intense part of the beam may not correspond to the entrance of the fiber. However, by assuming the fiber entrance is positioned at an intensity that is between 90% and 100% of the maximum intensity, a transmission of between 32% and 39.5% and an increase in irradiance of between 10.6 and 13.1 is determined. Interestingly, some throughput of the fiber is observed in part a). At the base of the red arrow a weak ring-like structure is observed. As shown in the following section, this ring structure corresponds to multiple reflections inside the fiber.

3.2.4 Ring Structure

The XUV spatial profile in the far field, after propagation through the hollow fiber, consists of two parts; a central spot corresponding to XUV that has passed through the hollow fiber without reflecting off the sides, and a wide-angle ring-like structure corresponding to one or more reflections inside the fiber. To study this structure, the CCD was positioned such that the intense part of the beam missed the chip whilst the less-intense ring structure

was observed using a longer integration period. Figure 3.20 shows several concatenated images, which have been recorded in this way and normalised to the same integration time. Seven rather than three orders of magnitude of intensity can now be observed.

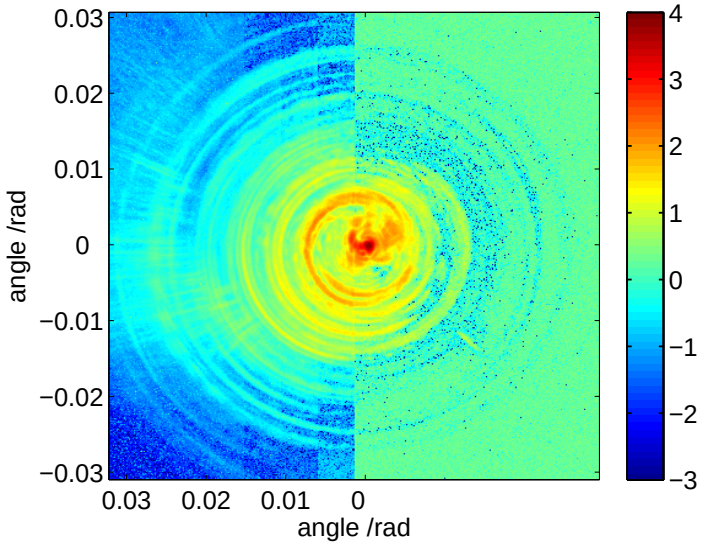

Figure 3.20: *Concatenated intensity profiles recorded for integration times of (a) 500 s, (b) 200 s, (c) 100 s, (d) 50 s and (e) 6 s allowing the less-intense structure to be studied. The images have been normalised to the same integration time and put on a logarithmic scale.*

Figure 3.20 shows five or six main rings, with some rings consisting of additional structure. If a sample is placed after the fiber and the diffraction pattern is recorded, a great deal of the scattered light will be hidden amongst the observed ring structure. Figure 3.21 shows a selection of figure 3.20 along with an intensity profile, highlighting the angular profile of the rings produced as the XUV leaves the hollow fiber. Also shown on figure 3.21 is the required periodicity of a sample that would result in 30 nm radiation being diffracted to the same angle as the ring structure. Information corresponding to distances greater than 1 μm may therefore be difficult to resolve. However, smaller length scales should not be greatly affected.

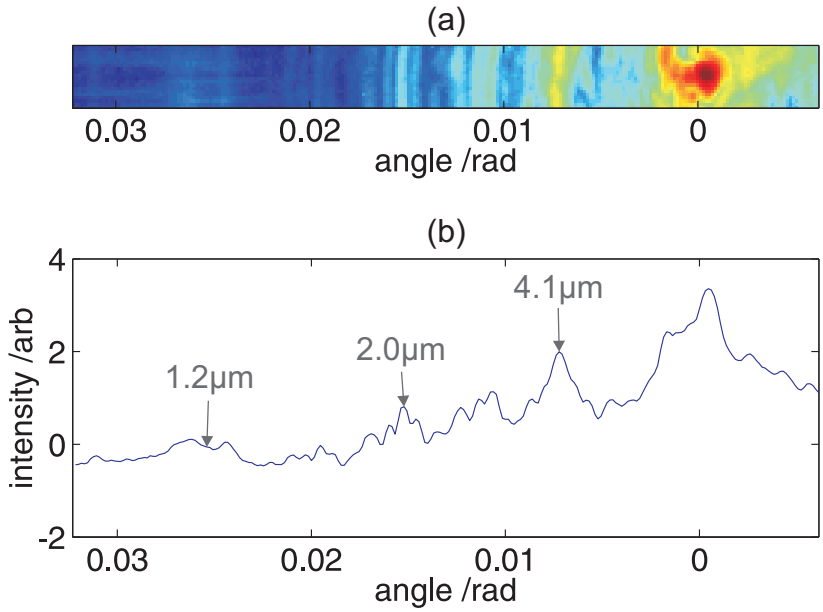

Figure 3.21: *(a) Thin section of ring profile from figure 3.20 and (b) corresponding angular profile of the ring structure. Also shown are periodic spacings that would cause interference peaks for 30 nm radiation at the ring angles. The color scale is logarithmic.*

3.2.5 Theoretical Model

To help understand the processes inside the focussing fiber and to interpret the experimental results, a propagation model has been created by group member Froud [67]. To precisely simulate the propagation of light through a simple structure, such as a one dimensional waveguide, an analytical wave model can be used [90]. However, in order to model propagation through a three dimensional optic, a ray-tracing approach is generally used. This approach is appropriate when the wavelength of the light is small in comparison to the size scale of the simulated optic [91], and therefore ray tracing is an appropriate technique to simulate the focussing fiber described in this chapter. The simulation by Froud builds on the model described by Vincze [88] by introducing both a Gaussian radiation source (rather than a point source) and interference effects. The simulation concept and results are presented

in this section.

In order to simulate the output of the fiber, the following calculation steps are completed. The three dimensional fiber surface is constructed with a user-defined profile, and bends and twists in the profile can be added. The initial distribution of rays is then determined. By choosing an appropriate distribution of position and trajectory angles a Gaussian beam source can be simulated [92]. All rays that do not pass through the entrance of the optic are removed, and all rays which pass through the optic with no reflections are temporarily ignored. The following is then determined for each remaining ray: the intersection point of the fiber surface and the ray, the surface normal and hence the reflected angle of the ray, all subsequent intersection points and reflected angles, and the angle and position of the ray as it leaves the optic. For each reflection, the Fresnel reflectivity is calculated, and the intensity of the ray is updated. Although all rays will eventually leave the optic, it was found that the simulation speed was considerably faster if all rays that reach a tenth reflection were removed. The position and angle of the rays that pass through the exit of the optic are then propagated to a plane that is normal to the propagation of the rays, corresponding to a virtual CCD. The virtual CCD is a two dimensional histogram, corresponding to individual pixels. The coherent sum of all rays that are incident on each pixel is then calculated.

Figure 3.22 shows a) a schematic of this described simulation, and b) a simulated radial distribution of the XUV after propagation through the focussing fiber using similar parameters to the experimental setup described in this chapter. Part b) shows strong qualitative agreement with the experimental results shown in figure 3.20. Analysis of part a) shows that the rays that form the ring structure always correspond to one or more reflections

inside the fiber, whilst the rays in the central spot always correspond to paths with no reflections. To clarify this explanation, the rays that experience one or more reflections are coloured red and the rays that experience no reflections are coloured blue. The fact that the central spot was found to generally propagate in a slightly different direction to the centre of the ring structure (see figure 3.20) provides further evidence that the central spot is only light that has experienced no reflections.

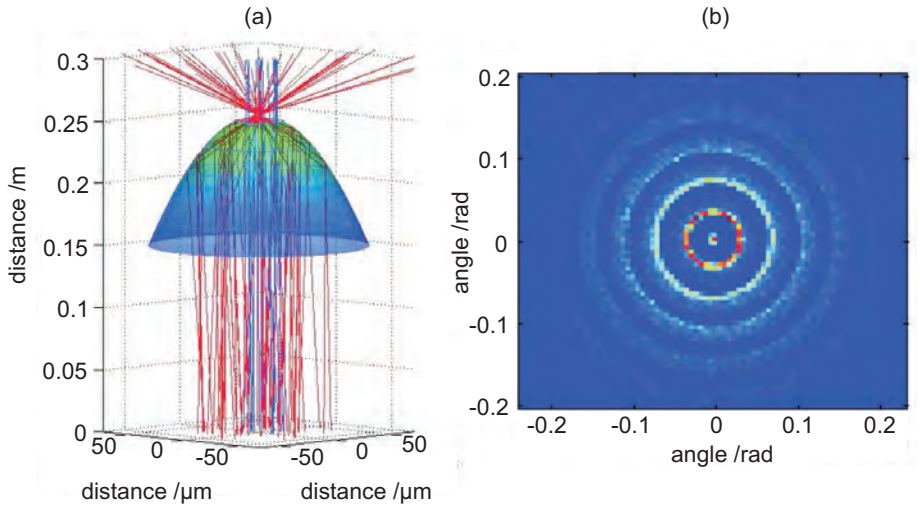

Figure 3.22: *(adapted from [67]) Part a) presents a schematic of the simulation showing paths of XUV photons as the propagate through the fiber. Blue rays correspond to zero reflections and produce the central spot. Red rays correspond to one or more reflections inside the fiber and produce the ring structure. Note the unequal distance scales. Part b) shows the simulated far-field image of propagated XUV from the fiber, and shows good agreement with figure 3.20.*

During the procedure of aligning the fiber to the generated XUV, a large variation of ring structures, some of which possessed little symmetry, were often observed. Figure 3.23 presents four different images recorded on the experimental system presented in this chapter. The images are not fully understood, but they are known to correspond to varying degrees of misalignment. Even for a small tilt angle, the output can change considerably as the XUV may no longer be able to pass through the fiber with no reflec-

tions. The greater the tilt angle, the more reflections are required for light to pass through the fiber, and this can result in a larger overall deflected angle. These experimental results are similar to experimental results presented in [88] corresponding to 8.9 keV radiation at the European Synchrotron Radiation Facility. Theoretical results in this publication show that the tilt angle produces symmetrical rings, and that twists and bends in the fiber will produce asymmetric rings. Due to the relatively strong symmetry in figure 3.20, the fiber used in this chapter can be assumed to be free of bends and other such defects. However, the fact that the ring structure is always present implies that the parabolic profile of the fiber is an incorrect profile for the experimental setup. This is a consequence of the distances between the source and the fiber. As the rays are not collimated by the time they have reached the entrance of the fiber, they are not focussed to a single point. The correct profile for the fiber in the current experimental setup is therefore an ellipse.

3.2.6 Beam Propagation

By measuring the spatial beam profile at distances separated by 2 mm, the XUV beam quality as a result of the hollow fiber has been calculated. This is shown in figure 3.25, where both the quality of the central spot and the entire beam is shown. The central spot measurement is calculated by simply masking the outer ring structure. The error bars in this figure are a result of the deviations in the size of the XUV beam, for a fixed distance through the focus. This has been previously calculated to be approximately 10%. As discussed earlier, the deviations in size result from small changes in the laser intensity at the point of XUV generation; a higher intensity will ionise a larger volume of gas atoms, producing a larger source size and hence a

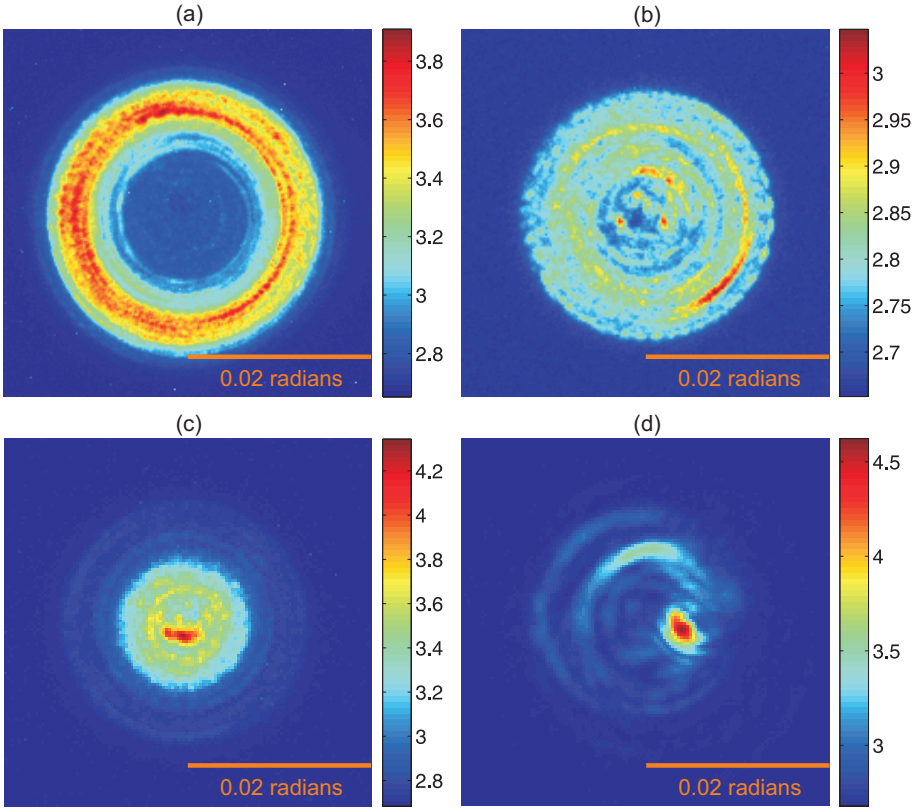

Figure 3.23: *Experimental XUV far field images for the focussing fiber, for varying tilt angles, displayed on a logarithmic color scale.*

Figure 3.24: *(adapted from [67]) Experimental results for 10 cm long focussing fiber recorded for different tilt angles at the European Synchrotron Radiation Facility. No scales or intensity colormaps are presented in the paper.*

larger focus.

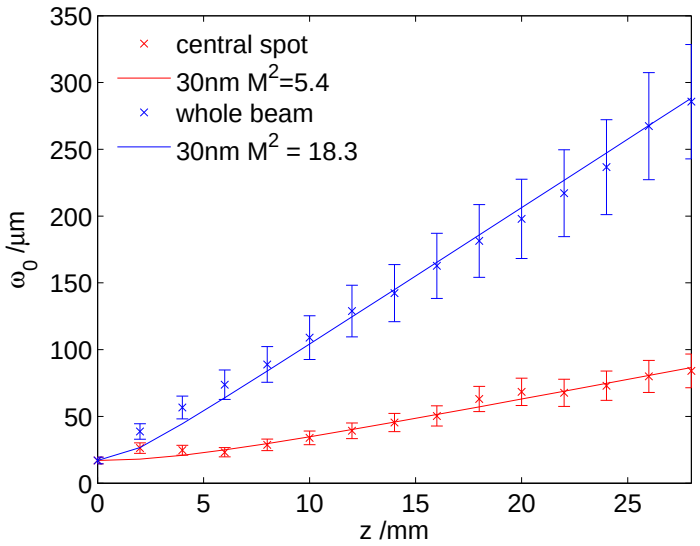

Figure 3.25: *The measured beam size for the central spot and the entire beam as a function of distance away from the hollow fiber exit.*

Figure 3.25 shows experimental data plotted against the propagation of a 30 nm Gaussian XUV beam. However, unlike the results reported earlier in this chapter from mirror focussing, the beam after the fiber has a large bandwidth. As the divergence of a beam depends on its wavelength, the M^2 fit to the experimental data must also be changed and hence the values quoted in the figure have an associated error. By fitting the data using wavelengths between 25 and 35 nm, a good approximation to the harmonic spectrum, the M^2 values of 4.6-6.4 and 15.7-21.9 have been determined.

3.2.7 Conclusion

From the evidence gathered in this section, it can be concluded that there are two components to the XUV after propagation through the fiber; a central spot corresponding to XUV that has passed through the fiber without any reflections, and a ring structure corresponding to one or more reflections

inside the fiber. The smallest spot size was measured to be immediately after the fiber exit aperture, and corresponded to 17.3 μm and 16.7 μm in the horizontal and vertical axes respectively. A transmission of $\sim$35% and an increase in the irradiance of $\sim$12 was also determined. The main drawback of using the fiber for diffraction experiments is the resultant ring structure. The angle of the ring structures was shown to coincide with diffracted light from a periodicity of a micron or greater.

3.3 Focussing Summary

As shown in this chapter, both the size and the quality of the focus must be considered. In the case of the focussing fiber, the rings caused by multiple reflections is a significant drawback as the XUV diffracted from a sample would be masked by the ring structure. The multilayer mirror however also displayed abberations at the focus due to both the astigmatism and the nanoscale surface modulations. This resulted in a diffraction pattern that exhibited asymmetric interference peak splitting. The phase at the focus of fiber was not measured, but due to the multiple reflections, a flat phase is unlikely.

The optics must also be compared with experimental integration in mind. The hollow fiber required extensive alignment each time it was to be used and, due to the nature of the focus, the fiber exit had to be positioned immediately in front of the sample. This posed problems with damage to the fiber and sample, and added another layer of complexity to the experimental setup. The multilayer mirror has the advantages of requiring only two axes of alignment.

The understanding of the propagation of the XUV inside and after the hollow fiber will enable a second generation of focussing fibers to be fab-

ricated with specific experimental parameters in mind. The possibility of designing a parabolic-shaped generation capillary that is used for both XUV generation and focussing is an intriguing possibility and could lead to a very compact radiation source.

Chapter 4

XUV Diffraction

X-ray diffraction can be used to determine the structural properties of periodic objects. Their diffraction patterns will in general consist of a series of discrete interference peaks. The angular separation and intensity of the peaks can be used to determine the structure of the object and the properties of the individual unit cells.

For diffraction patterns corresponding to a thin sample and obtained at a large object to detector distance, the electric field at this position is the Fourier transform of the electric field immediately after the object. However, a detector will record the modulus squared of the field, and hence information on the phase of the field is lost. Therefore, an inverse Fourier transform cannot be used to determine the overall shape of the object from the diffraction image.

If the detector is replaced by an objective lens, an electric field distribution that is identical to the one immediately after the object will then be projected to an imaging plane. A detector positioned at this plane will record an intensity distribution that is identical to that immediately after the original object. The lens therefore performs an inverse Fourier transform.

In this chapter, a technique that enables an object to be 'imaged' using only the diffraction pattern that is recorded on a detector is presented. In this case, the objective lens is replaced with an algorithm that firstly determines the phase of the diffraction pattern, then performs the inverse Fourier transform. The resolution limit for this imaging technique is therefore limited by the ability of the algorithm to find a solution, rather than abberations in the lens. To determine the phase, the object must be smaller than the inverse Fourier transform of the diffraction pattern recorded on a detector. The diffraction pattern must therefore be sampled at a high enough resolution.

Although this technique, known as coherent diffractive imaging (CDI), has been known for over thirty years, in the last decade there has been significant progress in the field. In this chapter, the technique is described and experimental results showing the imaging of a micron-sized object at extreme ultraviolet (XUV) wavelengths is presented.

In section 4.1 a brief motivation for diffraction as a tool for sample characterisation is given. An introduction to diffraction theory is then given, covering coherence and Fresnel and Fraunhofer diffraction. A technique that can be used to simulate the diffraction pattern for an arbitrary object to detector distance, the angular spectrum method (ASM), is also presented.

In section 4.2 the ASM is used to verify experimental Fresnel diffraction results from an object with a 4 μm periodicity. The simulations show good agreement with experimental results from both capillary and gas cell generated XUV high harmonic generation (HHG) radiation sources.

In section 4.3, the technique of CDI is introduced. The main result of this chapter is shown in section 4.4 where the phase of an experimental scattering image is calculated. This enables the original sample to be determined. The result is compared to an image of the sample taken with a optical microscope.

A conclusion to the chapter is given in section 4.5.

4.1 Diffraction Theory

In section 4.1.1 the motivation behind diffractive imaging is given. Following this, the topics of coherence (section 4.1.2) and Fresnel and Fraunhofer diffraction (section 4.1.3) are introduced. In section 4.1.4 the ASM is demonstrated through the use of a simulation. The output of the simulation is used later in section 4.2 where it is compared to experimental results.

4.1.1 Motivation

When a medium is excited by an incident plane wave, the electron cloud corresponding to each atom in the medium will oscillate. Each atom then radiates a secondary electric field that will interfere with the original. The total field propagating within the medium is the sum of all these fields. The light beam leaving the medium is consequently dependent on its structure. Analysis of the the emitted beam is therefore a useful method for understanding the structure of a medium.

As interatomic distances inside a medium are on the order of 0.1 to 1 $\mathring{A}$, X-rays with a wavelength on this order can be used to provide information on the interatomic structure of the medium. HHG can produce wavelengths in the range 3 to 50 nm. Therefore, information about structures that are on this length scale or larger can be determined. These wavelengths could therefore provide shape information on objects such as nanostructures, viruses and large proteins.

In the past few years there has been great interest in using a HHG source for the understanding of small objects through diffraction. Although there have been some results for 'crystal' diffraction, including diffraction from

an array of polystyrene nanospheres that yielded the refractive index of polystyrene [93] (see chapter 5 for details of the experiment and analysis), the majority of the work has been using CDI. The technique of CDI was first demonstrated on a HHG source in 2007 with a resolution of 214 nm [94], followed by a resolution of 94 nm [11] in 2008. Both of these results used multiple reflections off narrow-bandwidth multilayer mirrors to modify the generated harmonic structure into a monochromatic source. In early 2009, results have shown that it is possible to use CDI with the entire generated harmonic spectrum, rather than a single wavelength, with a resolution of 165 nm [95]. In mid 2009, a resolution of 119 nm was achieved despite only illuminating the sample with a single 20 femtosecond (fs) pulse of 32 nm radiation [32].

The rapid progress in using HHG for CDI is due to the high generated flux, the fact that it is a relatively cheap laboratory-based source and therefore has good experimental access, and the expertise formed on other X-ray radiation sources. However, the science that is possible using HHG is only beginning to be explored. In the future it should be possible to combine nanometer spatial resolution with attosecond temporal resolution, with a harmonic spectrum that can optimised for many applications.

4.1.2 Coherence

The radiation generated by HHG in general possesses strong spatial coherence. However, the generated spectrum consists of multiple harmonics of the fundamental laser and therefore no interference is observed between different harmonics.

The spatial coherence can be defined by the visibility of a set of interference fringes. A source illuminating two slits will in general produce

interference fringes, caused by the constructive and destructive interference of the waves emanating from the two slits. However, the fringes will only possess a strong modulation if the light illuminating the two slits is coherent. In the case of weakly coherent light, the fringes may be difficult to distinguish. HHG radiation has been shown to possess strong spatial coherence, through demonstration of the double slit result [26]. Spatial coherence is a requirement for diffractive imaging.

HHG radiation does not possess high temporal coherence. Two light beams with different wavelengths will always interfere. However, the resultant interference fringes will only be observed if the detector can record the fringes faster than the beat frequency. In the case of HHG, the beat frequency is on the order of femtoseconds and hence no interference is generally observed between the different harmonics. Throughout this thesis, the observed diffraction patterns are therefore the incoherent sum of the diffraction patterns from each harmonic.

4.1.3 The Fresnel and Fraunhofer Approximations

The spatial profile of light that is diffracted by an object depends on the distance between the object and the imaging plane. For small distances, corresponding to Fresnel (or near-field) diffraction, the spatial profile can be calculated by propagating multiple waves from one plane to the next and considering the interference at each step. For large distances, corresponding to Fraunhofer (or far-field) diffraction, the spatial profile can be calculated by using the Fourier transform of the intensity and phase of the light immediately after the object. For computational reasons the spatial profile at large distances is therefore more convenient to calculate.

As shown in figure 4.1, the distance, z, needed for far-field diffraction

corresponds to a difference between the path lengths L_1 and L_2 of less than $\lambda/4$. For distances greater than this, the interference effects will not change significantly as the difference between the paths lengths L_1 and L_2 will remain small. The diffraction pattern will therefore not significantly change and instead will only scale. The condition for far-field diffraction is therefore,

$$z > \frac{2D^2}{\lambda} \tag{4.1}$$

where D is the object diameter, and λ is the wavelength of the light.

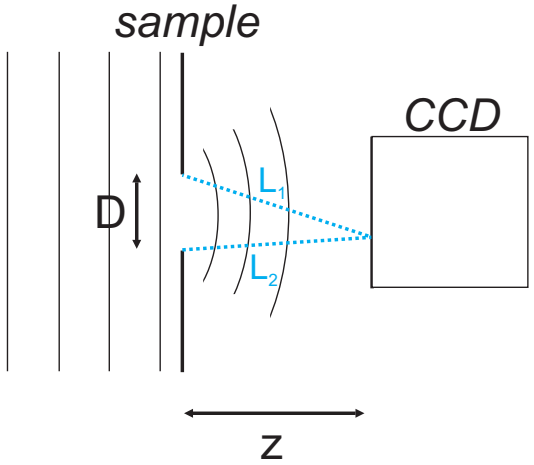

Figure 4.1: *Schematic of the requirement for far-field diffraction.*

4.1.4 Angular Spectrum Method

The far-field diffraction pattern from an object can be easily calculated; it is the modulus squared of the Fourier transform of the electric field immediately after the object. For large objects, the distance required for far-field diffraction may not be experimentally feasible. A technique for simulating a near-field diffraction pattern is therefore needed. In this section the ASM [85], which can be used to calculate Fresnel diffraction patterns, is described. However, it is important to realise that the ASM can be used

to calculate the diffraction pattern for any object to detector distance. To demonstrate the technique, the Fresnel diffraction pattern from an array of 2 μm diameter circular apertures is simulated and discussed. This theoretical sample is similar to the experimental sample shown in section 4.2. The simulated results show good agreement with the experimental diffraction patterns. The following paragraph explains the concept of the ASM.

The Fourier transform of the spatial intensity and phase distribution of a light beam immediately after an object yields the angular intensity and phase distribution. This represents the intensity and initial phase of plane waves propagating from the object for each angle, which can then be propagated to the imaging plane. The phase shift for each plane wave over a distance z is given by $\exp(ik_z z)$, where $k_z = \sqrt{k^2 - (k_x^2 + k_y^2)}$ is the component of the wavevector $k = 2\pi/z$ in the z direction. This result is then inverse Fourier transformed to recompose the angular distribution back into a spatial distribution. The modulus squared of this distribution yields the diffraction pattern at the imaging plane.

Figure 4.2 shows the simulated sample: a square array of 2 μm diameter circular apertures with a 4 μm basis, with a total width of 100 μm. Part b) shows a close-up of the data array, illustrating that the diameter of each circular aperture is 20 pixels. This resolution was chosen as a good balance between making the apertures circular and allowing a large number of such apertures in a 2048 by 2048 array. The underlying limitation here is the available computer memory.

Figure 4.3 shows the propagation of 27.6 nm light from the simulated sample, for different distances. Part a) shows the diffraction pattern at a distance of 1 mm. The simulated pattern looks like a 'shadow' of the sample, as light from each individual aperture does not strongly interfere with

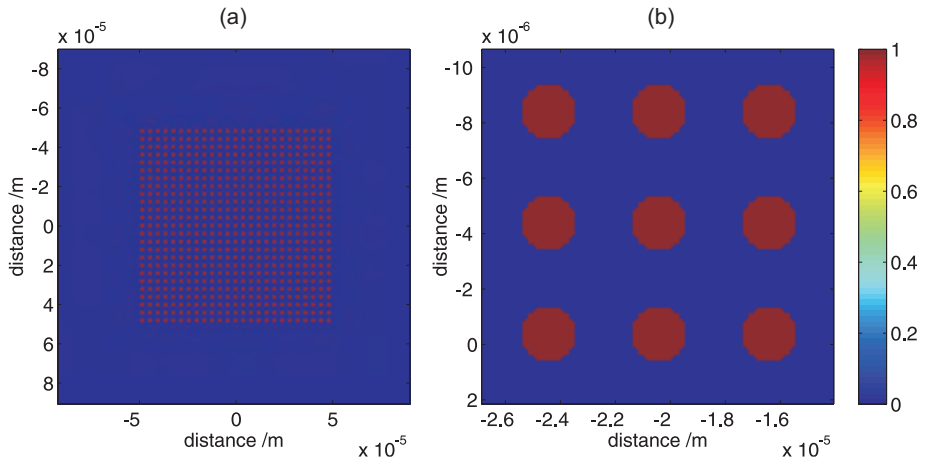

Figure 4.2: *Simulated sample, showing a) the whole sample and b) a close-up of the sample.*

light from adjacent apertures. Another limitation of the available computer memory now becomes apparent. The ASM composes a light field into an angular distribution, adds a phase shift, then recomposes the propagated light field back into a spatial distribution. The scaling in the final field is therefore identical to the starting field. This means that if a large propagation distance is chosen, the diffraction pattern may be larger than the size of the simulated data array. If a large distance is to be simulated using the ASM, the electric field may therefore need to be propagated a small distance, then re-sampled, then propagated another small distance. This inevitably leads to the loss of information, in particular the light that would be diffracted to wide angles. With improvements in computer memory, this inaccuracy could be avoided. Part b) of figure 4.3 shows the diffraction pattern at a distance of 1 cm. The distance scales are different as a result of the re-sampling. Strong interference between adjacent apertures is now observed, and a grid-like pattern is emerging. Part c) shows the pattern at a distance of 5 cm, which now has a distinct set of square apertures. This distance does not meet the condition $z > 72$ cm, and hence the pattern is

in the Fresnel diffraction regime. Part d) is the data in part c) shown on a logarithmic color scale.

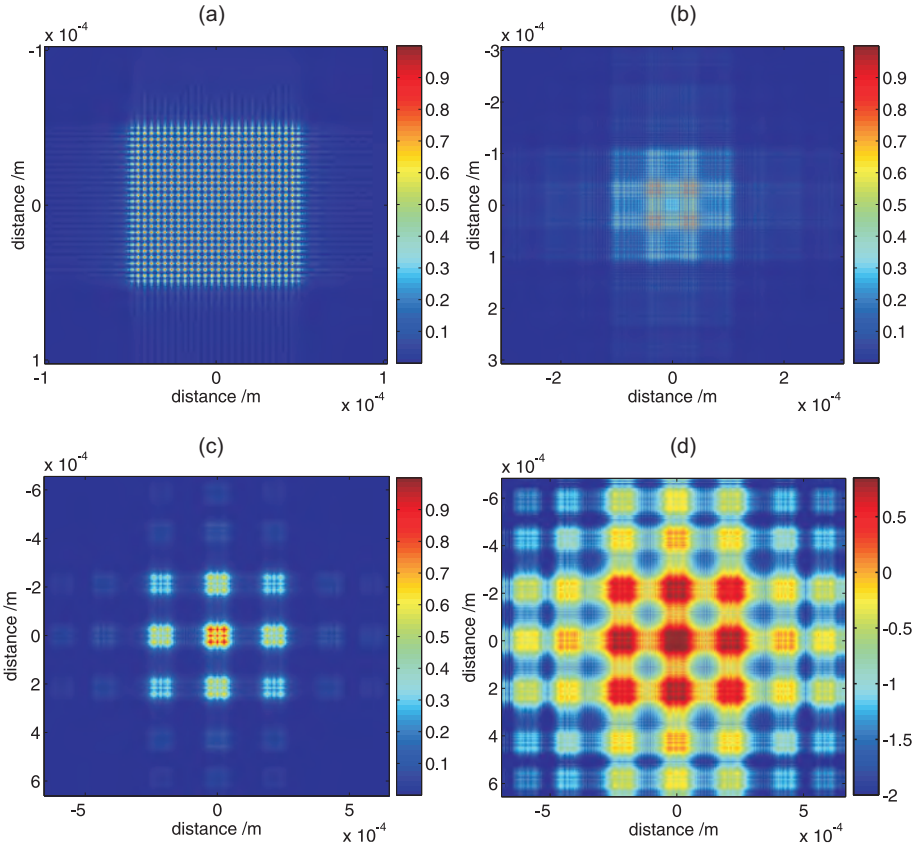

Figure 4.3: *Simulated intensity distribution at distances from the sample shown in figure 4.2: a) 1 mm, b) 1 cm, c) 5 cm and d) 5 cm shown on a logarithmic color scale.*

4.2 Fresnel Diffraction from a Periodic Sample

In this section, experimental diffraction results in the Fresnel regime from an array of 2 μm diameter circular apertures is presented and compared with results from the ASM simulation shown in section 4.1.4. The experimental setup has been described in section 2.5. The experimental results are taken under similar experimental conditions; they are described when

the results are presented in section 4.2.2. Importantly, one diffraction pattern corresponds to XUV radiation from a capillary and one from a gas cell. The difference in the generated XUV spectra is clear from the results. The ASM results from section 4.1.4 are adapted to take the spectral content into account; good agreement is shown with the experiment results. The experimental sample is described in section 4.2.1. The experimental results are shown in section 4.2.2. All experimental results were recorded with no XUV focussing optic and hence all generated wavelengths are incident on the sample, as opposed to a focussing optic which will in general alter the spectral nature of the source.

4.2.1 Sample

The sample, as shown in figure 4.4, is a square array of 2 μm diameter circular apertures, drilled into a 50 nm thick silicon nitride substrate. The sample was fabricated by Silson Ltd. As a silicon nitride sample can be fabricated as a single crystal, it can withstand large pressure differentials [96], making it a useful test sample. The entire sample is 500 x 500 μm. The hole-to-hole separation along the square axes is 4 μm. For the generated wavelengths, 50 nm of silicon nitride transmits $\sim$10% of the XUV and hence the substrate was coated with a 50 nm thick gold layer, which has a transmission of $\sim 5 \times 10^{-3}$. The diffraction pattern therefore only results from the light that is transmitted through the array of 2 μm apertures. As the sample was illuminated by the unfocussed XUV beam, which at the sample has an w_0 parameter of $\sim$1 mm, all the apertures are assumed to be illuminated by the same intensity. The sample can therefore be approximated by the simulated sample, as shown in figure 4.2. The only important difference is the overall sample size, which is 500 μm for the experimental sample but only

100 μm (due to computer limitations) for the simulation. This disparity is compensated by comparing the diffraction patterns for different distances; 11 cm for the experimental results and 5 cm for the simulation.

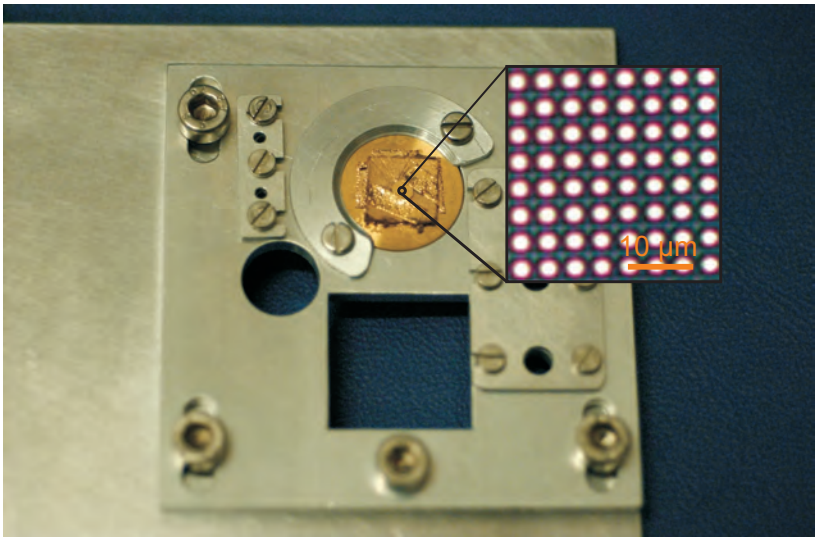

Figure 4.4: *Photograph of the periodic diffraction sample used in this chapter. The inset shows an optical microscope image of part of the sample.*

4.2.2 Experimental Results

In this section, Fresnel diffraction from the periodic sample is demonstrated. This is repeated under near identical conditions for both capillary and gas cell generated XUV. A comparison is then made with the simulated results. The high level of agreement demonstrates a good understanding of the XUV radiation and the diffraction sample. For both comparisons, the logarithmic color scales are not identical. This due to both the arbitrary intensity chosen in the simulation and to enhance the visibility of the wide angle structure. For the gas cell case, a beam block technique is used in order to improve the signal to noise ratio and to further illustrate the wide angle diffraction.

Figure 4.5 shows the recorded diffraction pattern for capillary generated

XUV using argon at a pressure of 70 mbar. Splitting in the interference peaks, a consequence of multiple wavelengths, can be observed for the wide angle diffraction peaks. The simulated result is for three XUV wavelengths. Although the overall structure of the simulation matches the experimental result, there are some discrepancies. Two of the 'missing' interference peaks are labelled by the pairs of arrows. Each purple arrow points to an interference peak which is expected but missing at the position of its orange counterpart arrow. This asymmetry is not produced by the simulation and is therefore believed to be a result of a non-square grid or sample tilt.

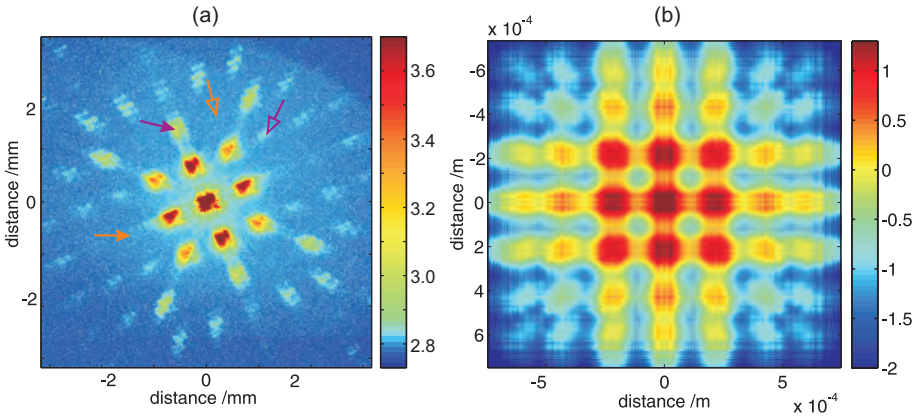

Figure 4.5: *A comparison of a) the experimental and b) the simulated Fresnel diffraction patterns. The experimental result corresponds to XUV generated inside a capillary. The simulated result contains the wavelengths 25.8 nm, 27.6 nm and 29.6 nm.*

Figure 4.6 shows the recorded diffraction pattern for gas cell generated XUV using argon at a pressure of 10 mbar. The simulated result includes seven wavelengths, illustrating that the gas cell generates approximately double the number of wavelengths as the capillary, for the described experimental conditions. Discrepancies that are similar to the capillary generated diffraction pattern are observed.

In general, the intensity of a diffraction pattern recorded at the centre of a detector is several orders of magnitude greater than the intensity recorded

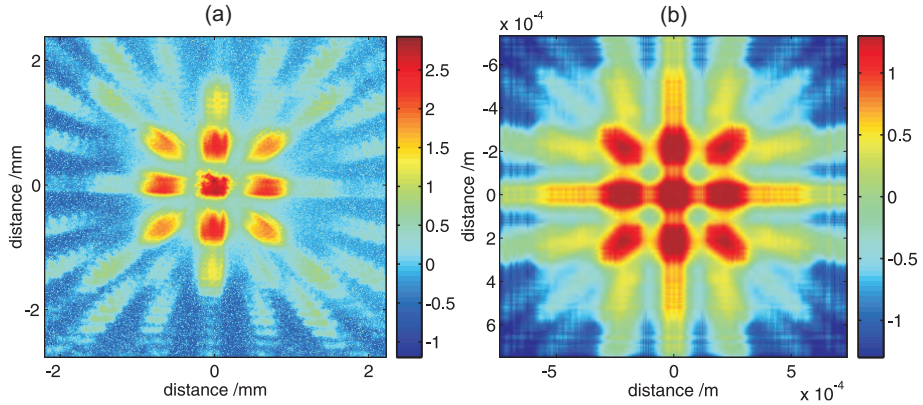

Figure 4.6: *A comparison of a) the experimental and b) the simulated Fresnel diffraction patterns. The experimental result corresponds to XUV generated inside a gas cell. The simulated result contains the wavelengths 22.8 nm, 24.2 nm, 25.8 nm, 27.6 nm, 29.6 nm, 32.0 nm and 34.8 nm.*

at the edge. Depending on the dynamic range of the detector, all or some of the wide angle information is likely to remain below the noise level even if the integration period is increased until the centre of the detector reaches the saturation limit. If a longer integration period is used, the centre of the image will become distorted. The usual technique to cope with this problem is to record and then concatenate two diffraction images: one that contains the whole image using a short integration period, and one with a long integration period with the central part of the detector blocked. Figure 4.7 shows the concatenated diffraction image using this described method. This is the full diffraction image from figure 4.6a). The beam block is a 3 mm diameter washer, held in place by a 120 μm diameter piano wire. The wire is visible in the image. The hard edge on the right hand side is due to an incorrect background subtraction image and not a problem with the technique.

Although far from ideal, this proof of principle experiment shows the advantages of using a beam block to enhance the signal-to-noise ratio at wide angles. An improvement to this procedure would be to introduce a

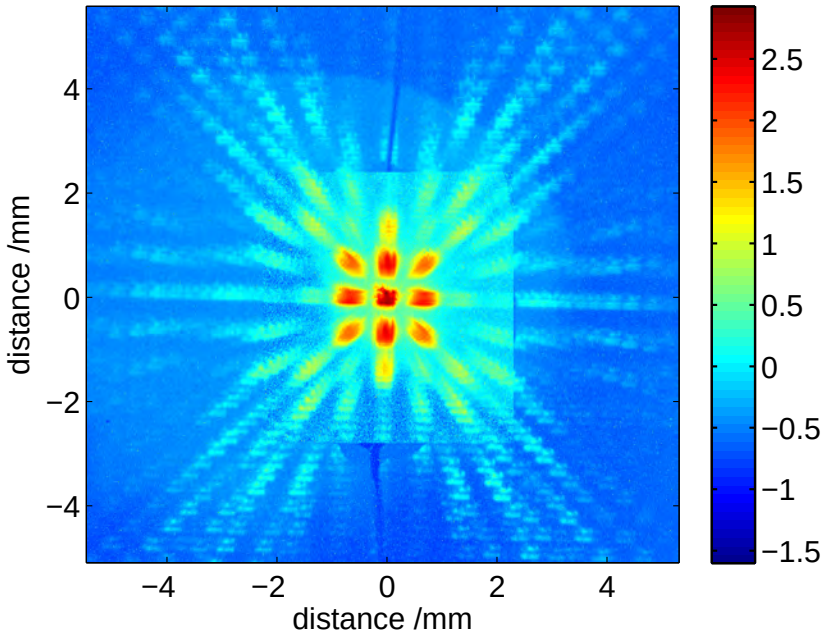

Figure 4.7: *Experimental diffraction image from the periodic sample for gas cell generated XUV, using the described beam block technique.*

series of circular beam blocks with different diameters, to further increase the dynamic range and to help reduce the transition between different integration times. Alternatively, a single beam block could be moved between the sample and the detector, changing its angular acceptance.

4.3 Introduction to Coherent Diffractive Imaging

An object is generally imaged by illuminating it and then collecting the diffracted light with an objective lens onto a detector. The smallest object size that can be observed is related to the wavelength of the light and therefore short wavelengths, such as XUV radiation, can produce a better imaging resolution than for visible light. However, due to the difficulties in making optics for short wavelengths, alternative methods of imaging are

often used. In this section, an alternative is presented in which the objective lens is removed and the object's diffraction pattern, rather than an image of the object, is recorded on a detector. An algorithm is then used instead of the objective lens to produce an image of the sample. This is known as coherent diffractive imaging (CDI).

When a far-field scattering pattern is recorded on a detector, the intensity is recorded but the phase information is lost. Therefore, an inverse Fourier transform cannot be used to determine the sample, as both the intensity and the phase are required. However, algorithms exist that can determine the phase of the scattering pattern for some special cases and hence allow the sample to be defined [7, 97]. These are known as phase retrieval algorithms. In this way, the algorithm actually replaces the imaging objective, and instead of the imaging resolution being limited by aberrations in the objective, the resolution is based upon the ability of the algorithm to find an appropriate solution [98].

A phase retrieval algorithm iterates between object space (the diffraction sample) and image space (the diffraction image) using the Fourier relation, and performs a process in each. In object space, there is assumed to be a region, known as the mask, which definitely contains the entire sample. This enables the algorithm to reduce the intensity outside the mask towards zero, as there is definitely no sample outside the mask. In image space, the algorithm replaces the simulated diffraction pattern with the experimentally observed diffraction pattern. The simulated phase, however, remains the same. After this process has been performed, the new result is Fourier transformed to the other domain, where the alternate process is performed. This can be repeated indefinitely. In general, after $\sim$100 iterations, the simulated sample closely resembles the actual diffraction sample. For a

1024 by 1024 array of double precision numbers, this typically takes a few minutes.

The algorithm is outlined in figure 4.8. An initial estimation of the sample, which has a random amplitude and phase, is Fourier transformed to generate the first guess of the diffraction pattern. The intensity distribution in this first guess is changed to the experimentally observed values, but the phase distribution is left unchanged. This result is inverse Fourier transformed to obtain the first iteration of the sample. Any intensities outside of the pre-defined mask are reduced or set to zero. This is then Fourier transformed to generate a diffraction pattern, where the intensities are once again matched with the experimental results. This cycle is continued for a fixed number of iterations or until the error between the iterated and experimental diffraction pattern is below a threshold.

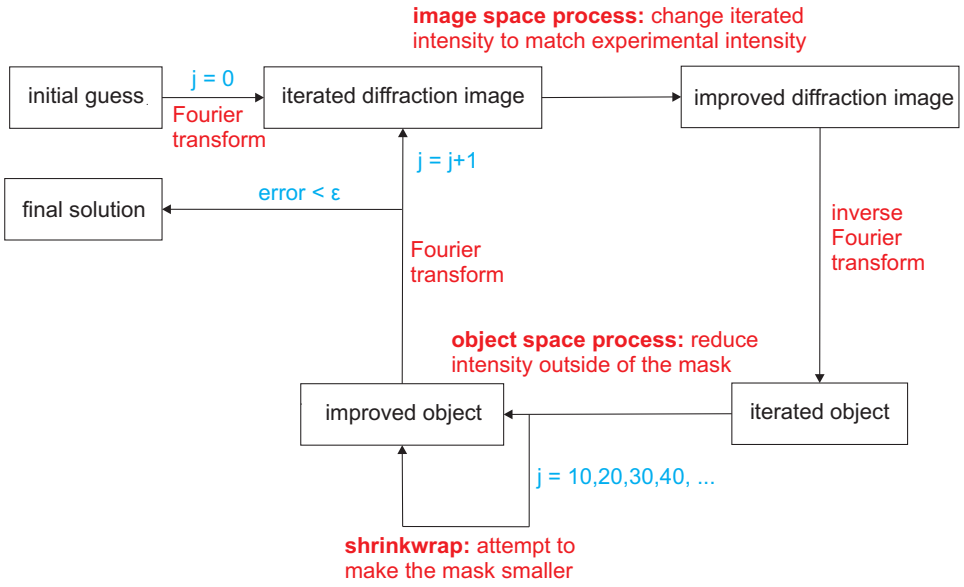

Figure 4.8: *A schematic of the phase retrieval algorithm used for CDI.*

If the iteration number is a member of a set of pre-defined values, such as every tenth iteration, the shrinkwrap modification [99] is used. This modi-

fication attempts to reduce the size of the mask and hence increase the area outside the mask that can then be reduced to zero. As this increases the strength of the object space constraint, the solution is generally improved. The shrinkwrap technique works by calculating the convolution of the current iterated sample and a Gaussian function, hence producing a 'blurred' version of the sample. All pixels that have intensities that are greater that a defined threshold are combined to form the new mask that is in general slightly smaller than the previous mask but still bigger than the sample.

4.3.1 Geometric and Algorithmic Requirements

There are two contradicting requirements for the experimental geometry for CDI. For a given detector, the phase retrieval algorithm in general converges more effectively when the diffraction pattern is sampled with a high resolution, corresponding to a large object to detector distance. However, the resolution of the solution image is highest when the diffraction image is recorded at a short distance from the sample, corresponding to a large angular acceptance for the detector. This section quantifies these statements in order to define the ideal experimental geometry.

There are two important concepts: the oversampling ratio and the image pixel size. Their mathematical definitions are given after this brief explanation. Firstly, the oversampling ratio describes the area of the region outside the mask in relation to the area inside the mask. A larger value corresponds to a larger area outside the mask that can be reduced in value in order to help the algorithm converge towards a solution. Simulations have shown that a value greater than two is required for a solution, but ideally the ratio should be larger than five [100]. Secondly, the image pixel size refers to the size of the reconstructed pixels in the solution. This represents the funda-

mental imaging resolution limit. A schematic of the imaging setup is shown in figure 4.9. Equations 4.2 and 4.3 can be derived from figure 4.9 and the paraxial approximation.

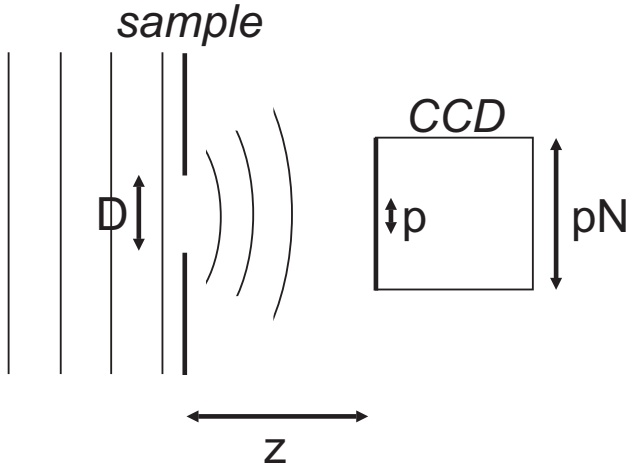

Figure 4.9: *Schematic of CDI imaging setup.*

The oversampling ratio can be determined by showing that θ_{pixel}, the small angle from the object corresponding to a single CCD pixel, can be described by both λ/D_{pixel} (from the Bragg relation) and p/z. This gives $D_{pixel} = z\lambda/p$. The oversampling ratio, defined as $O = D_{pixel}/D_{object}$, is then defined in terms of the experimental geometry by [94],

$$O = \frac{z\lambda}{pD_{object}} \tag{4.2}$$

where z is the sample to charge coupled device (CCD) distance, λ is the wavelength, p is the CCD pixel size and D_{object} is the size of the sample. This value can be made larger by increasing z or by decreasing D_{object}. Alternatively, the CCD pixel size can be reduced.

The image pixel size can be calculated similarly by showing that $\theta_{detector}$, the small angle from the object corresponding to the whole detector, can be described by $\lambda/D_{detector}$ and pN/z. The image pixel size is therefore defined

by,

$$D_{detector} = \frac{z\lambda}{pN} \tag{4.3}$$

where N is the number of CCD pixels. To decrease the image pixel size, either z can be decreased, or the size of the CCD increased (either through larger pixels or a greater number of pixels). However, if the CCD cannot be changed, this result contradicts the requirement for z to be large in order to obtain a large oversampling ratio. Therefore, in order to solve this geometric problem, the size of the sample, D_{object}, may need to be reduced. Figure 4.10 shows a) the oversampling ratio and b) the image pixel size as a function of the sample to CCD distance, for the CCD parameters used in this thesis. The vertical dashed lines represent the minimum possible distance in our experiment, due to the CCD being positioned 17 mm inside the camera. To obtain the best resolution, the CCD must be positioned at the minimum distance. This limits the sample to be no larger than 5 μm, as this will ensure an oversampling ratio value greater than five. The experimental results in the following section therefore use a sample that is 5 μm in diameter.

4.4 Coherent Diffractive Imaging of an Aperiodic Sample

In this section, experimental results are given that show the successful imaging of an aperiodic micron-sized object using the technique of CDI for XUV wavelengths. The object in this case is a combination of the sample shown in figure 4.4 and a 5 μm diameter aperture, separated by 55 μm. A schematic of this combination is shown in figure 4.11. Strong quantitative agreement

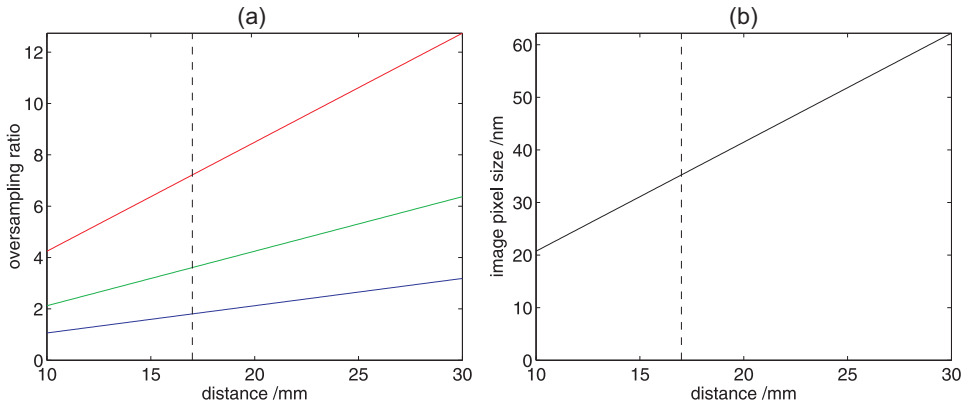

Figure 4.10: *Part a) shows the oversampling ratio for 5 μm (red), 10 μm (green) and 20 μm (blue) diameter samples as a function of the sample to CCD distance. Part b) shows the reconstructed image pixel size as a function of the sample to CCD distance. The vertical dashed line represents the minimum possible distance for our experiment.*

between the CDI solution and a white light microscope image is shown. The imaging resolution is $\sim$1 μm, believed to be a consequence of the multiple wavelengths in the incident XUV beam. Calculations show that the resolution will be reduced to $<$ 50 nm if the source is monochromatised. Work is currently underway to replicate the multiple wavelength phase retrieval algorithm presented in [95] (as briefly described earlier), as this is a route to improving the imaging resolution without the need to monochromate the XUV source.

In section 4.4.1, a microscope image of the sample is used to determine the relative positions of the 5 μm and 2 μm apertures. By using the ASM (described in section 4.1.4), the white light from the microscope is propagated through a 5 μm aperture for a distance of 55 μm, and a mask, corresponding to the array of 2 μm apertures, is overlaid on the result. With the relative positions determined, the ASM simulation is repeated for the generated XUV wavelengths. This XUV result is therefore the expected CDI solution. The experimental far-field diffraction pattern from the sample is

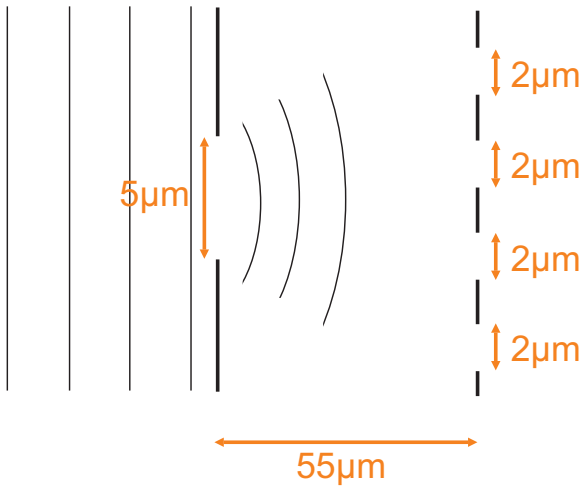

Figure 4.11: *Schematic of the CDI sample, showing the location of the 5 µm diameter aperture in relation to the array of 2 µm diameter apertures.*

shown in section 4.4.2. The CDI starting conditions, the algorithm output, and the final result are presented in this section.

4.4.1 Microscope Image of the Sample

Figure 4.12 shows the microscope image of a) the sample shown in figure 4.4 and b) the CDI sample as described in figure 4.11.

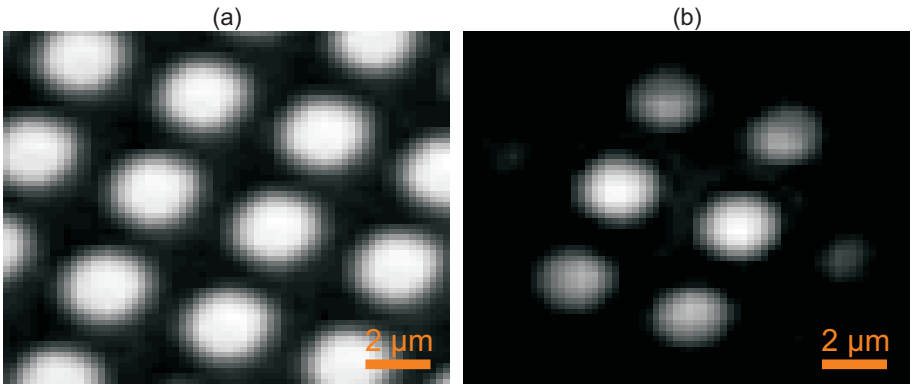

Figure 4.12: *Microscope images using visible radiation of a) the sample shown in 4.4 and b) the CDI experimental sample.*

There is an important difference between imaging the CDI sample with

visible and with XUV wavelengths. As the 5 μm aperture is similarly sized to the visible wavelengths used for the microscope, a significant amount of light is diffracted by the aperture. The result is that some 2 μm apertures that are not directly in the shadow of the 5 μm aperture will be illuminated by the visible radiation. Therefore the image in part b) contains a larger number of the 2 μm apertures than is geometrically predicted. However, the XUV wavelengths will be diffracted much less, and hence will illuminate fewer apertures. A direct comparison of the microscope image and the XUV CDI solution is therefore not appropriate. In the following paragraphs, the microscope image is analysed in order to determine the equivalent image that should be the CDI solution.

The relative intensities of the 2 μm apertures in figure 4.12b) contain information on the relative position of the 5 μm aperture. Figure 4.13 shows this microscope image. The labels A$\rightarrow$G refer to descending relative intensities at the 2 μm apertures. The two important considerations are: G is more intense than H, and C and D are more intense than E and F. This information enables the relative positions of the 5 μm and 2 μm apertures to be determined.

By using the ASM, the diffraction pattern for white light at a distance of 55 μm from a 5 μm aperture can be calculated. By overlaying this pattern onto a mask which corresponds to the array of 2 μm apertures, a comparison with the experimental microscope image can be made. This analysis is shown in figure 4.14. In part c) the data in part b) is averaged over each aperture, and the brightest to weakest apertures are labelled A$\rightarrow$G. This is directly comparable to figure 4.13 and shows that the relative position of the 5 μm and array of 2 μm apertures has been correctly identified.

The accuracy of the relative position of the sample can be determined by

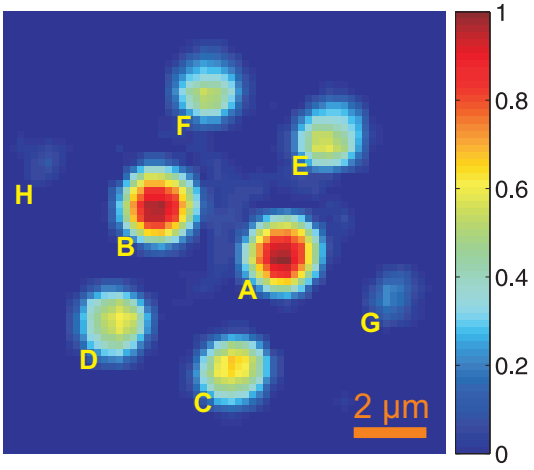

Figure 4.13: *Imported microscope image from figure 4.12b) shown on an RGB colormap to illustrate the relative intensities at the 2 µm apertures.*

comparing the intensity of each circle for the simulation and the microscope image. Figure 4.15 shows a comparison of the peak intensities of the apertures A→G in figure 4.13 and figure 4.14c). Surprisingly good agreement is shown given that the simulation only allows discrete positions for the mask, corresponding to movements of ∼120 nm, due to the pixel resolution.

Figure 4.16 shows the outcome when the ASM simulation is repeated using the three XUV wavelengths that are reflected from the XUV focussing mirror. This is therefore the expected CDI solution.

4.4.2 Experimental Results

In this section, the experimental XUV diffraction pattern from the sample is presented. This result is then used in the CDI algorithm to produce an image of the sample. The diffraction pattern is presented first, followed by an in-depth analysis of the algorithmic process. Figure 4.17 shows the diffraction image for an integration time of five minutes, displayed on a logarithmic scale. The data was recorded at a sample to CCD distance of 17 mm, producing to a good approximation a far-field pattern.

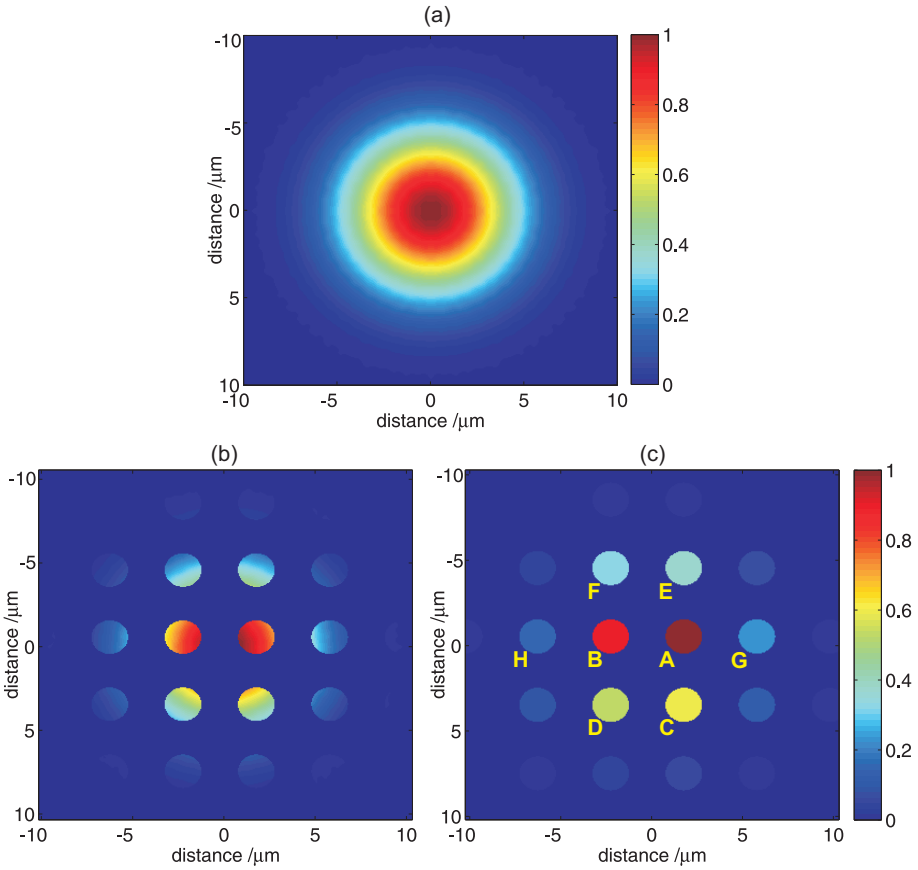

Figure 4.14: *An ASM simulation of a) white light at a distance of 55 µm after a 5 µm diameter aperture. Part b) shows this result overlaid with an appropriately positioned array of 2 µm diameter apertures. Part c) shows the mean value of each aperture.*

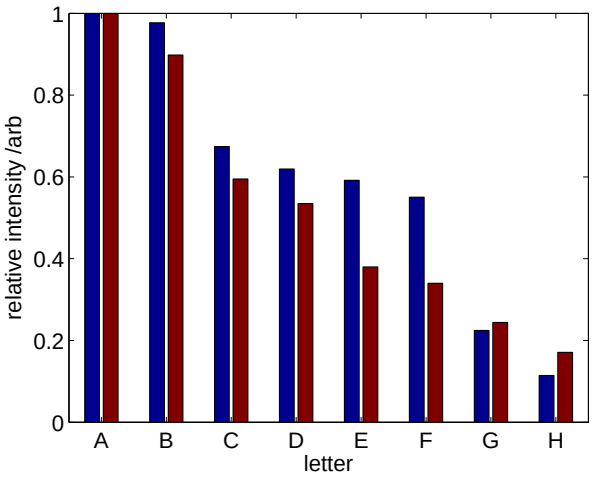

Figure 4.15: *A comparison of the experimental intensities measured using the microscope (blue bars, see figure 4.13) and the simulated intensities (red bars, see figure 4.14c)), confirming that the relative position of the 5 µm aperture and the array of 2 µm apertures has been correctly identified.*

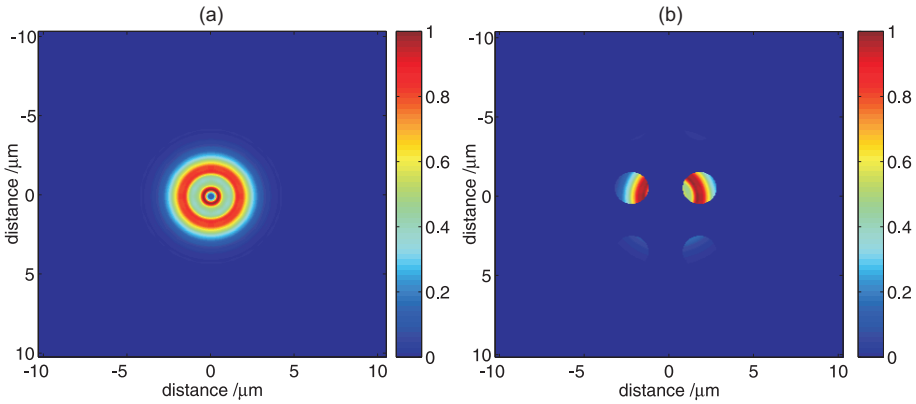

Figure 4.16: *An ASM simulation of a) XUV light at a distance of 55 µm after a 5 µm diameter aperture. Part b) shows this result overlaid with an array of 2 µm diameter apertures, in the previously calculated position.*

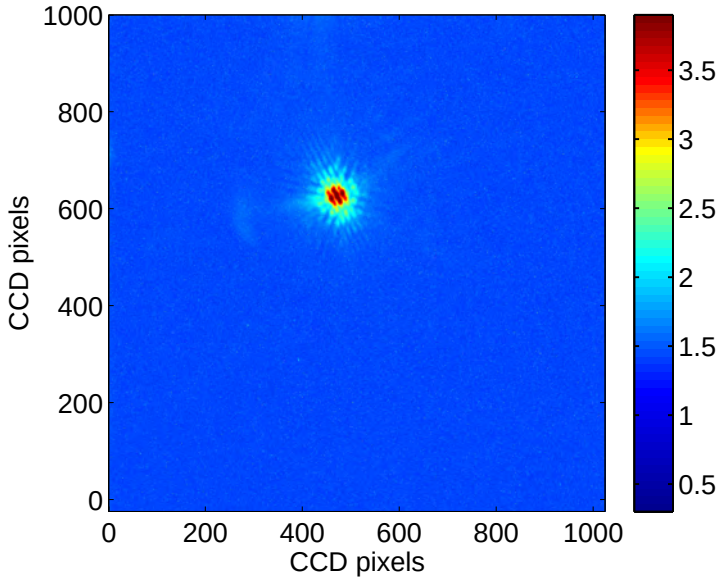

Figure 4.17: *Experimentally observed far-field diffraction pattern from the CDI sample. The data is displayed on a logarithmic scale.*

The rest of this experimental section is divided into three parts: the CDI starting conditions, the algorithm output, and the CDI solution. The first part shows the randomly generated initial intensity and phase distribution which is fed into the algorithm. The second part presents the sample intensity and mask at several iteration numbers through the reconstruction process. The third part shows the final result. Here, the structure of the predicted sample is reconsidered, and the experimental diffraction pattern is adapted in order to quantify the phase distribution of the XUV beam as it illuminates the sample.

Starting Conditions

In this section, the initial intensity and phase distribution is presented. The initial guess for the sample and the mask is generally the autocorrelation of the sample, which can be calculated by taking the inverse Fourier transform

of the experimentally observed diffraction image. This guarantees that the perfect solution is a subset of the starting condition and hence allows the algorithm to set the sample intensity that occurs outside the mask to a value of zero. The starting guess is shown in figure 4.18.

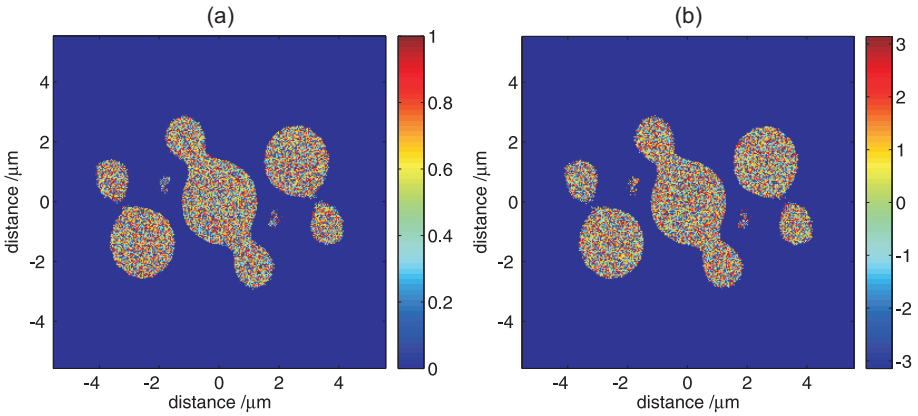

Figure 4.18: *The initial guess for a) the sample intensity and b) the sample phase. The distance scale is calculated from figure 4.10.*

Reconstruction Algorithm

As the starting condition is randomly generated each time the CDI algorithm is run, the output at each iteration is not always the same, even though the end result is usually very similar. In order to obtain a high-level understanding of the algorithm, it is useful to analyse the output for a single run. Described in this section are some of the algorithm iterations.

The algorithm is set to run for 200 iterations, and the mask is reduced in size using the Shrinkwrap algorithm every tenth iteration. The error reduction modification [7] is also used. This causes the sample intensity outside the mask to be reduced to 10% of its value for the first 100 iterations, and then reduced to 0% for the final 100 iterations. This encourages the algorithm to explore a large region of the parameter space for the first half and then fine-tune the solution in the second half.

Figure 4.19 shows the iteration numbers 1, 20, 40 and 60. Figure 4.20 shows the iteration numbers 80, 100, 150 and 200. The algorithm output is shown as two parts, the sample (left) and the mask (right). The mask generally appears to be a stage behind the sample. This is intentional, as the algorithm should be allowed to 'explore' the parameter space before the new (and hopefully better) mask is calculated. The correct sample is always assumed to be a subset of the mask. However, as shown in the figures, the mask can be incorrectly defined, and hence it must be allowed to increase in size if required. The following paragraphs summarise the progress at each step.

Iteration 1: The starting condition is shown. The mask is set equal to the shape of this initial guess of the sample. The final solution is always a subset of this mask. The sample shows a central spot, with two equally sized spots on either side.

Iteration 20: The algorithm has produced a sample that is three circles arranged in a line, and has updated the mask accordingly.

Iteration 40: The algorithm has now produced a sample that consists of only two circles. It is evident that the suitability of this solution is being tested, as the mask shows that three circles in a line is still the most likely solution at this stage.

Iteration 60: Now that the parameter space corresponding to two circles in a line has been explored, the algorithm has decided that two rather than three circles must exist. The mask has been updated accordingly.

Iteration 80: The solution corresponding to two circles cannot produce the observed diffraction image and therefore additional features in the sample are required. The algorithm is now exploring variants of the sample. Shown in the figure is a sideways extension on one of the circles. The mask

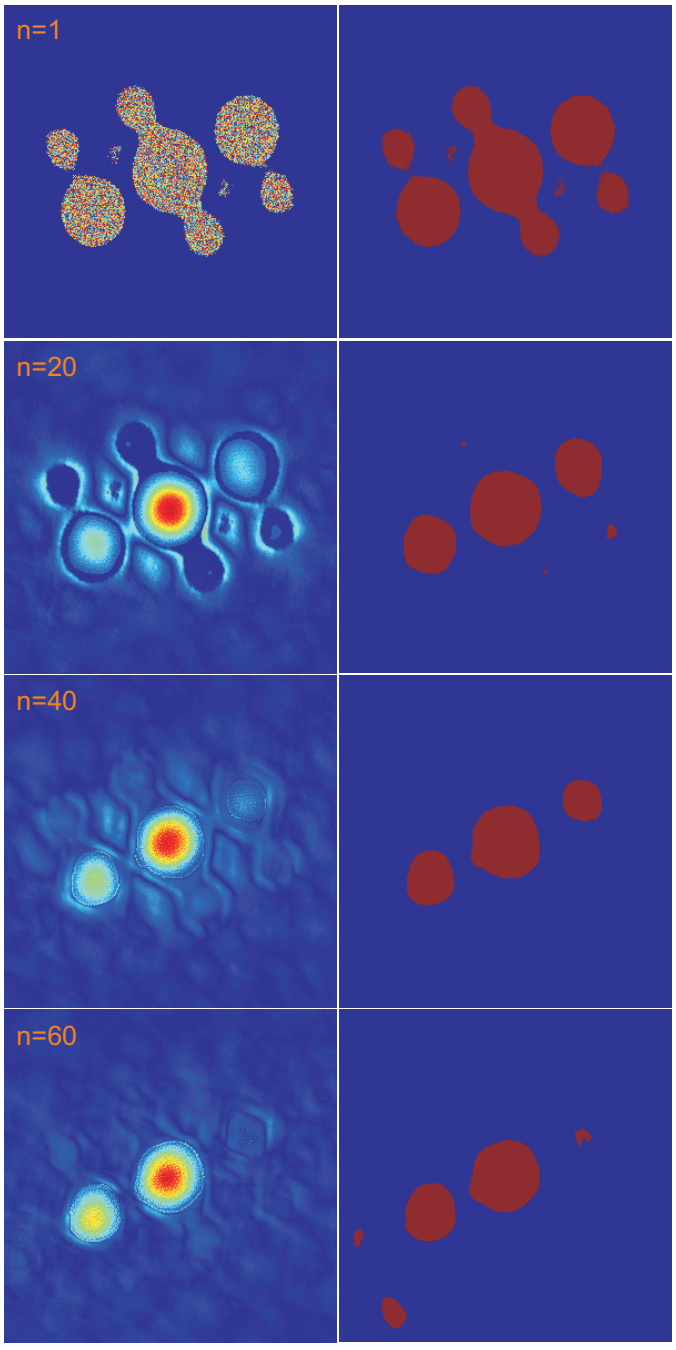

Figure 4.19: *Intensity (left) and mask (right) for the iteration numbers 1, 20, 40 and 60.*

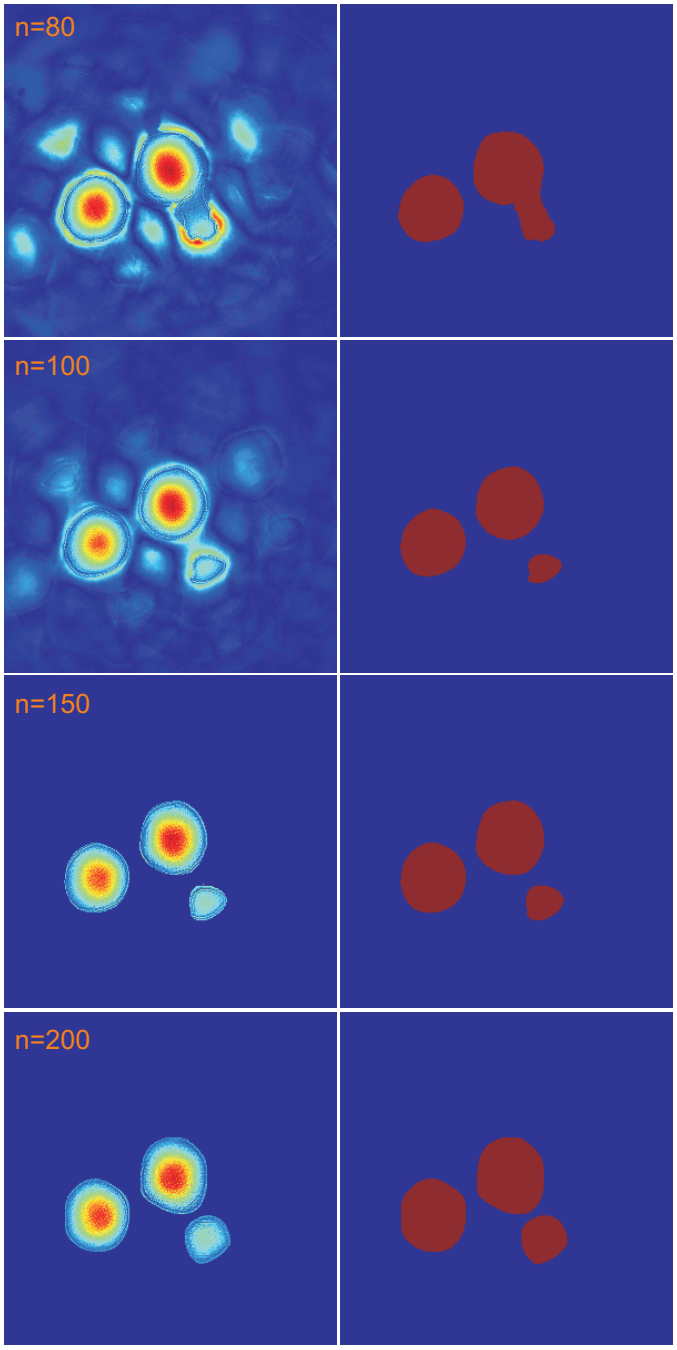

Figure 4.20: *Intensity (left) and mask (right) for the iteration numbers 80, 100, 150 and 200.*

is updated to take this extension into account.

Iteration 100: The algorithm is now halfway through the total number of iterations and therefore all intensity outside the mask is now reduced to zero during each iteration. This reduces the ability of the algorithm to search for another local minima, and instead the local parameter space is explored in order to refine the current solution. The extension has now formed a separate circle.

Iteration 150: The shape and intensity profile for the three circles is now optimised, and no further improvements are observed. This is believed to be a consequence of multiple XUV wavelengths in the experimental diffraction pattern.

Iteration 200: The final solution shows three circles, where one is both clipped and noticeably less intense. The central circle is slightly more intense than the left circle.

CDI Solution

Figure 4.21 shows the final solution. The intensity, presented in part a), shows relatively good agreement with the visible microscope image in 4.13, but it is clear that the solution is not exactly what was predicted. The most likely reason for this is a small sample tilt. As the distance between the 5 μm aperture and the array of 2 μm apertures is much larger than the periodicity of the array, a small tilt angle would significantly change the set of illuminated 2 μm apertures. A tilt angle of 4.15 degrees would result in a sideways distance of 4 μm, which is the periodicity of the array. By using the CDI solution, the most likely sample tilt can be determined. Figure 4.22 shows the simulated sample under XUV illumination, for a tilt angle of 1.6 degrees. This result is now very similar to the CDI solution; the relative

intensities of the three apertures now show good agreement.

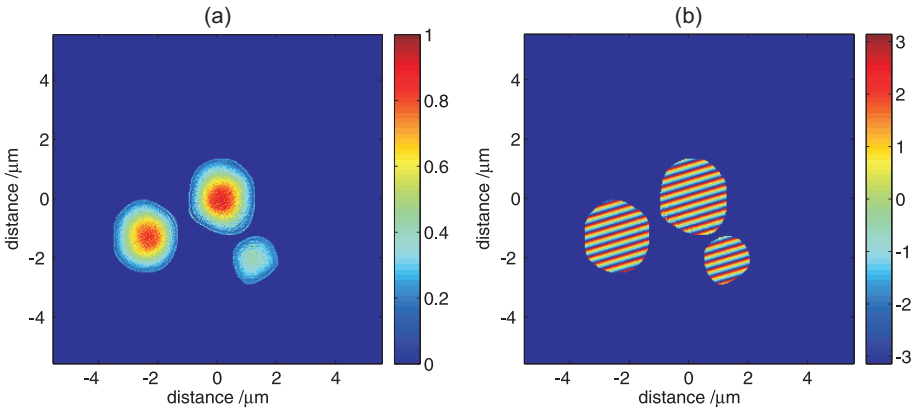

Figure 4.21: *Final values for the a) intensity and b) phase of the CDI sample. The distance scale is calculated from figure 4.10.*

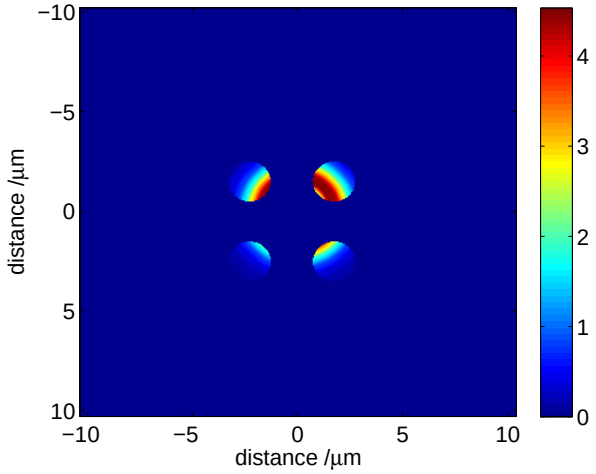

Figure 4.22: *An ASM simulation the CDI sample with a tilt angle of 1.6 degrees, for XUV wavelengths. Good agreement is now shown with the experimental result in figure 4.21.*

The phase of the CDI solution, as shown in figure 4.21b), is strongly sloped. This is a consequence of the experimental diffraction pattern (shown in figure 4.17) being centred towards the edge of the CCD. In order to explain the apparent change in direction of the beam after the sample, the algorithm has determined that the sample must have strongly altered the

phase of the XUV beam. However, the off-centre diffraction pattern is really a consequence of a misaligned CCD. The sloped phase is therefore an artifact of the way the experimental data was recorded. If the diffraction pattern was central on the CCD, the phase of the CDI solution would then correspond to the phase of the XUV beam at the sample. The XUV beam phase can still be determined, however, by padding the outside of the experimental data array with zeros, cropping the data so that the most intense region is then central and then running the CDI algorithm on this new diffraction pattern. This result is shown in figure 4.23 where the phase now corresponds to the phase of the XUV beam immediately after the array of 2 μm apertures. The intensity profile is similar to figure 4.21a) and therefore demonstrates the repeatability of the CDI process.

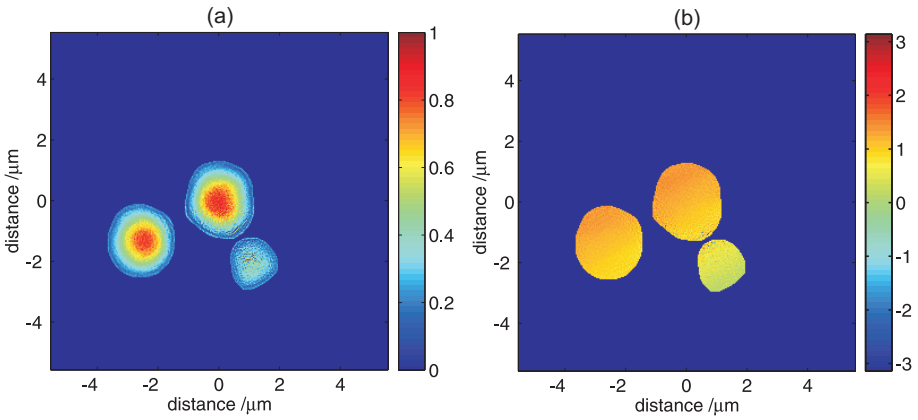

Figure 4.23: *CDI solution for the centralised diffraction pattern showing the a) intensity and b) phase. The distance scale is calculated from figure 4.10.*

4.5 Conclusion

This chapter has shown the successful reconstruction of a micron-sized sample. Due to the multiple wavelengths present in the incident XUV beam, the resolution was limited to around 1 μm. However, the imaging resolution is

predicted to be better than 50 nm once the source is made monochromatic. This is likely to be achieved in the near future using a mirror with a narrow reflected bandwidth. Preparation is currently underway by group member Chapman to produce a tobacco mosaic virus sample for XUV CDI. This will move the project towards its overriding objective of single molecule imaging.

This chapter has also shown Fresnel diffraction from an array of 2 μm diameter apertures. The ASM was used to simulate the data with some success. However, differences in the number of interference peaks were observed, which are believed to be a consequence of defects in the sample.

Chapter 5

Simultaneous Determination of Structure and XUV Dielectric Constant of a Nanoscale Object

High Harmonic Generation (HHG) has the ability to generate a high flux of extreme ultraviolet (XUV) radiation across many discrete wavelengths. For diffraction experiments, an optical technique is generally used to attenuate all but one of the harmonics. This wavelength selectivity can be achieved by reflections off narrowband multilayer mirrors. However, each reflection will also attenuate the harmonic of interest. Therefore both the total flux and the flux in the brightest harmonic is reduced. One of the unique and striking features of HHG is the spectral comb that is generated. New scientific techniques should therefore be devised to use this property. By using the comb of harmonics and a periodic diffraction sample, this chapter shows how

the refractive index of a material can be calculated for multiple wavelengths from just a single diffraction image. The refractive index is extremely difficult to measure accurately in the XUV spectral region due to the high absorption for almost all materials. The structure of the diffraction sample and its defects can also be quantified from the same diffraction image. Therefore the technique presented in this chapter is a simultaneous imaging and spectroscopic technique.

This chapter is organised as follows. Section 5.1 provides the motivation for this investigation. Section 5.2 shows the nanoscale sample and describes the fabrication technique. Section 5.3 describes the theoretical background, which includes Mie scattering and the application of some crystal lattice theory. The experimental XUV diffraction pattern is shown in section 5.4. The technique for extracting the refractive index from the diffraction image is presented in section 5.5. The generality of this technique is explained in sections 5.6 and 5.7, where the application of other diameters and refractive indices is explored. The structure of the nanosphere array can also be determined from the same diffraction image. Section 5.8 compares diffraction images from different regions on the sample, showing the possibilities of this radiation source for analysing grain boundaries. The application of coherent diffractive imaging (see section 4.4) to a diffraction pattern with discrete interference peaks is also investigated in this section. A summary of this chapter is presented in section 5.9.

The refractive index of a material for X-ray wavelengths is usually described in the form $(1 - \delta) + i\beta$, where δ is nearly always positive and β is always positive. The real part corresponds to the phase shift caused by the material and the imaginary part corresponds to the absorption from the material. In this chapter, when referring to the refractive index, the terms

real and *imaginary* are used to refer to the values of δ and β respectively, unless explicitly stated otherwise. The term *refractive index* is used to refer to the combination of the real and imaginary component.

5.1 Motivation

To understand the interaction between light and matter, the refractive index of the medium at the wavelength must be known. Due to the large number of absorption edges in the XUV spectral region, the refractive index can change rapidly. The two tabulated references for the refractive index in the XUV are Henke [65] and Chantler [101]. Henke's publication consists of all experimentally-measured values for the photoabsorption cross-section of elements, and from this the refractive index values are calculated. Chantler's publication takes a theoretical approach using quantum mechanics and other techniques to help predict the refractive index for each element.

As an example of the data available, a figure from the Henke publication is presented. Figure 5.1 shows the experimentally measured photoabsorption cross-section for hydrogen. The black dots represent experimental data points, and the black line is a best fit of this data. Within the most intense part of the HHG spectrum, illustrated by the red box, there are no experimental data points. Therefore the best fit line must be extrapolated between a set of data at wavelengths that have double the energy, and a single data point at 20 eV. Kramers-Kronig analysis is then performed on this best fit line to obtain the refractive index. There is therefore a significant error in both the tabulated real and imaginary refractive index components for hydrogen in the XUV spectral region. In fact, no value for the real part of the refractive index is given for energies less then 50 eV. Similar problems exist for nearly all elements. Carbon, for example, has a larger number

of photoabsorption data points, but individual data sets in general do not agree and a weighted best fit line must be drawn between them in order to calculate the complex refractive index.

Figure 5.1: *The tabulated photoabsorption cross-section results and best fit line for hydrogen (adapted from [65]), showing a lack of experimental data points in the most intense part of the generated HHG spectrum, illustrated by the red box.*

Although some experimental refractive index data exists for elements, there are very few experimental measurements for the refractive index of compounds in the XUV. The refractive index for a compound is instead usually approximated by combining the refractive indices of the constituent elements in the ratios that they exist in the compound [65]. The interaction between the atoms is therefore ignored. However, the susceptibility of hydrogen, for example, changes significantly when it is bonded in a compound, especially at XUV wavelengths [101]. An experimental measurement is therefore required.

A major issue lies with the difficulty of directly measuring the real part of the refractive index. The Kramers-Kronig analysis requires a large number of absorption values for different wavelengths before a single value can be determined. A direct experimental measurement of the real part is therefore often desirable. Current techniques for determining the real part in regions

of high absorption typically require a large number of single-wavelength reflectivity versus angle measurements [102]. In this case, the error between the experimental and Fresnel reflectivity curves can be minimised in order to extract the refractive index. There are three properties of this technique that should be improved. Firstly, measuring the reflectivity as a function of angle requires a different geometry for each measurement. A single measurement technique would be significantly better. Secondly, a technique where the theoretical curve varies extremely strongly with changing real and imaginary components will result in a higher accuracy. Thirdly, the Fresnel reflectivity technique only works for a single wavelength, and hence must be repeated many times. Ideally, multiple wavelengths should be tested simultaneously. Presented in this chapter is a measurement technique that meets all these criteria.

The way that light interacts with a sphere that is similarly sized to the wavelength is heavily dependent upon both the real and imaginary components for the refractive index of the sphere. It is this property that is used in this chapter. Measuring the intensity of light that is scattered by a single sphere as a function of angle allows the refractive index to be determined, as the error between the experimental and theoretical results can be minimised by changing the theoretical refractive index components. However, this will only work for a single wavelength as the intensity for multiple wavelengths at a particular angle will overlap. By using an array of spheres, destructive interference will occur, resulting in interference peaks for different wavelengths that are offset. This enables the refractive index for multiple wavelengths to be measured simultaneously. Using this technique, the refractive index for polystyrene ($C_6H_5CH\text{-}CH_2$) at three wavelengths (26.8 nm, 27.6 nm and 29.6 nm) has been experimentally determined.

Polystyrene was chosen as the material to investigate, as Chau, a PhD student at the University of Southampton, had previous experience using polystyrene nanospheres to make single-layer hexagonal arrays. The generality of this technique is discussed extensively in section 5.7.

5.2 Sample Fabrication

With help from Chau, a single-layer, hexagonal array of polystyrene spheres (Duke Scientific Corp.), with an average diameter of 196 $\pm$ 1.2 nm and density of 1.05 g/cm^3, was fabricated onto a 50 nm thick silicon nitride substrate (Silson Ltd). The size of the spheres was calculated by measuring the average length of three sets of fifty spheres (taken along a lattice direction) and the error in this measurement was combined with the error in the scanning electron microscope (SEM) calibration of 10 nm. The substrate is 500 μm by 500 μm. Figure 5.2 shows an SEM image of a section of the sample. The sample was fabricated by floating a single layer of nanospheres on the surface of water whilst the silicon nitride window was supported immediately below the surface [103]. When the water was slowly removed, the spheres formed a single-layer hexagonal array on the substrate.

5.3 Theoretical Background

This section provides an understanding of the interaction between the XUV and the nanosphere sample. By combining the Mie solution to Maxwell's equations and parts of crystal lattice theory, a set of differential equations can be produced that describe the far-field diffraction pattern resulting from the illumination of a hexagonal array of nanospheres.

The sample is a 2D hexagonal array of nanospheres, which is equiva-

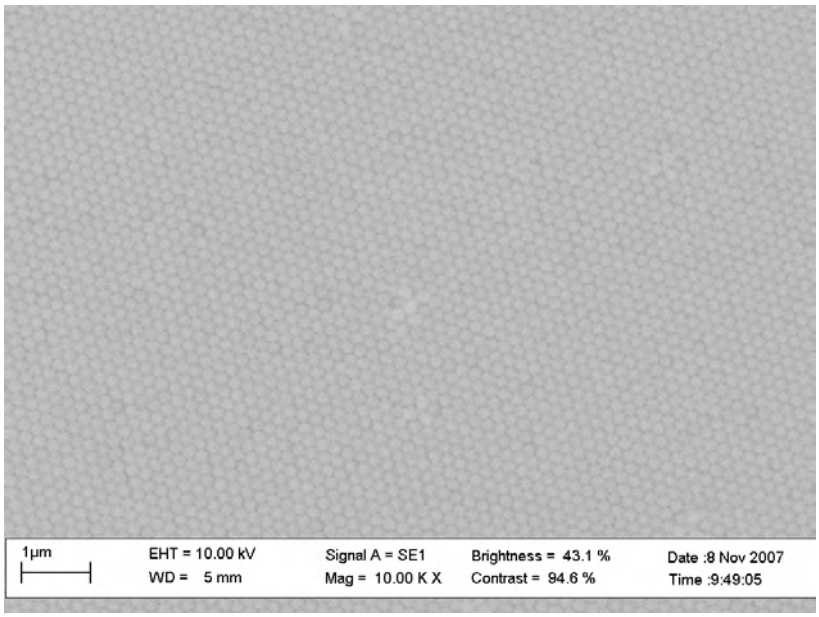

Figure 5.2: *SEM image of a region on the hexagonal nanosphere sample showing a ∼20 µm area of the sample that is a single crystallite with minor defects.*

lent to the convolution of a hexagonal array of delta functions and a single nanosphere. The far-field diffraction pattern from the sample is therefore the Fourier transform of the array of delta functions multiplied by the far-field scattering pattern from a single nanosphere. The result is therefore a hexagonal array of delta functions that have an intensity dependent on the far-field scattering pattern from a single nanosphere. An application of crystal lattice theory can be used to calculate the angles of the interference peaks. The Mie solution can be used to determine the far-field scattering pattern. The Mie solution is described in section 5.3.1. The application of crystal lattice theory to this problem is given in the following paragraphs.

To describe the array of spheres, it is convenient to introduce the Bravais lattice. It is defined as an infinite array of points such that a crystal will look identical from whichever of the points it is observed from. The position of each point is described by the vector,

$$\mathbf{R} = n_1\mathbf{a}_1 + n_2\mathbf{a}_2 + n_3\mathbf{a}_3 \tag{5.1}$$

where $\mathbf{a}_1$, $\mathbf{a}_2$ and $\mathbf{a}_3$ are three vectors not all in the same plane, and n_1, n_2 and n_3 are integers. For the hexagonal array of spheres, possible values for $\mathbf{a}_1$, $\mathbf{a}_2$ and $\mathbf{a}_3$ are given as,

$$\mathbf{a}_1 = \frac{\sqrt{3}a}{2}\mathbf{x} + \frac{a}{2}\mathbf{y} \tag{5.2}$$

$$\mathbf{a}_2 = a\mathbf{y} \tag{5.3}$$

$$\mathbf{a}_3 = c\mathbf{z} \tag{5.4}$$

where a is the diameter of a sphere, and x, y and z are unit vectors along the x, y and z axes, as defined in figure 5.3. As the lattice is a single layer, the constant c will be infinite in this case.

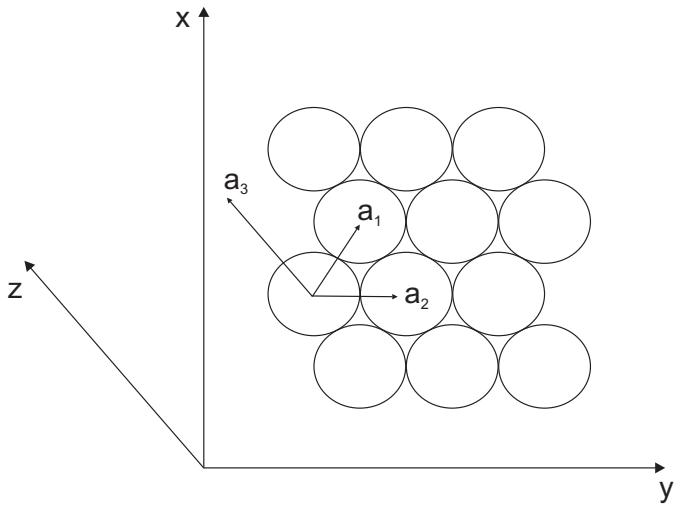

Figure 5.3: *Definition of $\mathbf{a}_1$, $\mathbf{a}_2$ and $\mathbf{a}_3$ in terms of the x, y, and z axes, illustrating a hexagonal array, looking along the axis of XUV propagation.*

The reciprocal lattice vectors correspond, and are in a direction normal, to a set of real space lattice planes. They are defined by,

$$\mathbf{b}_1 = 2\pi \frac{\mathbf{a}_2 \times \mathbf{a}_3}{\mathbf{a}_1 \cdot (\mathbf{a}_2 \times \mathbf{a}_3)} \tag{5.5}$$

$$\mathbf{b}_2 = 2\pi \frac{\mathbf{a}_3 \times \mathbf{a}_1}{\mathbf{a}_1 \cdot (\mathbf{a}_2 \times \mathbf{a}_3)} \tag{5.6}$$

$$\mathbf{b}_3 = 2\pi \frac{\mathbf{a}_1 \times \mathbf{a}_2}{\mathbf{a}_1 \cdot (\mathbf{a}_2 \times \mathbf{a}_3)} \tag{5.7}$$

For any vector K, defined by,

$$\mathbf{K} = k_1\mathbf{b}_1 + k_2\mathbf{b}_2 + k_3\mathbf{b}_3 \tag{5.8}$$

where k_1, k_2 and k_3 are integers, there is a lattice plane normal to K and with a separation d, where $2\pi/d$ is the length of the shortest reciprocal lattice vector parallel to K. Knowledge of the lattice plane separations enable a calculation of each of the angles of the diffraction interference peaks from the nanosphere sample. The first five lattice plane separations for a sphere diameter of 196 nm are: 169.7 nm, 98.0 nm, 84.9 nm, 64.2 nm and 49.0 nm.

5.3.1 Mie Scattering Theory

The Mie solution to Maxwell's equations can be used to show how light is scattered by a spherical object and hence provide an intensity versus angle distribution. A schematic of this interaction is presented in figure 5.4.

When an electromagnetic field crosses the boundary between a medium and a particle, the permittivity and permeability will generally change.

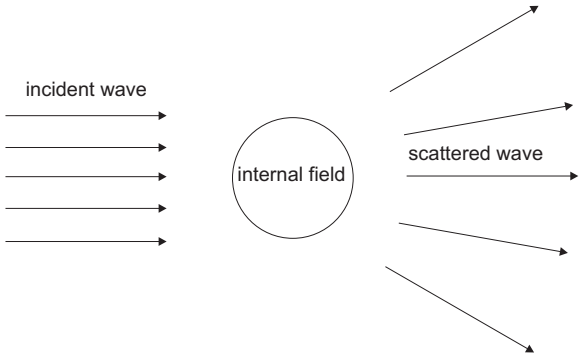

Figure 5.4: *The interaction of light and a spherical object can be modelled by considering the electric field inside the spherical object. From this, the scattered wave can be calculated.*

Across this discontinuity, the components of the field that are tangential to the surface of the particle must be continuous. This boundary condition, defined in equations 5.9 and 5.10, can be used to determine the electromagnetic field inside the particle. In this case, $\mathbf{n}$ is a unit vector normal to the surface of the particle, and $\mathbf{E}$ and $\mathbf{H}$ are the electric and magnetic fields. The subscripts refer to the field inside (1) and outside (2) the particle.

$$[\mathbf{E}_2 - \mathbf{E}_1] \times \mathbf{n} = 0 \tag{5.9}$$

$$[\mathbf{H}_2 - \mathbf{H}_1] \times \mathbf{n} = 0 \tag{5.10}$$

These boundary conditions are used in conjunction with the expansion of a set of vector plane waves, which correspond to the incident radiation, into polar coordinates. This enables the amount of light that is scattered to a particular angle to be calculated. A summary of the derivation is shown in appendix A.

Figure 5.5 shows the scattered intensity as a function of angle for 27.6 nm light incident on a spherical object with a diameter of 196 nm and values

of 0.0917 and 0.302 for δ and β respectively. An angle of zero represents undeflected light and an angle of π represents light that is deflected back towards the radiation source. The distribution is calculated for a single azimuth angle, defined as the direction of a one dimensional line across a plane that is parallel to the imaging plane. Due to the effects of polarisation, light is scattered slightly differently for azimuth angles that are perpendicular and parallel to the XUV polarisation. In all analysis in this chapter, an average across all azimuth angles is presented, as the difference between them is small for the angles investigated.

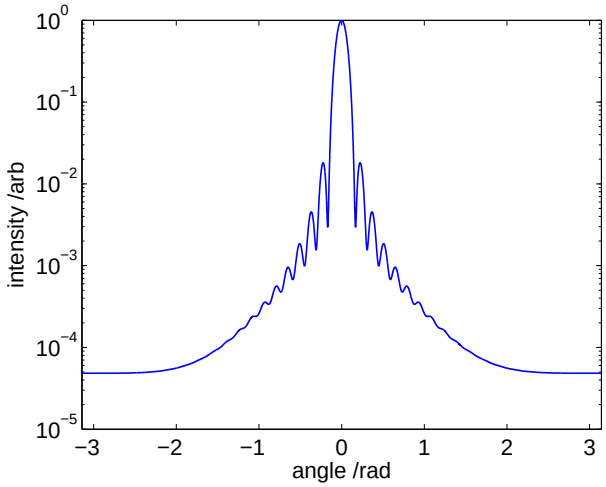

Figure 5.5: *Intensity versus angle distribution of 27.6 nm light scattered from a single 196 nm diameter sphere with values of 0.0917 and 0.302 for δ and β respectively.*

5.4 Experimental Results

In this section the experimentally measured diffraction pattern from the hexagonal array of spheres is presented. The sample was positioned at the focus of the multilayer mirror (see section 3.1) using radiation produced by the gas cell XUV radiation source (see section 2.5). The CCD was positioned

at a distance of 17.7 mm away from the sample.

In order to test if this diffraction pattern is far-field, the angular spectrum method (ASM) (as explained in section 4.1.4) has been used to simulate the XUV diffraction pattern from a hexagonal array of circles for the experimental distance. Due to limited computer memory, the circles were set to a 5 μm diameter. This diffraction pattern was compared with the simulated far-field diffraction pattern. The simulated sample was illuminated with a Gaussian beam with the experimentally measured w_0 parameter. The difference in the intensity of the diffraction peaks for the ASM calculation and the far-field calculation was 0.2%. As the polystyrene spheres are more than ten times smaller than the simulated circles, the percentage difference will be much less. The experimental diffraction patterns shown in this chapter are therefore far-field to a good approximation.

Figure 5.6 shows the experimentally observed diffraction pattern for an integration time of 240 seconds. Approximately six discrete sets of interference peaks are observed, as the sample is illuminated by multiple XUV wavelengths that are diffracted to slightly different angles.

An image was also recorded for the same period of time with no gas present in the gas cell. This enabled a background subtraction of the laser leakage and provided a data set that is the sum of the number of XUV photons plus a random noise component for each CCD pixel. All analysis was performed on this background subtracted data set.

As the multiple diffraction peaks correspond to the different generated wavelengths, an appropriately angled intensity profile through the diffraction pattern can therefore be used to determine the harmonic spectrum that is incident on the sample. This corresponds to the spectrum that is reflected from the multilayer mirror. When using this method, a small correction may

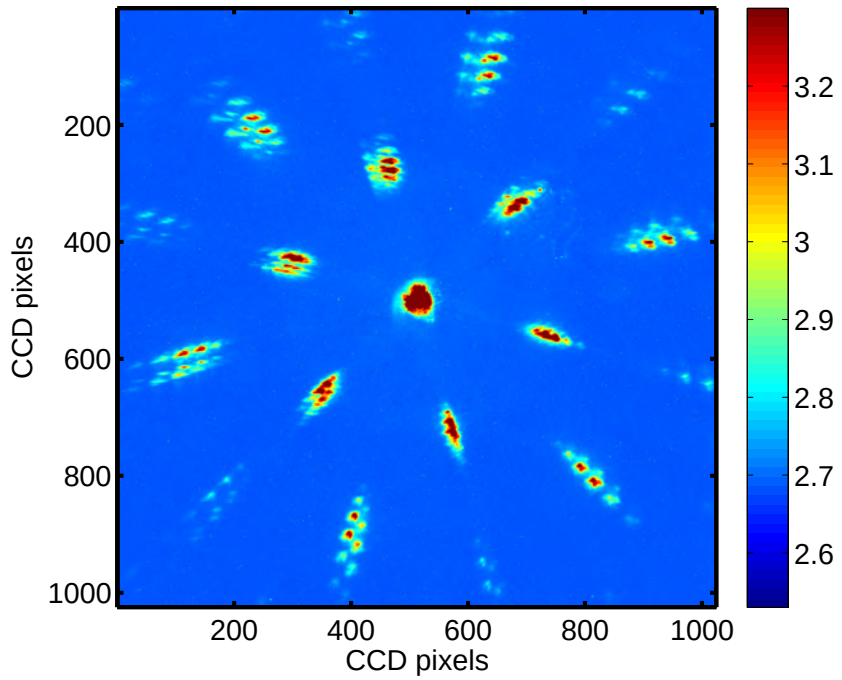

Figure 5.6: *Experimentally observed XUV far-field diffraction pattern from the hexagonal array of spheres, for an integration time of 240 seconds, displayed on a logarithmic intensity scale.*

be required, as the refractive index and hence the amount of light scattered may not be constant across the spectral region. This method was used to produce the spectrum shown in figure 3.4. Calculations have shown that in this case the spectral intensity extracted from the CCD image is within 5% of the spectrum incident on the sample. However, this might not be the case if an absorption edge existed within the spectral region. An explanation for the radial interference peak splitting was presented in section 3.1.4.

In addition to the diffraction pattern, to calculate the refractive index of the sphere material a measurement of the size of the spheres and the fundamental laser wavelength is required. These measurements can be used to calculate the generated XUV wavelengths, the sample to CCD distance (L), the interference peak size and subsequently the refractive index.

Firstly, the generated wavelengths and L are calculated using an error minimisation technique. Using the diffraction pattern, the number of pixels separating the central spot and each of the first order interference peaks (corresponding to the six different wavelengths) are recorded. As the size of the spheres is known, the relationship between λ_i and L_i for i =1,2...6 can be determined using the Bragg relation. Using the fact that only odd harmonics are generated and that the value of L should be identical for each wavelength allows both the set of generated wavelengths and the real value of L to be determined. By calculating each combination of odd harmonics, a different value for L will emerge. However, the variation in L will be minimised for the correct set of wavelengths. This occurs for the 23rd, 25th, 27th, 29th, 31st and 33rd harmonic of 800 nm. L is calculated using this minimisation method to be 17.7 $\pm$ 0.2 mm, and was measured by eye to be 17 mm.

Secondly, the width of the interference peaks can be calculated using the

Scherrer equation [104],

$$B = \frac{\lambda}{tcos(\theta)} \tag{5.11}$$

where B is the half-width half-maximum of the interference peak, t is the width of the crystal and θ is the angle of the interference peak in relation to the incident beam. As the diffraction pattern in figure 5.6 has six-fold symmetry and hence is from a single crystallite, the size of the crystallite is equivalent to the size of the XUV focus. Calculations show that the interference peaks at the angles of 0.16, 0.27 and 0.33 radians are 11% smaller, 3% smaller and 3% larger than the size of a CCD pixel at that angle. This implies that each non-convoluted interference peak is similarly sized to a single pixel.

The intensity of the most intense pixel within each convoluted interference peak was recorded. This provided the intensity for a defined wavelength and angle. This technique was repeated for the three most intense wavelengths, and for each of the three diffraction orders observed. This provided data points at non-zero angles. The intensity in the central spot was summed, and this intensity was split into the different wavelengths in their relative strengths, using the spectrum extracted from the diffraction pattern itself (see figure 3.4). This provided the intensity for each wavelength at zero degrees and allowed the experimental data to be normalised for comparison with theoretical calculations.

5.5 Determination of XUV Dielectric Constant

For each wavelength there exists 19 data points; 1 at zero radians, and six at each of the three angles at ∼0.16, ∼0.27 and ∼0.33 radians. These data

points are then fitted to the Mie scattering calculations using a nonlinear least-squares minimisation routine, from the MATLAB function library.

A function was written that takes as arguments the wavelength, the values of δ and β and the size of the spheres and returns a Mie scattering curve. The values of δ and β are the parameters that are used to minimise the error between the experimental and theoretical results. The measurement error in the size of the spheres is included in the routine.

Figure 5.7 shows the experimental data set and the error minimised curve for 27.6 nm, along with the curves corresponding to the tabulated values given by [65] and [101].

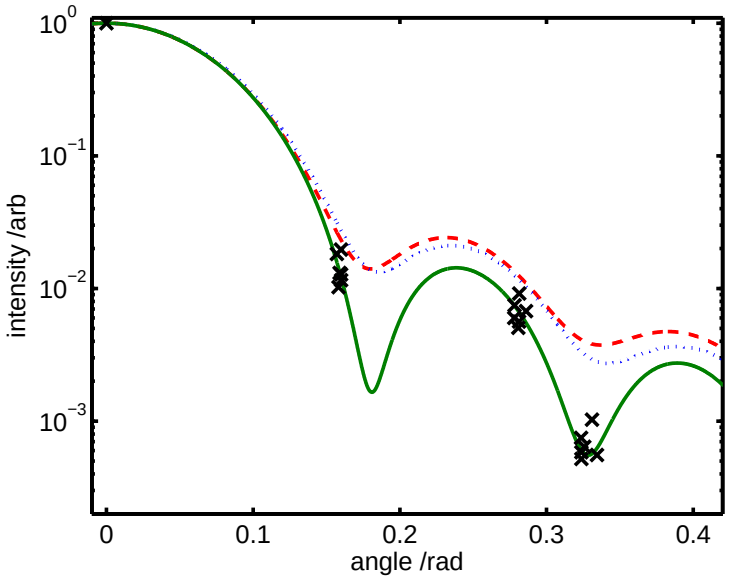

Figure 5.7: *Experimental data (crosses) and Mie scattering curve (solid line) corresponding to the experimentally determined values for the refractive index of polystyrene. Also plotted are the distributions corresponding to the tabulated values from [65] (dashed) and [101] (dotted).*

The least-squares fit gives the optimal value for δ and β together with 95% confidence intervals. These are illustrated by the error bars on figure 5.8. Within the fitting process the data is weighted according to a Pois-

son counting error, and therefore the lowest intensity values have a lower weighting.

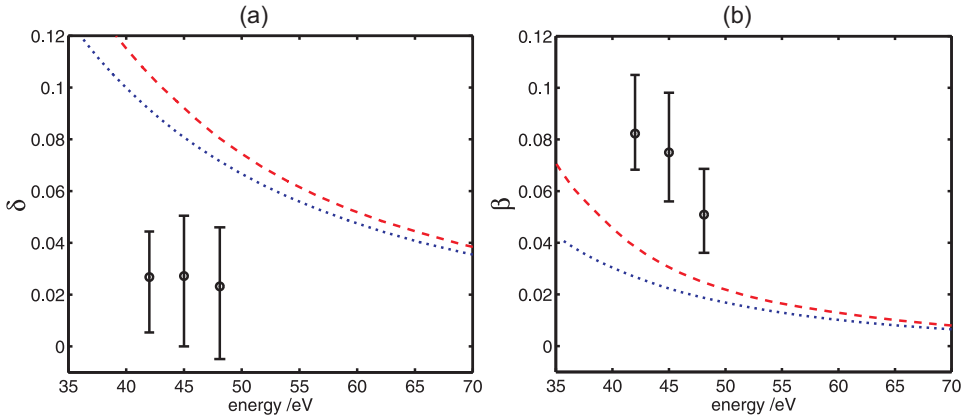

Figure 5.8: *The a) real and b) imaginary parts of the refractive index for polystyrene, showing the experimentally determined results (black, with 95% confidence levels) together with tabulated data from [65] (dashed) and [101] (dotted).*

The experimentally observed trend for β matches with the tabulated databases. However, the value of β has been measured to be roughly double the predicted value. Both the value and trend of δ are predicted incorrectly. The considerable difference between experimental results and the databases is expected for many elements in the XUV spectral region, due to the extremely sparse existing experimental measurements and the presence of absorption edges. To predict the refractive index of a molecule, these measurements are then used in the non-interacting atom approximation, which simply combines the refractive index of the constituent elements and ignores the interaction between the atoms. It is clear that the susceptibility of many elements, especially hydrogen, will change when the atom is bonded within a molecule. Therefore, it is not surprising that the experimental results presented in this chapter do not agree with the tabulated databases.

5.6 Application to other Diameters

The average diameter of the spheres used for the experiment described in this section was measured to be 196 ± 1.2 nm. Figure 5.9 shows the theoretical diffraction result from a hexagonal array of 50, 100, 200, 500 and 1000 nm diameter polystyrene spheres when illuminated by 27.6 nm light. The experimentally measured refractive index is used here. Similar to previous figures, both the Mie scattering curve and the position (and hence the intensity) of the interference peaks are shown. The vertical dotted line shows the angular acceptance of the CCD when the camera is placed as close as possible to the sample. This is an experimental limitation unique to the camera used in this thesis and corresponds to a distance of 17 mm.

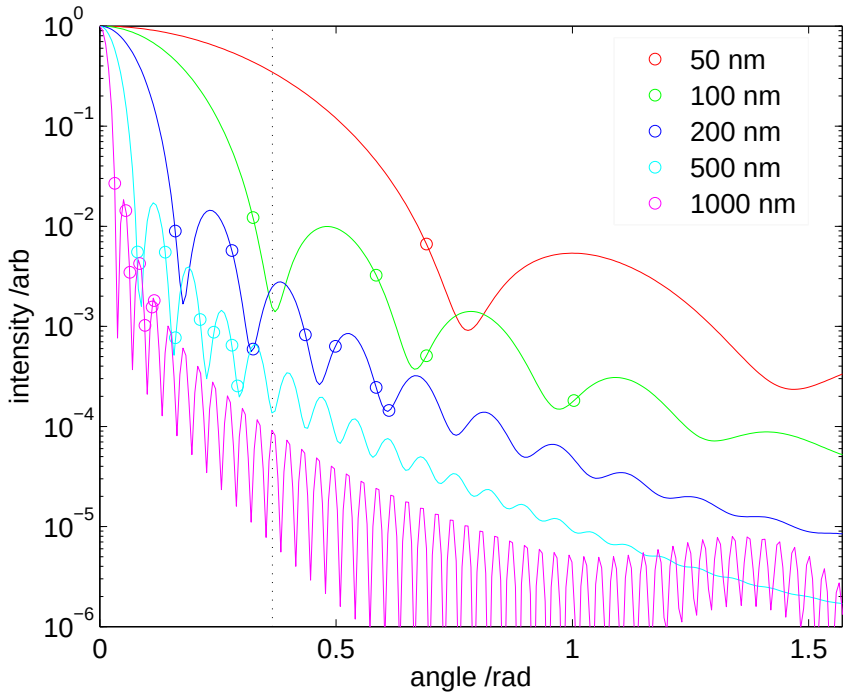

Figure 5.9: *Theoretical diffraction peaks from a hexagonal array of polystyrene nanospheres of different diameters. The circles represent the position and hence the intensity of interference peaks for 27.6 nm light. The theoretical curves are all normalised to unity.*

Figure 5.9 shows that in order to observe three diffraction orders a sphere diameter greater than or equal to approximately 200 nm must be used. A hexagonal array of 100 nm diameter spheres would only produce a single observable diffraction peak and hence would not enable the refractive index to be accurately determined, as the number of data points would not be higher than the number of variables. A unique solution may therefore not be possible. To solve this problem, an XUV detector without the described limitation could be used.

5.7 Application to other Materials

The technique demonstrated in this chapter enables the determination of the refractive index of polystyrene in the range 25 to 30 nm. This section shows that the technique can be used to accurately determine the refractive index of almost any material in the XUV wavelength range, if the material can be formed into spheres. However, it is important to realise that the way in which light is scattered from any object is dependent on its shape and therefore any object that is similar in size to the wavelength could potentially be used.

An equation that is a function of two variables can always be best-fitted to a set of data points, giving a value for each of the variables. However, the variables can only be determined accurately if there is little correlation between them. In other words, the partial differential with respect to one variable must be different to the partial differential with respect to the other. As shown in this section, the values for δ and β can be extracted accurately from just four data points, as the way in which they affect the Mie calculation is in general significantly different.

Figure 5.10 shows the effect on the scattering curve when the real and

imaginary components of the refractive index are changed independently. In part a) the real part of the refractive index is changed whilst the imaginary part is held constant. In part b) the real part is held constant whilst the imaginary part is changed. In both cases the red line corresponds to a decrease in either the real or imaginary part by a factor of 25%, whilst the blue line corresponds to an increase of 25%. The green line is the experimentally observed value and is therefore identical in both parts of the figure. Of interest is that a) exhibits strong variation only for the third angle, whilst b) only for the first angle. The two components, δ and β, therefore affect the scattering curve in significantly different ways and this enables the refractive index to be accurately extracted.

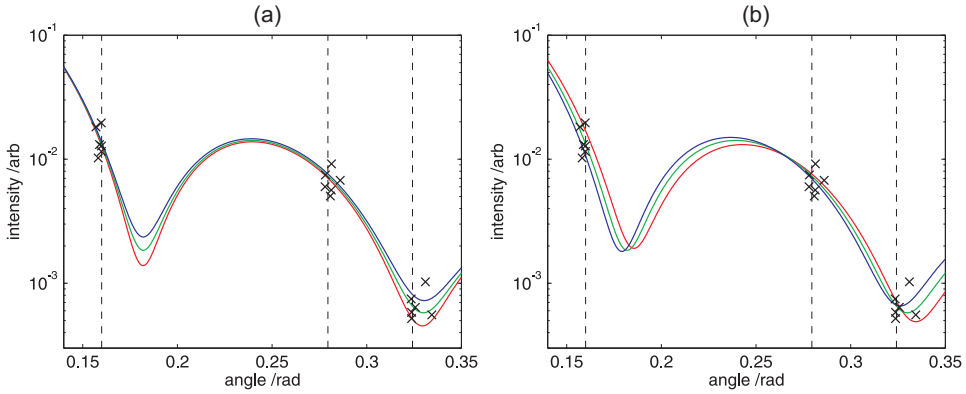

Figure 5.10: *The effect on the scattering curve whilst a) changing the real part of the refractive index and holding the imaginary part constant and b) vice-versa. The red lines correspond to a decrease of 25% and the blue line an increase of 25%. The green line is the experimentally determined value. Of interest is that a) exhibits strong variation only for the third angle, whilst b) only for the first angle.*

Figures 5.11 and 5.12 show this effect in more detail for the first and third angles in figure 5.10. In both cases a) corresponds to only changing the real component and b) only changing the imaginary component.

There are several companies that sell nanospheres made from plastic and from some metals. Coating polystyrene spheres with a metal is also

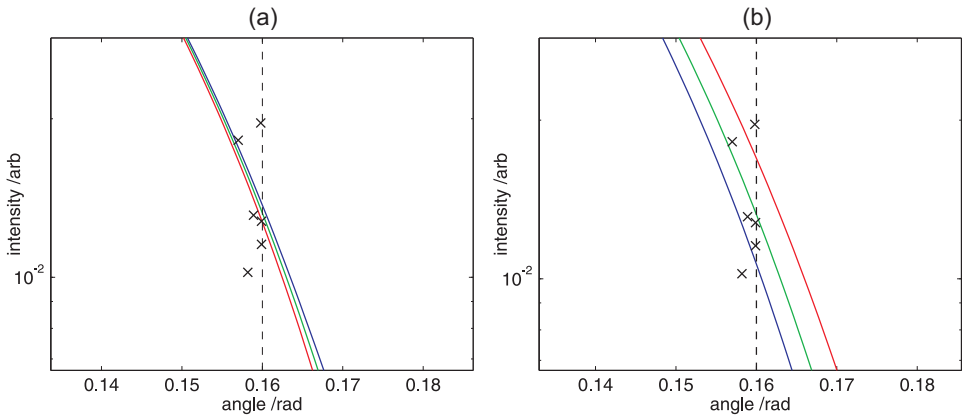

Figure 5.11: *The effect on the theoretical curve at the* first *angle when the a) real and b) imaginary components are changed by a factor of 25%. This is equivalent to figure 5.10 for a specific angle range. The scattering curve at this angle is not sensitive to small changes in the real component, but very sensitive to changes in the imaginary component.*

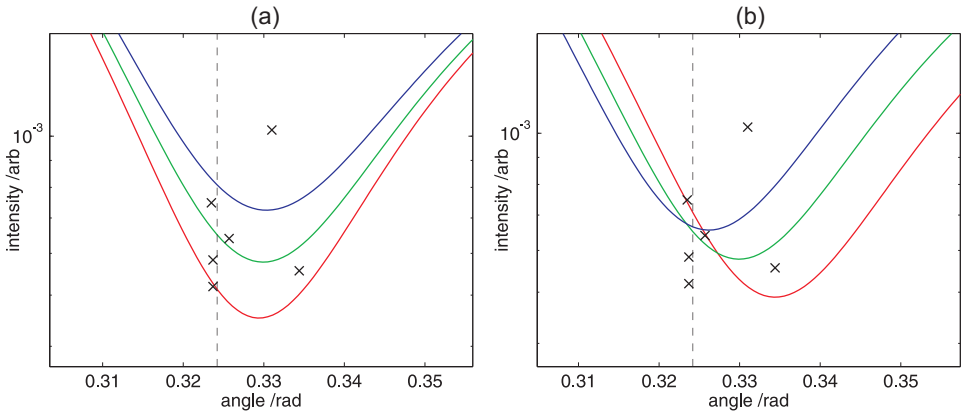

Figure 5.12: *The effect on the theoretical curve at the* third *angle when the a) real and b) imaginary components are changed by a factor of 25%. This is equivalent to figure 5.10 for a specific angle range. The scattering curve at this angle is sensitive to small changes in the real component, but insensitive to the imaginary component due to the crossing point in the function.*

feasible as the Mie solution can be easily extended to coated spheres. Future innovations, driven by experimental requirements, are likely to allow the fabrication of nanospheres from other materials. The generality of this technique is therefore of interest.

By simulating the experimental data points for a hexagonal array of 196 nm diameter spheres for each combination of real and imaginary refractive index components in the range $0 < \delta < 0.3$ and $0 < \beta < 0.3$, and simulating the effect of a small change in each of the values for δ and β, a relative value is given for the extraction accuracy for each refractive index for 27.6 nm light. All other factors aside, each refractive index accuracy value higher than that calculated for polystyrene must therefore lead to a more accurate result. The outcome of this simulation is normalised by setting the accuracy value for the refractive index of polystyrene to a value of unity. Figure 5.13 shows the simulated result displayed on a logarithmic color scale, where for example a value of one represents an accuracy ten times that observed for polystyrene. Several important materials are overlaid on the figure to give an idea of the variety present in the XUV spectral region. The experimentally determined value of polystyrene is shown in yellow. The orange region contains organic compounds, and the red values correspond to inorganic materials. The orange and red values are taken from [65]. However, as shown in this chapter, these values are known to have large errors and therefore only indicate the approximate refractive index value for each material.

Figure 5.13 explicitly demonstrates the generality of this technique for other materials. This generality is a direct consequence of the different effect of δ and β on the way XUV is scattered by a nanosphere. Interestingly, the accuracy for polystyrene represents an unusually low value. If this technique was repeated for another material, it is likely that the refractive index would

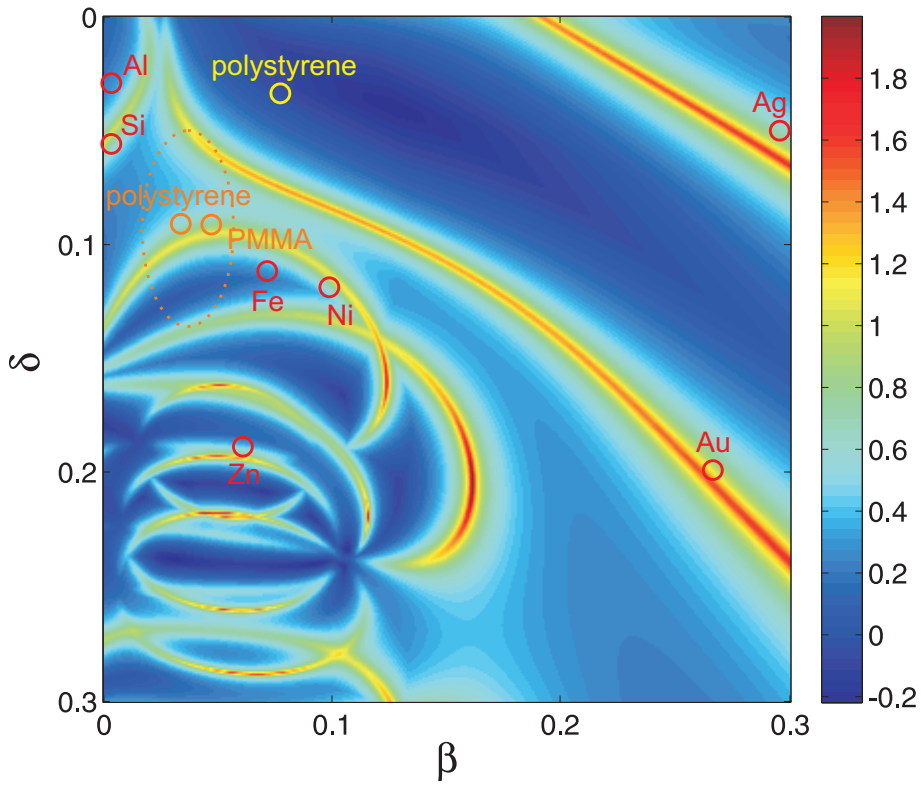

Figure 5.13: *The predicted relative experimental accuracy in obtaining the refractive index of a material, using the technique described in this chapter. The accuracy value for the refractive index value for polystyrene (yellow), determined in this chapter, is set to a value of one. As the color scale is logarithmic, the value for polystyrene on the colorbar is therefore zero. A colorbar value of one therefore indicates an experimental accuracy that is ten times better than the experimental results in this chapter. Several organic (orange) and inorganic (red) refractive indices, taken from [65], are also shown to illustrate the variety of refractive indices for 27.6 nm light.*

be measured with a higher accuracy. It is important to realise that this figure corresponds to 27.6 nm light and 196 nm diameter spheres. Simulations have shown that the size of the spheres strongly determines the accuracy result, and hence if a high accuracy is required, the size of the spheres could be optimised for a particular wavelength.

5.8 Determination of the Structure and Defects

XUV diffraction can be used to quantify defects in a crystal. The diffraction results presented in this chapter so far are from illumination of a single crystallite. However, regions were found on the sample that contained grain boundaries. Figure 5.14 compares the far-field diffraction images from a) a single crystallite, and b) a grain boundary. When the boundary is illuminated, two sets of rotated hexagonal interference peaks are observed.

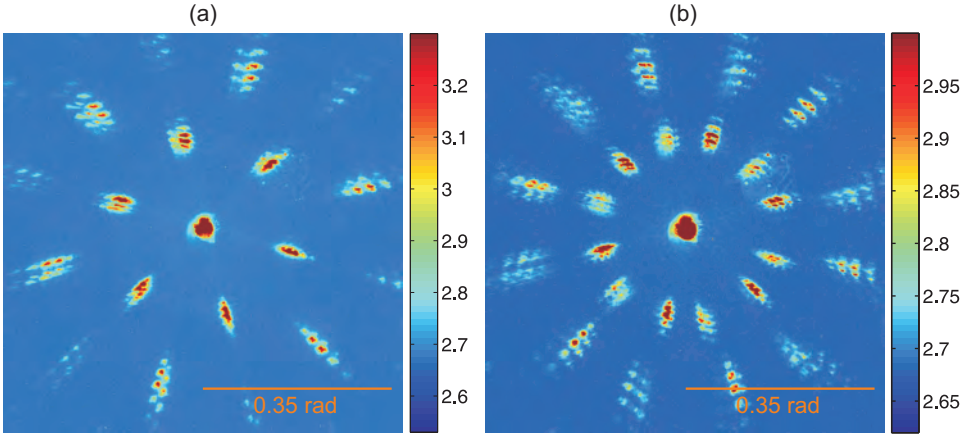

Figure 5.14: *XUV far-field diffraction images from a) a single crystallite and b) a grain boundary.*

Part b) contains useful information on the nature of the boundary. For example, the relative intensities of the interference peaks can be used to determine the number of spheres in each of the two crystallites, and the angle between the interference peaks can be used to calculate the relative

angles of the two sets of lattices.

As discussed in section 4.4, coherent diffractive imaging enables a sample to be determined using only its diffraction pattern. It is ideal for imaging aperiodic objects, as the measured diffraction pattern is continuous and hence there is a large set of non-zero data points. However, destructive interference effects, caused by multiple scatterers in a periodic sample, can result in a very small amount of information measured on a detector. The error in the reconstructed sample when using a diffraction pattern with discrete interference peaks is therefore generally large. Figure 5.15 shows the reconstructed sample, where part a) shows the whole sample, and part b) a small region. Illustrated on part b) are the reconstructed lattice planes. For this analysis, the diffraction image in figure 5.14a) has been used.

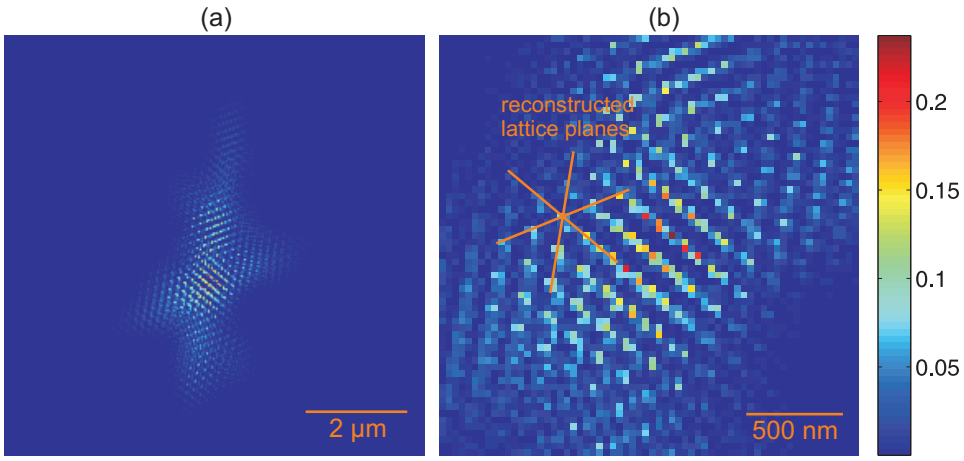

Figure 5.15: *Coherent diffractive imaging solution for the experimental diffraction pattern in figure 5.14a), showing a) the entire sample, and b) a close up of the reconstructed lattice planes. The distance scale is calculated from figure 4.10.*

The coherent diffractive imaging algorithm produces a sample that has hexagonal lattices with a peak to peak separation of between five and six pixels, corresponding to a sphere diameter of between 182 and 218 nm. However, the reconstructed sample bears little other resemblance to the

physical sample. Firstly, the algorithm converges on a solution that has a distinctly different shape each time. Secondly, the number of reconstructed spheres is several orders of magnitude smaller than the correct value. Finally, when reconstructing the sample corresponding to the diffraction pattern in figure 5.14b), a single hexagonal lattice is determined.

Although coherent diffractive imaging is a useful method of imaging an aperiodic sample, the information that can be gained from a periodic sample is limited. However, the reconstructed solution is considerably better than a simple inverse Fourier transform and therefore may still be of some use. Further study is needed to understand the level of periodicity at which the coherent diffractive imaging technique no longer provides an accurate representation of the sample.

5.9 Conclusion

Presented in this chapter is a technique for simultaneously measuring the structure and XUV dielectric constant across several wavelengths for a nanoscale object. All that is required is a single diffraction image, shown to be obtainable within a few minutes. The experimentally measured complex refractive index for polystyrene is presented. A significant discrepancy was shown between the experimental results and existing tabulated values. However, this is not surprising given the limited available data and its significant associated errors that is used in order to obtain these values.

The generality of this technique has been demonstrated. Assuming that a sphere of a given material can be made, this technique will allow the determination of its refractive index. In fact, it is likely that a higher accuracy than the result presented here will be achieved. A significant improvement in the accuracy will also be made if the observed interference peak split-

ting, shown to be a result of small imperfections in the mirror surface, is prevented.

Light that is diffracted from any object contains information on the refractive index of the object. This technique is therefore not limited to diffraction from spherical objects, but is applicable to many other structures.

Chapter 6

Conclusions and Future Work

This thesis has described the development of a High Harmonic Generation radiation source for extreme ultraviolet (XUV) diffractive imaging at the University of Southampton. The following paragraphs summarise the important contributions that I have made during this PhD and the steps that are now required to progress the group towards its objective of single molecule scattering.

Two focussing techniques have been demonstrated: a spherical multilayer mirror and a hollow fiber with a parabolic profile. The multilayer mirror was shown to produce an astigmatic focus and decrease the XUV beam quality. By simulating small surface deviations, both the experimentally observed increase in M^2 and the diffraction peak splitting was explained. The hollow fiber produced a smaller focus but, due to multiple reflections, the resultant focus comprised of ring-like structures. Currently, the intensity at the focus is limited by the quality of the two available optics and therefore a more effective focussing optic is now required.

The successful coherent diffractive imaging of a micron-sized aperiodic sample from an XUV diffraction pattern has been demonstrated. By monochromating the source, the imaging resolution is expected to become ∼50 nm. Fabrication of a tobacco mosaic virus sample is currently being undertaken by group member Chapman, with the aim of imaging a biological sample. This will be a significant step towards the objective of the project.

A technique for measuring the refractive index of a material at multiple wavelengths from a single diffraction image was presented. By measuring the XUV diffraction pattern from a hexagonal array of polystyrene nanospheres, the refractive index of polystyrene was determined for three wavelengths in the range 25 to 30 nm. The experimental results were shown to disagree with the theoretical values. The crystal structure and defects can be quantified from the same diffraction image, making this method a simultaneous imaging and spectroscopic technique.

The objective of this thesis was to develop and optimise the HHG source and work towards the ultimate goal of single-shot, single molecule imaging. The tasks were therefore to increase the XUV flux and develop the experimental system to be capable of coherent diffractive imaging. The XUV flux has been increased by three orders of magnitude, two focussing setups have been tested and a micron-sized object has been successfully imaged.

Whilst substantial progress has been made during this thesis, it is clear that the objective of single-shot single molecule imaging requires considerably more research. This should centre on the further increase of flux, the increase in the energy of the generated photons and the development of a system capable of delivering biological materials into the path of the XUV beam. Recent advances in commercial table-top laser amplification systems [105] will enable further increases in XUV flux, and laser pulse

compression techniques [106, 107] will enable higher XUV energies. In addition, electrospray [108] systems are showing promise for the delivery of small samples into the path of a pulsed X-ray beam [109].

Whilst the technology may be a decade away, the scientific advances that will result from the routine imaging of large biological proteins and viruses in a laboratory environment will perhaps be as revolutionary as the discovery of X-rays 100 years ago.

Appendix A

Mie Scattering Derivation

Presented here is a summary of the derivation for the interaction of light with a spherical object. This work follows the derivation given by Bohren and Huffman [110].

To determine the light that is scattered by a spherical object, the four equations, A.1, A.2, A.5 and A.6 are required, where π_n and τ_n are the angle dependent functions, and a_n and b_n are the scattering coefficients. The angle dependent functions for a specific angle θ, are defined as,

$$\pi_n = \frac{P_n^1}{sin\theta} \tag{A.1}$$

$$\tau_n = \frac{P_n^1}{d\theta} \tag{A.2}$$

where P_n^m is the associated Legendre function of the first kind of degree n and order m. They can be solved using the relations,

$$\pi_n = \frac{2n-1}{n-1}(\cos\theta)\pi_{n-1} - \frac{n}{n-1}\pi_{n-2} \tag{A.3}$$

$$\tau_n = n(\cos\theta)\pi_n - (n+1)\pi_{n-1} \tag{A.4}$$

where the fact that $\pi_0 = 0$ and $\pi_1 = 1$ is used to complete the upwards recurrence relation.

The scattering coefficients are defined as the following,

$$a_n = \frac{m\psi_n(mx)\psi_n'(x) - \psi_n(x)\psi_n'(mx)}{m\psi_n(mx)\xi_n'(x) - \xi_n(x)\psi_n'(mx)} \tag{A.5}$$

$$b_n = \frac{\psi_n(mx)\psi_n'(x) - m\psi_n(x)\psi_n'(mx)}{\psi_n(mx)\xi_n'(x) - m\xi_n(x)\psi_n'(mx)} \tag{A.6}$$

where the prime indicates differentiation with respect to the argument in the brackets.

To solve for the scattering coefficients, the equations A.7, A.8, A.9 and A.10 are used.

The size parameter x, and relative refractive index m are defined as,

$$x = \frac{2\pi N a}{\lambda} \tag{A.7}$$

$$m = \frac{N_1}{N} \tag{A.8}$$

where a, λ, N and N_1 which are the radius of the sphere, the wavelength of incident light, and the refractive index of the medium and particle.

The functions $\psi_n(\rho)$ and $\xi_n(\rho)$ are defined as,

$$\psi_n(\rho) = \rho j_n(\rho) \tag{A.9}$$

$$\xi_n(\rho) = \rho h_n^{(1)}(\rho) \tag{A.10}$$

where $j_n(\rho)$ and $h_n^{(1)}(\rho)$ are the spherical Bessel and Hankel functions.

This provides us with the scattering and extinction cross sections,

$$C_{sca} = \frac{2\pi}{k^2}\sum_{n=1}^{\infty}(2n+1)(|a_n|^2 + |b_n|^2) \tag{A.11}$$

$$C_{ext} = \frac{2\pi}{k^2}\sum_{n=1}^{\infty}(2n+1)\Re\{a_n + b_n\} \tag{A.12}$$

where $k = 2\pi/\lambda$ is the wavevector.

Also required are the matrix components for the transverse components of the scattered electric field, as defined by,

$$S_1 = \sum_n \frac{2n+1}{n(n+1)}(a_n\pi_n + b_n\tau_n) \tag{A.13}$$

$$S_2 = \sum_n \frac{2n+1}{n(n+1)}(a_n\tau_n + b_n\pi_n) \tag{A.14}$$

where $|S_1|^2$ is the scattered irradiance per unit incident irradiance given that the incident light is polarised perpendicular to the scattering plane, and $|S_2|^2$ corresponds to light that is polarised parallel to the scattering plane. It is important to note that π_n and τ_n are for a specific angle, and hence $|S_1|^2$ and $|S_2|^2$ must be calculated for each required angle.

In order to improve the computation time, equations A.5 and A.6 can be simplified to,

$$a_n = \frac{[D_n(mx)/m + n/x]\psi_n(x) - \psi_{n-1}(x)}{[D_n(mx)/m + n/x]\xi_n(x) - \xi_{n-1}(x)} \tag{A.15}$$

$$b_n = \frac{[mD_n(mx) + n/x]\psi_n(x) - \psi_{n-1}(x)}{[mD_n(mx) + n/x]\xi_n(x) - \xi_{n-1}(x)} \tag{A.16}$$

where D_n is the logarithmic derivative,

$$D_n(\rho) = \frac{d}{d\rho} \ln \psi_n(\rho) \tag{A.17}$$

which can be solved using the downwards recursion relation,

$$D_{n-1}(\rho) = \frac{n}{\rho} - \frac{1}{D_n + n/\rho} \tag{A.18}$$

Bibliography

[1] J. D. Watson and F. H. C Crick. Molecular structure of nucleic acids. *Nature*, 171, 1953.

[2] T. Remetter, J. Johnsson, P. Mauritsson, K. Varju, Y. Ni, F. Lepine, E. Gustafsson, M. Kling, J. Khan, R. Lopez-Martens, K. J. Schaffer, M. J. Vrakking, and A. L'Huillier. Attosecond electron wave packet interferometry. *Nature Physics*, 2:323–326, 2006.

[3] A. S. Moffat. Opening the door to more membrane protein structures. *Science*, 277(5332):1607–1608, 1997.

[4] M. L. Pusey, Liu Z-H, W. Tempel, J. Praissman, D. Lin, B-C. Wang, J.A. Gavira, and Ng J.D. Life in the fast lane for protein crystallization and x-ray crystallography. *Progress in Biophysics and Molecular Biology*, 88:359–386, 2005.

[5] R. Neutze, R. Wouts, D. van der Spoel, E. Weckert, and J. Hajdu. Potential for biomolecular imaging with femtosecond x-ray pulses. *Nature*, (6797):752–759, 2000.

[6] A. Barty, S. Boutet, M. J. Bogan, S. Hau-Riege, K. Marchesini, S. Sokolowski-Tinten, N. Stojanovic, R. Tobey, H. Ehrke, A. Cavlleri, S. Dustere, M. Frank, S. Bajt, B. W. Woods, M. M. Seibert, J. Hadju,

R. Treusch, and H. N. Chapman. Ultrafast single-shot diffraction imaging of nanoscale dynamics. *Nature Photonics*, 2:415–419, 2008.

[7] J. R. Fienup. Phase retrieval algorithms - a comparison. *Applied Optics*, 21(15):2758–2769, 1982.

[8] H. N. Chapman, A. Barty, M. J. Bogan, S. Boutet, M. Frank, S. P. Hau-Riege, S. Marchesini, B. W. Woods, S. Bajt, H. Benner, R. A. London, E. Plonjes, M. Kuhlmann, R. Treusch, S. Dusterer, T. Tschentscher, J. R. Schneider, E. Spiller, T. Moller, C. Bostedt, M. Hoener, D. A. Shapiro, K. O. Hodgson, D. Van der Spoel, F. Burmeister, M. Bergh, C. Caleman, G. Huldt, M. M. Seibert, Frnc Maia, R. W. Lee, A. Szoke, N. Timneanu, and J. Hajdu. Femtosecond diffractive imaging with a soft x-ray free-electron laser. *Nature Physics*, 2(12):839–843, 2006.

[9] D. L. Matthews, P. L. Hagelstein, M. D. Rosen, M. J. Eckart, N. M. Ceglio, A. U. Hazi, H. Medecki, B. J. McGowan, J. E. Trebes, B. L. Whitten, E. M. Cambell, and C. W. Hatcher. Demonstration of a soft x-ray amplifier. *Physical Review Letters*, 54(2):110–113, 1985.

[10] J. J. Rocca, V. Shlyaptsev, F. G. Tomasel, O. D. Cortazar, D. Hartshorn, and J. L. Chilla. Demonstration of a discharge pumped table-top soft x-ray laser. *Physical Review Letters*, 73(16):2192–2195, 1994.

[11] R. L. Sandberg, C. Song, P. W. Wachulak, D. A. Raymondson, B. Amirbekian, E. Lee, A. E. Sakdinawat, C. La-O-Vorakiat, M. C. Marconi, C. S. Menoni, M. M. Murnane, J. J. Rocca, H. C. Kapteyne,

and J. Miao. High numerical aperture tabletop soft x-ray diffraction microscopy with 70-nm resolution. *PNAS*, 105(1):24–27, 2008.

[12] M. Pioletti, F. Schlunzen, J. Harm, R. Zarivach, M. Gluhmann, H. Avila, H. Auerbach T. Bashan, A. Bartels, T. Jacobi, C. Hartsch, A. Yonath, and Franceschi. F. Crystal strcutures of complexes of the small ribosomal subunit with tetracycline, edeine and if3. *The EMBO Journal*, 20(8):1829–1839, 2001.

[13] J. M Grimes, J. N. Burroughs, P. Gouet, J. M. Diprose, R. Malby, S. Zientara, P. C. Mertens, and D. I. Stuart. The atomic structure of the bluetongue virus core. *Nature*, 395:470–478, 1998.

[14] F. Schotte, M. H. Lim, T. A. Jackson, A. V. Smirnov, J. Soman, J. S. Olson, G. N. Phillips, M. Wulff, and P. A. Anfinrud. Watching a protein as it functions with 150-ps time-resolved x-ray crystallography. *Science*, 300(5627):1944–1947, 2003.

[15] H. F. Poulsen, S. F. Nielsen, E. M. Lauridsen, S. Schmidt, R. M. Suter, U. Lienert, L. Margulies, T. Lorentzen, and D. J. Jenson. Three-dimensional maps of grain boundaries and the stress state of individual grains in polycrystals and powders. *Applied Crystallography*, 34:751–756, 2001.

[16] A. Filipponi, M. Borowski, D. T. Bowren, S. Ansell, A. D. Cicco, S. D. Panfilis, and J-P. Itie. An experimental station for advanced research on condensed matter under extreme conditions at the european synchrotron radiaton facility - bm29 beamline. *Review of Scientific Intstrumenents*, 71(6):2422–2432, 2000.

[17] K. Xia, U. L. Skyllberg, W. F. Bleam, P. R. Bloom, E. A. Nater, and P. A. Helmke. X-ray absorption spectroscopic evidence for the complexation of hg(ii) by reduced sulfur in soil humic substances. *Environ. Sci. Technol.*, 33:527–261, 1999.

[18] Diamond light source, July 2009. `http://www.diamond.ac.uk/`.

[19] D. H. Bilderback, P. Elleaumme, and E. Weckert. Review of third and next generation synchrotron light sources. *J. Phys. B*, 38:773–797, 2005.

[20] R. W. Schoenlein, S. Chattopadhyay, H. H. W. Chong, T. E. Glover, P. A. Heimann, C. V. Shank, A. A. Zholents, and M. S. Zolotorev. Generation of femtosecond pulses of synchrotron radiation. *Science*, 287:2237–2240, 2000.

[21] V. et al Ayvazyan. First operation of a free-electron laser generating gw power radiation at 32 nm wavelength. *European Physical Journal D*, 37:297–303, 2006.

[22] Flash: The free-electron laser in hamburg. Technical report, DESY, 2007.

[23] H. N. Chapman. X-ray imaging beyond the limits. *Nature Materials*, 8:299–301, 2009.

[24] M. Lewenstein, P. Balcou, M. Y. Ivanov, and A. LHuillier. Theory of high-harmonic generation by low-frequency laser fields. *Physical Review*, 49(3):2117, 1994.

[25] P. B Corkum. Plasma perpective on strong field muliphoton ionisation. *Phys. rev.*, 71(13):1994–1997, 1993.

[26] R. A. Bartels, A. Paul, M. M. Murnane, H. C. Kapteyn, S. Backus, Y. Liu, and D. T. Attwood. Absolute determination of the wavelength and spectrum of an extreme-ultraviolet beam by a young's double-slit measurement. *Optics Letters*, 27(9):707–709, 2002.

[27] E. A. Gibson, A. Paul, N. Wagner, R. Tobey, S. Backus, I. P. Christov, M. M. Murnane, and H. C. Kapteyn. High-order harmonic generation up to 250 ev from highly ionized argon. *Physical Review Letters*, 92 (3), 2004.

[28] C. A. Froud, E. T. F. Rogers, D. C. Hanna, W. S. Brocklesby, M. Praeger, A. M. de Paula, J. J. Baumberg, and J. G. Frey. Soft x-ray wavelength shift induced by ionization effects in a capillary. *Optics Letters*, 31(3):374–376, 2006.

[29] R. Bartels, S. Backus, E. Zeek, L. Misoguti, G. Vdovin, I. P. Christov, M. M. Murnane, and H. C. Kapteyn. Shaped-pulse optimization of coherent emission of high-harmonic soft x-rays. *Nature*, (6792):164–165, 2000.

[30] P. Lan, P. Lu, Q. Li, W. Hong, and Q. Zhang. Macroscopic effects for quantum control of broadband isolated attosecond pulse generation with a two-color field. *Physical Review A*, 79:043413, 2009.

[31] D. I. Svergun. Restoring low resolution structure of biological macromolecules from solution scattering using simulated annealing. *Biophys. J.*, 76(6):2879–2886, 1999.

[32] A. Ravasio, D. Gauthier, F. Maia, M. Billon, J. Caumes, D. Garzella, M. Geleoc, O. Gobert, J. Hergott, A. Pena, H. Perez, B. Carre, E. Bourhis, J. Gierak, A. Madouri, D. Mailly, B. Schiedt, M. Fa-

jardo, J. Gautier, P. Zeitoun, P. Bucksbaum, J. Hadju, and H. Merdji. Single-shot diffractive imaging with a table-top femtosecond soft x-ray laser-harmonics source. *Physical Review Letters*, 103:028104, 2009.

[33] U. Morgner, F. X. Kartner, S. H. Cho, Y. Chen, H. A. Haus, J. G. Fujimoto, and E. P. Ippen. Sub-two-cycle pulses from a kerr-lens mode-locked ti:sapphire laser. *Optics Letters*, 24(6):411–413, 1999.

[34] T. Brabec, Ch. Spielmann, P.F. Curley, and F. Krausz. Kerr lens mode locking. *Optics Letters*, 17(18):1292–1294, 1992.

[35] M. Aoyama, Y. Yamakawa, Y. Akahane, J. Ma, N. Inoue, H. Ueda, and H. Kiriyama. 0.85-pw, 33-fs ti:sapphire laser. *Optics Letters*, 28 (17):1594–1596, 2003.

[36] J. Zhou, G. Taft, C-P. Huang, M. M. Murnane, H. C. Kapteyn, and I. P. Christov. Pulse evolution in a broad-bandwidth ti:sapphire laser. *Optics Letters*, 19(15):1149–1151, 1994.

[37] A. E. Siegman. How to (maybe) measure laser beam quality. Optical Society of America Annual Meeting, Long Beach, California, 1997.

[38] R. Trebino. *Frequency-resolved optical gating: the measurement of ultrashort laser pulses*. Springer,, first edition, 2002.

[39] P. O'Shea, M. Kimmel, X. Gu, and R. Trebino. Highly simplified device for ultrashort-pulse measurement. *Optics Letters*, 26:932–934, 2001.

[40] M. Ferray, A. LHuillier, X. F. Li, L. A. Lompre, G. Mainfray, and C. Manus. Multiple-harmonic conversion of 1064 nm radiation in rare gases. *Journal of Physics B: Atomic, Molecular and Optical Physics*, 21:31–35, 1988.

[41] K. C. Kulander and B. W. Shore. Calculations of multiple-harmonic conversion of 1064-nm radiation in xe. *Physical Review Letters*, 62(5): 524–526, 1989.

[42] C. Altucci, R. Velotta, J. P. Marangos, E. Heesel, E. Springate, M. Pascolini, L. Poletti, P. Villoresi, C. Vozzi, G. Sansone, M. Anscombe, J-P. Caumes, S. Stagira, and M. Nisoli. Dependence upon the molecular and atomic ground state of higher-order harmonic generation in the few-optical-cycle regime. *Physical Review A*, 71: 013409, 2005.

[43] S. L. Stebbings, E. T. F. Rogers, A. M. de Paula, M. Praegar, C. A. Froud, B. Mills, D. C. Hanna, J. J. Baumberg, W. S. Brocklesby, and J. G. Frey. Molecular variation of capillary-produced soft x-ray high harmonics. *J. Phys. B: At. Mol. Opt. Phys.*, 41:145602, 2008.

[44] P. M. Paul, E. S. Toma, P. Breger, G. Mullot, F. Auge, P. Balcou, H. G. Muller, and P. Agostini. Observation of a train of attosecond pulses from high harmonic generation. *Science*, (5522):1689–1691, 2001.

[45] P. B. Corkum, N. H. Burnett, and M. Y. Ivanov. Subfemtosecond pulses. *Optics Letters*, 19(22):1870–1872, 1994.

[46] D. Oron, Y. Silberberg, N. Dudovich, and D. M. Villeneuve. Efficient polarisation gating of high-order harmonic generation by polarisation-shaped ultrashort pulses. *Physical Review A*, 72:063816, 2006.

[47] C. G. Durfee, A. R. Rundquist, S. Backus, C. Herne, M. M. Murnane, and H. C. Kapteyn. Phase matching of high-order harmonics in hollow waveguides. *Physical Review Letters*, 83(11):2187–2190, 1999.

[48] E. Constant, D. Garzella, P. Breger, E. Mevel, Ch. Dorrer, C. Le Blanc, F. Salin, and P Agostini. Optimizing high harmonic generation in absorbing gases: Model and experiment. *Physical Review Letters*, 82(8):1668, 1999.

[49] M. Schnurer, Ch. Spielmann, P. Wobrauschek, C. Streli, N. H. Burnett, C. Kan, K. Ferencz, R. Koppitsch, Z. Cheng, T. Brabec, and F. Krausz. Coherent 0.5-kev x-ray emission from helium driven by a sub-10-fs laser. *Physical Review Letters*, 80(15):3236–3239, 1998.

[50] C. Altucci, R. Bruzzese, C. de Lisio, M. Nisoli, S. Stagira, De Silvestrim S., O. Svelto, A. Boscolo, P. Ceccherini, L. Poletto, G. Tondello, and P. Villoresi. Tunable soft x-ray radiation by high-order harmonic generation. *Physical Review A*, 61:021801, 1999.

[51] Z. H. Chang, A. Rundquist, H. W. Wang, I. Christov, M. M. Murnane, and H. C. Kapteyn. Generation of coherent, femtosecond, x-ray pulses in the "water window". *Ieee Journal of Selected Topics in Quantum Electronics*, 4(2):266–270, 1998.

[52] P. Salieres, P. Antoine, A. Bohan, and M. Lewenstein. Temporal and spectral tailoring of high-order harmonics. *Physical Review Letters*, 81 (25):5544–5547, 1998.

[53] P. B. Corkum and F. Krausz. Attosecond science. *Nature Physics*, 3: 381–387, 2007.

[54] B. Shan, A. Cavalieri, and Z. Chang. Tunable high harmonic generation with an optical parametric amplifier. *Applied Physics B*, 74 (S23-S26), 2002.

[55] A. Averchi, D. Faccio, R. Berlasso, M. Kolesik, J. V. Moloney, A. Couairon, and P. D. Trapani. Phase matching with pulsed bessel beams for high-order harmonic generation. *Physical Review A*, 77: 021802, 2008.

[56] E. T. F. Rogers. *Modelling of Capillary High Harmonic Generation*. PhD thesis, University of Southampton, 2008.

[57] P. Balcou, P. Salieres, A. L'Huillier, and M. Lewenstein. Generalized phase-matching conditions for high-harmonics: The role of field-gradient forces. *Physical Review A*, 55(4):3204–3210, 1997.

[58] F. Lindner, W. Stremme, M. G. Schatzel, F. Grasbon, G. G. Paulus, H. Walther, R. Hartmann, and L. Struder. High-order harmonic generation at a repetition rate of 100 khz. *Physical Review A*, 68:013814, 2003.

[59] M. Praeger, A. M. de Paula, C.A. Froud, E. T. F. Rogers, S. L. Stebbings, W. S. Brocklesby, J. J. Baumberg, D. C. Hanna, and J. G. Frey. Spatially resolved soft x-ray spectrometry from a single-image diffraction. *Nature Physics*, 3(3):176–179, 2007.

[60] H. J. Worner, H. Niikura, J. B. Bertrand, P. B. Corkum, and D. M. Villeneuve. Observation of electronic structure minima in high-harmonic generation. *Physics Review Letters*, 102:103901, 2009.

[61] F. Powell. Care and feeding of soft x-ray and extreme ultraviolet filters. In *Laser-induced Damage in Optical Materials*, volume 1848, pages 503–514. SPIE, 1992.

[62] W. Zhu, C. J. Hirchmugl, A. D. Laine, B. Sinkovic, and S. S. P. Parkin. Determination of the thickness of al oxide films used as barriers in

magnetic tunneling junctions. *Applied Physics Letters*, 78(20):3103–3105, 2001.

[63] R. W. Falcone. Dichroic beam splitter for extreme-ultraviolet and visible radiation. *Optics Letters*, 8(1):21–23, 1983.

[64] E. J. Takahashi, H. Hasegawa, Y. Nabekawa, and K. Midorikawa. High-throughput, high damage threshold broadband beam splitter for high-order harmonics in the extreme-ultraviolet region. *Optics Letters*, 29(5):507–509, 2004.

[65] B. L. Henke, E. M. Gullikson, and J. C. Davis. X-ray interactions - photoabsorption, scattering, transmission, and reflection at e=50-30,000 ev, z=1-92. *Atomic Data and Nuclear Data Tables*, 54(2):181–342, 1993.

[66] R. M. Azzam. Direct relation between fresnel's interface reflection coefficients for the parallel and perpendicular polarisations. *J. Opt. Soc. Am.*, 69(7):1007–1016, 1979.

[67] C. A. Froud. *Designing a Nanoscale Source: Towards Single Molecule X-Ray Scattering*. PhD thesis, University of Southampton, 2007.

[68] M. Praeger. *Development and Spatio-Spectral Mapping of a Capillary High Harmonic Source*. PhD thesis, University of Southampton, 2008.

[69] E. A. J. Marcatili and R. A. Schmeltzer. Hollow metallic and dielectric waveguides for long distance optical transmission and lasers. *Bell Systems Technical Journal*, 43:1783–1809, 1964.

[70] R. K. Nubling and J. A. Harrington. Launch conditions and mode coupling in hollow-glass waveguides. *Optical Engineering*, 37(9):2454–2458, 1998.

[71] J. Grant-Jacob. Gas density measurement using a jet-cell as a high-harmonic source. *Manuscript in preparation.*

[72] W. Chao, B. D. Harteneck, J. A. Liddle, E. H. Anderson, and D. T. Attwood. Soft x-ray microscopy at a spatial resolution better than 15 nm. *Nature*, 435:1210–1213, 2005.

[73] K. M. Skulina, C. S. Alford, R. M. Bionta, D. M. Makowiecki, E. M. Gullikson, R. Soufli, J. B. Kortright, and J. H. Underwood. Molybdenum/beryllium multilayer mirrors for normal incidence in the extreme ultraviolet. *Applied Optics*, 34(19):3727–3730, 1995.

[74] W. Lui, G. E. Ice, J. Z. Tischler, A. Khounsary, and A. T. Assoufid, L. Macrander. Short focal length kirkpatrick-baez mirrors for a hard x-ray nanoprobe. *Review of Scientific Instruments*, 76:113701, 2005.

[75] S. Matsuyama, H. Mimura, H. Yumoto, Y. Sano, K. Yamamura, M. Yabashi, Y. Nishino, K. Tamasaku, T. Ishikawa, and K. Yamauchi. Development of scanning x-ray flourescence microscope with spatial resolution of 30 nm using kirkpatrick baez mirror optics. *Review of Scientific Instruments*, 77:103102, 2006.

[76] M. Bargheer, N. Zhavoronkov, R. Bruch, H. Legall, H. Stiel, M. Woerner, and T. Elsaesser. Comparison of focusing optics for femtosecond x-ray diffraction. *Applied Physics B-Lasers and Optics*, 80(6):715–719, 2005.

[77] D.H. Bilderback. Review of capillary x-ray optics from the 2nd international capillary optics meeting. *X-ray Spectrometry*, 32:195–207, 2003.

[78] H. Mashiko, A. Suda, and K. Midorikawa. Focusing coherent soft x-ray radiation to a micrometer spot size withan intensity of 10(14) w/cm(2). *Optics Letters*, 29(16):1927–1929, 2004.

[79] E. A. Stern, Z. Kalman, A. Lewis, and K. Lieberman. Simple method for focusing x-rays using tapered capillaries. *Applied Optics*, 27(24): 5135–5139, 1988.

[80] D. H. Bilderback, S. A. Hoffman, and D. Thiel. Nanometer spatial resolution achieved in hard x-ray imaging and laue diffraction experiments. *Science*, 263:201–203, 1994.

[81] G. Yin, Y. Song, M. Tsang, F. Chen, S. Liang, K, F. W Deuwer, M. Feser, W. Yun, and H. D. Sheih. 30 nm resolution x-ray imaging at 8 kev using third order diffraction of a zone plate lens objective in a transmission microscope. *Applied Physics Letters*, 89:221122, 2006.

[82] J. J. Park, D. S. Kim, S. C. Jeon, J. Park, K. H. Lee, J. Lee, K. N. Kim, J. J. Yoo, and C. H. Nam. Table-top soft x-ray microscope adopting a pmma phase-reversal zone plate. CLEO/IQEC, 2009.

[83] S. Svelto. *Principles of Lasers.* Plenum Press, New York, fourth edition, 1998.

[84] V. S. Popov. Tunnel and multiphoton ionization of atoms and ions in a strong laser field (keldysh theory). *Physics-Uspekhi*, 47(9):855–885, 2004.

[85] O. K. Ersoy. *Fourier Optics and Imaging.* Wiley, 2007.

[86] Lebow company, July 2009. `http://www.lebowcompany.com/`.

[87] E. Hecht. *Optics*. Addison-Wesley, San Francisco, second edition, 1998.

[88] L. Vincze, K. Jansssens, and F. Adams. Interpretation of capillary generated spatial and angular distributions of x-rays. *Review of scientific instruments*, 69(10), 1998.

[89] T. A. Birks and Y. W. Li. The shape of fibre tapers. *Journal of Lightwave Technology*, 10(4):432–438, 1992.

[90] S. V. Kukhlevsky, F. Flora, A. Marinai, K. Negrea, L. Palladino, Reale A., G. Tomassetti, A. Ritucci, G. Nyitray, and L. Kozma. Diffraction of x-rays in capillary optics. *Applied Optics*, 39(6):1059–1063, 2000.

[91] M. Born and E. Wolf. *Principles of optics*. Cambridge University Press, seventh edition, 1999.

[92] P. P. Crooker, W. B. Colson, and J. Blau. Representation of a gaussian beam by rays. *American Journal of Physics*, 74(8):722–727, 2006.

[93] B. Mills, C. F. Chau, E. T. F. Rogers, J. Grant-Jacob, S. L. Stebbings, M. Praeger, A. M. de Paula, C. A. Froud, R. T. Chapman, T. J. Butcher, J. J. Baumberg, W. S. Brocklesby, and J. G. Frey. Direct measurement of the complex refractive index in the extreme ultraviolet spectral region using diffraction from a nanosphere array. *Applied Physics Letters*, 93:231103, 2008.

[94] R. L. Sandberg, A. Paul, D. A. Raymondson, S. Hadrich, D. M. Gaudiosi, J. Holtsnider, R. I. Tobey, O. Cohen, M. M. Murnane, and H. C. Kapteyne. Lensless diffractive imaging using tabletop coherent high-harmonic soft-x-ray beams. *Physical Review Letters*, 99:098103, 2007.

[95] B. Chen, R. A. Dilanian, S. Teichmann, B. Abbey, A. G. Peele, G. J. Williams, P. Hannaford, L. V. Dao, H. M. Quiney, and K. A. Nugent. Multiple wavelength diffractive imaging. *Physics Review A*, 79:023809, 2009.

[96] H. D. Tong, H. V. Jansen, V. J. Gadgil, C. G. Bostan, E. Berenschot, C. J. M. Rijn, and M. Elwenspoek. Silicon nitride nanosieve membrane. *Nano Letters*, 4(2):283–287, 2004.

[97] R. P. Millane. Phase retrieval in crystallography and optics. *Journal of the Optical Society of America A*, 7:394–411, 1990.

[98] S. Marchesini. Invited article: A unified evaluation of iterative projection algorithms for phase retrieval. *Review of Scientific Intruments*, 78:011301, 2007.

[99] S. Marchesini, H. N. Chapman, S. P. Hau-Riege, R. A. London, A. Szoke, H. He, M. R. Howells, H. Padmore, R. Rosen, J. C. H. Spence, and U. Weierstall. Coherent x-ray diffractive imaging: applications and limitations. *Optics Express*, 11(19):2344–2353, 2003.

[100] J. Miao, T. Ishikawa, E.H. Anderson, and K.O. Hodgson. Phase retrieval of diffraction patterns from noncrystalline samples using the oversampling method. *Physical Review B*, 67:174104, 2003.

[101] C. T. Chantler, K. Olsen, R. A. Dragoset, J. Chang, A.R. Kishore, S.A. Kotochigova, and D. S. Zucker. X-ray form factor, attenuation and scattering tables(version 2.1). [online] available: http://physics.nist.gov/ffast [2009, may 13]. national institute of standards and technology, gaithersburg, md. originally published

as chantler, c.t., j. phys. chem. ref. data 29(4), 597-1048 (2000); and chantler, c.t., j. phys. chem. ref. data 24, 71-643 (1995). 2005.

[102] D. L. Windt, W. C. Cash, M. SCott, P. Arendt, B. Newman, R. F. Fisher, A. B. Swartzlander, P. Z. Takacs, and J. M. Pinneo. Optical constants for thin films of c, diamond, al, si, and cvd sic from 24 a to 1216 a. *Applied Optics*, 27(2):279–295, 1988.

[103] C. F. Chau and T. Melvin. The fabrication of macroporous polysilicon by nanosphere lithography. *J. Micromech. Microeng.*, 18:064012, 2008.

[104] A. L. Patterson. The scherrer formula for x-ray particle size determination. *Physical Review*, 56:978–982, 1939.

[105] Coherent inc., September 2009. `http://www.coherent.com/`.

[106] M. Nisoli, S. Stagira, S. De Silvestri, O. Svelto, S. Sartania, Z. Cheng, M. Lenzner, C. Spielmann, and F. Krausz. A novel-high energy pulse compression system: generation of multigigawatt sub-5-fs pulses. *Applied Physics B Lasers and Optics*, 65(2):189–196, 1997.

[107] A. Suda, M. Hatayama, K. Nagasaka, and K. Midorikawa. Generation of sub-10-fs, 5-mj-optical pulses using a hollow fiber with a pressure gradient. *Applied Physics Letters*, 86:111116, 2005.

[108] J. B. Fenn, M. Mann, C. K. Meng, S. F Wong, and C. M. Whitehouse. Electrospray ionsation for mass spectrometry of large biomolecules. *Science*, 246(4926):64–71, 1989.

[109] M. J. Bogan, W. H. Benner, S. Boutet, U. Rohner, M. Frank, A. Barty, M. M. Seibert, F. Maia, S. Marchesini, S. Bajt, B. Woods, V. Riot, S. P. Hau-Riege, M. Svenda, E. Marklund, E. Spiller, J. Hajdu, and

H. N. Chapman. Single particle x-ray diffractive imaging. *Nano Letters*, 8(1):310–316, 2007.

[110] C. F. Bohren and D. R. Huffman. *Absorption and Scattering of Light by Small Particles.* Wiley, Weinheim, 2004.